The Dissertation Committee for Arjang Shahriari Certifies that this is the approved version of the following dissertation:

Electrostatic Control and Enhancement
of
Film Boiling Heat Transfer

Committee:

Vaibhav Bahadur, Supervisor

David Bogard

Ofodike Ezekoye

Roger Bonnecaze

Jayathi Murthy

Electrostatic Control and Enhancement
of
Film Boiling Heat Transfer

by

Arjang Shahriari

Dissertation

Presented to the Faculty of the Graduate School of
The University of Texas at Austin
in Partial Fulfillment
of the Requirements
for the Degree of

Doctor of Philosophy

The University of Texas at Austin
May 2018

Dedication

To my mother, Parisima,
for her unconditional love …
To my father, Fariborz,
for being my role model …
To my sister, Anoosheh,
for being my best friend …
To my soulmate, Katayoun,
for being my inspiration …

Acknowledgements

Completion of this thesis would not have been possible without the support and contribution of many people. It is a great honor for me to thank some of those many, to whom I owe my deepest gratitude.

I would like to sincerely thank my advisor, Prof. Vaibhav Bahadur, for guiding me throughout last few years. This entire process has been such an enjoyable and rewarding experience. Your scientific intuition, invaluable insights, and continuous involvement were indispensable in developing my academic merits. Thank you for all the time and attention you have given to myself and my work.

I would like to thank my dissertation committee, Prof. David Bogard, Prof. Ofodike Ezekoye, Prof. Roger Bonnecaze, and Prof. Jayathi Murthy, for their time in reviewing my work and for their valuable input. I would also like to thank Prof. Carlos Hidrovo for his support and advice when I when I first started my Ph.D. program. I am grateful for everything I learned during our time working together.

I would like to thank all of my past and current lab mates. I have learned so much from everyone and have thoroughly enjoyed my time in our labs. I would like to particularly thank Dr. Brian Carroll, Dr. Tae Jin Kim, Dr. Katherine Carpenter, Dr. Renee Hale, Enakshi Wikramanayake, Onur Ozkan, Palash Acharya, Manoj Lokanathan, Mark Hermes and Siavash Zamani.

I would like to acknowledge the staff of the Department of Mechanical Engineering at The University of Texas at Austin, Mark Phillips, Sarah Parker, Terrie Chandler, Diana Ziegler and Jenny Kondo for their technical and administrative support.

Last but definitely not least, an enormous thank you to my family. This work would not have been possible without their continuous support and unconditional love. I wish to express my sincere appreciation to my beloved parents, Parisima and Fariborz, thank you for your incredible support and unconditional love through my entire life. Thank you Anoosheh, for being the most amazing sister anyone could ever have. Thank you Katayoun for enriching my life with much love and support.

Electrostatic Control and Enhancement of Film Boiling Heat Transfer

Arjang Shahriari, Ph.D.
The University of Texas at Austin, 2018

Supervisor: Vaibhav Bahadur

Boiling heat transfer is severely degraded at high surface temperatures due to the formation of a vapor layer at the surface, commonly known as the Leidenfrost effect. Heat transfer is limited to a critical heat flux (CHF); higher heat fluxes lead to surface dryout and temperature excursions. An externally applied electric field in the vapor layer can significantly enhance boiling heat transfer for electrically conducting or polar liquids. In such liquids, the electric field is concentrated in the vapor layer, and promotes liquid-surface contact, which can significantly enhance boiling heat transfer.

This dissertation is a fundamental study of the influence of concentrated interfacial electric fields on film boiling heat transfer for liquids with finite electrical conductivity (like water and organic solvents). This dissertation describes experimental, analytical and numerical studies on various aspects of the physics underlying electrostatic suppression of film boiling. This dissertation also quantifies the heat transfer benefits associated with electrostatic suppression of film boiling. This dissertation is divided into five main studies, which analyze different aspects of electrostatic suppression of the Leidenfrost state.

The first part of this dissertation (Chapter 2) describes droplet-based experimental investigations on electrostatic suppression of the Leidenfrost state. It is demonstrated that the Leidenfrost state can be suppressed and surface dryout can be prevented using externally applied electric fields (AC or DC). Elimination of the Leidenfrost state increases

heat dissipation capacity by more than one order of magnitude. In preliminary experiments, heat removal capacities exceeding 500 W/cm^2 are measured for water, which is five times the CHF of water on common engineering surfaces. A multiphysics analytical model is developed to predict the vapor layer thickness in the Leidenfrost state.

The second part of this dissertation (Chapter 3) analyzes the fundamental mechanisms underlying electrostatic suppression of Leidenfrost state. It is shown that the interplay of destabilizing and stabilizing forces determines the minimum (threshold) voltage required to suppress the Leidenfrost state. Detailed linear instability analysis is conducted to investigate the growth of electrostatically-induced perturbations on the liquid-vapor interface in the Leidenfrost state, and predict the threshold voltage required for suppression.

The third part of this dissertation (Chapter 4) focuses on suppression of the Leidenfrost state on soft, deformable surfaces, like liquids. It is seen that the nature of electrostatic suppression on a deformable liquid substrate is drastically different from that on a solid substrate. This is due to the existence of an electric field inside the substrate and the deformability of the substrate. A multiphysics analytical model is developed to predict the vapor layer thickness on deformable liquids.

The fourth part of this dissertation (Chapter 5) includes experimental studies on suppression of film boiling during high temperature quenching of metals. It is shown that an electric field can fundamentally change the boiling patterns, wherein the stable vapor layer (film boiling) is replaced by intermittent wetting of the surface. This fundamental switch in the heat transfer mode significantly accelerates cooling during quenching. An order of magnitude increase in the cooling rate is observed, with the heat transfer seen approaching saturation at higher voltages. An analytical model is developed to extract voltage dependent heat transfer rates from the measured cooling curve.

The fifth part of this dissertation (Chapter 6) develops the concept of using acoustic signature tracking to study electrostatic suppression of film boiling. It is shown that acoustic signature tracking can be the basis for objective measurements of the threshold voltage and frequency required for suppression. Acoustic signature tracking can also detect various boiling patterns associated with electrostatically-assisted quenching. With appropriate calibration, this technique can be used to estimate surface temperatures, heat flux and onset of dryout associated with electrically enhanced boiling.

In summary, this dissertation has led to seminal contributions in the field of boiling heat transfer, and essentially opened up a new area of study in the field. This work has shown that electric fields can make the CHF limit irrelevant, and reshape the boiling curve. The present work lays the foundations for electrically tunable boiling heat transfer with conducting liquids. The impact of the proposed work is evident in the area of quenching, where electrically tunable cooling offers a new tool to control the microstructure and mechanical properties of metals.

Table of Contents

List of Tables

List of Figures

Chapter 1: Introduction and literature review [1]

Boiling heat transfer is a very efficient way of removing heat as it relies on the large latent heat of vaporization of the working fluid. Boiling can provide very high heat dissipation capacity at low surface superheats. In practice, boiling heat transfer rates at elevated surface temperatures are limited by the formation of a vapor layer on the surface. The underlying phenomena are depicted in the classical boiling curve (Figure 1.1) which shows the heat flux versus wall superheat (T_{wall} -T_{sat}) for pool boiling (bulk fluid is stagnant), where T_{wall} is the surface temperature and T_{sat} is the saturation temperature at the ambient pressure. The nucleate boiling region (A-B) is characterized by bubble nucleation, growth and subsequent detachment resulting in high heat fluxes. However, the heat transfer rates do not increase indiscriminately. At point B, bubble generation becomes dominant and an insulating vapor layer starts forming which degrades heat transfer. The region (B-C) is the transition region wherein the surface is alternately covered by liquid or vapor. Point C is the Leidenfrost point, wherein the surface is completely covered by an insulating vapor layer and the heat transfer capacity is severely reduced. At this point, heat transfer occurs through conduction and radiation across the vapor gap. The region to the right of point C is the film boiling region and is marked by increasing heat fluxes with increasing wall superheats; this increase in heat flux is primarily due to an increase in radiative heat transfer. The practical significance of the Leidenfrost state is the fact that the vapor gap is a barrier to heat transfer and limits the operating conditions to the left of point B, which is denoted as the critical heat flux (CHF). The high temperatures at point D also pose a

---

[1] The contents of this chapter have been partially published in the following journal article: **Shahriari A**, Birbarah P, Oh J, Miljkovic N, Bahadur V. (2017) Electric-field-based control and enhancement of boiling and condensation. Nanoscale and Microscale Thermophysical Engineering, 21 (2), 102-121.

significant operational risk, as they are higher than the melting point of many common metals.

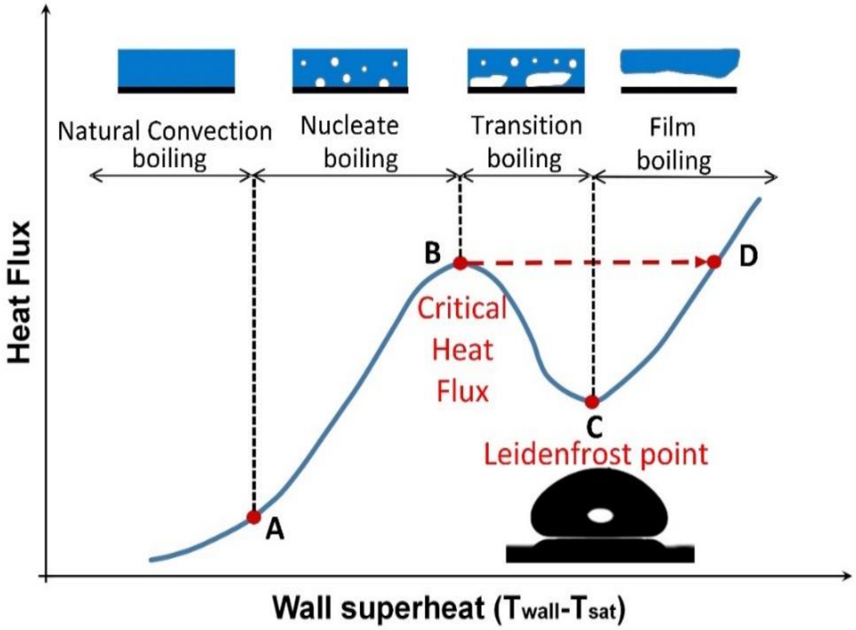

Figure 1.1. Classical boiling curve, identifying various regimes in pool boiling. The inset shows a water droplet (diameter ~ 2 mm) in the Leidenfrost state.

Boiling heat transfer (BHT) has been widely studied over many decades (Bigham et al., 2011; Roh, 2014; Mahmoudi et al., 2013; Kivisalu et al., 2014; Lee et al., 2005; Bergman et al., 2011; Raj et al., 2010; Carey, 2007; Lie et al., 2005; Vassallo et al., 2004; Dhir, 1998; Rahman et al., 2015; Rahman et al., 2014; Geisler et al, 2009; Son et al., 2008; Arik et al., 2003; Basu et al., 2002) and there is a rich repertoire of review articles (Arik et al., 2011; Fan et al., 2016; Konishi et al., 2015; Kim et al., 2015; Dhir et al., 2013; Murshed et al., 2011; Kim, 2009; Pioro et al., 2004) on this topic. Despite extensive research, there are significant unanswered questions related to meso, micro and nanoscale phenomena influencing various regimes of the boiling curve. A significant number of recent studies have analyzed the role of surface engineering (surface texture and chemistry) on the critical heat flux (CHF) and heat transfer coefficients in nucleate boiling (O'Hanley et al., 2013; Adera et al., 2013; Kwon et al., 2013; Chu et al., 2013; Zou et al., 2013; Chu et al, 2012; Cooke et al., 2012; Kim et al., 2010; Chen et al., 2009; Li et al., 2007; Dhillon et al., 2015). It has been shown that active force fields such as acoustics (Ng et al., 2015) and magnetic fields (Naphon et al, 2015) etc. can also influence boiling.

This dissertation studies the role of an electric field in controlling and enhancing film boiling heat transfer. This concept relies on using an active force field to control microscale fluid mechanics and heat transfer in the film boiling region, and is thus different from most recent studies, which use passive surface engineering techniques to enhance boiling heat transfer. The work in this dissertation is based on, and inspired from a well-understood microfluidic technology known as electrowetting (EW).

Over the past two decades, EW has emerged as a powerful tool for controlling droplet-based microfluidic operations like droplet motion, creation and merging (Mugele et al., 2005; Lippmann, 1875; Chen et al., 2013; Bahadur et al., 2006; Kumari et al., 2008; Bahadur et al., 2007; Bahadur et al., 2008a, Bahadur et al., 2008b). EW works for electrically conducting liquids (even very low conductivity liquids like deionized water, organic solvents, etc.). EW is based on the electrical modulation of solid-liquid interfacial tension to control wettability. An illustration of the role of an electric field in influencing wettability is depicted in Figure 1.2. Figures 1.2a and 1.2b show an electrically conducting water droplet resting on a dielectric layer. A potential difference is established across this dielectric layer using the conducting droplet as the top electrode and a second underlying electrode below the dielectric layer. An electric field (AC or DC) applied across the dielectric causes the droplet to wet the surface (Figure 1.2b). This action is called electrowetting and is reversible. It is noted that there is no electric field in the electrically conducting droplet and the entire potential difference falls across the dielectric layer (typically ~ 1 μm thick). Also, there is no steady state current flowing through the circuit as the dielectric layer blocks DC current. It should also be noted that liquids with very low electrical conductivity are compatible with electrowetting; even deionized water can be electrowetted as it picks up ions from air.

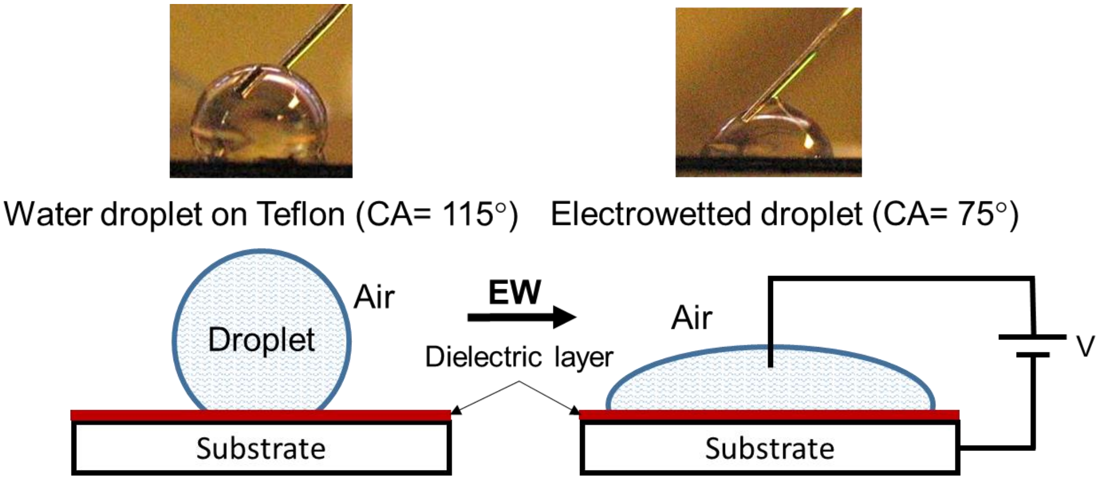

Figure 1.2. Electrowetting-induced change in the droplet shape (and contact angle). An applied electric field across the dielectric layer causes the droplet to spread, this happens because the droplet is electrostatically attracted to the substrate.

It is noted that EW requires a dielectric layer to enable electrical attraction. This attraction can be understood by considering the analogy of a parallel plate capacitor with a dielectric in between two conducting plates. It is well known that the plates attract when the capacitor is charged. In an EW configuration, the conducting liquid is one of the plates and is attracted towards the substrate. It is noted that the droplet stays equipotential, and the entire voltage difference falls across the surface capacitance.

The above concept of electrostatic attraction can also be used to fundamentally eliminate the Leidenfrost state by attracting liquid towards the surface. This is the primary hypothesis of the work contained in this dissertation. The electric field will exist in the vapor layer and the dielectric layer (since the droplet is equipotential). The dielectric layer is not essential to electrostatic suppression, indeed many experiments were conducted without it. However, the dielectric layer reduces steady state DC current flow (and Joule heating), which significantly reduces the power consumption. It is also noted that the added thermal resistance of the dielectric layer is insignificant compared to that of the vapor layer which is eliminated.

In section 1.1 previous studies on the role of electric fields on enhancement and control of boiling heat transfer using insulating and conducting liquids are discussed. Sections 1.2 and 1.3 discuss the motivations and objectives of this dissertation, respectively. Section 1.4 reviews previous studies relevant to the present dissertation. Section 1.5 describes the organization of the rest of this dissertation.

1.1. INFLUENCE OF ELECTRIC FIELDS ON BOILING HEAT TRANSFER

Influence of electric fields on boiling heat transfer with electrically insulating liquids

Electric fields have been widely explored for influencing thermal-fluid systems. Electrohydrodynamics (EHD) (Pearson et al., 2011) and dielectrophoresis (Pohl, 1978; Jones, 2001) are widely studied phenomena that rely on electric fields to actuate fluids. There have been many past studies on the use of electric fields for boiling heat transfer enhancement (Siedel et al., 2011; Chen et al., 2012; Lie et al, 2006; Zhang et al., 2010; Takata et al., 2003; Schweizer et al., 2013; Di Marco et al., 2003; Quan et al., 2015;

Sheikhbahai et al., 2012; Bologa et al., 2012; Wang et al, 2009; Zaghdoudi et al., 2005; Di Marco et al., 2011; Di Marco et al., 2011; Kweon et al., 2000; Zaghdoudi et al., 1999; Carrica et al., 1997; Mahmoudi et al., 2014; Migliaccio et al., 2013; Takano et al., 1996; McGranaghan et al., 2014; Verplaetsen et al., 1999; Pandey et al., 2016; Cipriani et al., 2004). However, most studies are confined to electrically insulating (dielectric) liquids such as refrigerants (electrical conductivity is O (10^{-14}) S/m). For such liquids, the electric field exists in the bulk of the liquid, and the field magnitude in the region near the interface is similar to that in the bulk.

A detailed review of boiling heat transfer enhancement in insulating liquids using electric fields is not the primary objective of this dissertation. Indeed, there is a detailed review of this topic (Grassi et al., 2006). This section summarizes the findings of recent and significant studies on this topic. Studies have analyzed the influence of electric fields on:

a. Bubble dynamics (generation, growth, departure)

The influence of electric fields on various aspects of bubble dynamics such as growth, detachment, departure velocity, and trajectory has been investigated in recent studies (Siedel et al., 2011; Chen et al., 2012; Lie et al, 2006; Zhang et al., 2010; Takata et al., 2003; Schweizer et al., 2013; Di Marco et al., 2003). In general, studies show that electric fields can increase the bubble release frequency and prevent coalescence of adjacent bubbles (Chen et al., 2012; Lie et al, 2006; Zhang et al., 2010; Takata et al., 2003). Similar studies (Schweizer et al., 2013; Di Marco et al., 2003) under microgravity show that electric fields act to elongate bubbles and promote their detachment. It is noted that bubble sizes under microgravity are smaller than those in terrestrial conditions; however, the application of electric fields enlarges the bubbles to sizes comparable to those in regular gravity conditions.

b. Enhancement of nucleate boiling heat transfer

Nucleate boiling heat transfer enhancement by electric fields has been the focus of a significant number of studies (Quan et al., 2015; Sheikhbahai et al., 2012; Bologa et al., 2012; Wang et al, 2009; Zaghdoudi et al., 2005; Di Marco et al., 2011; Di Marco et al., 2011; Kweon et al., 2000; Zaghdoudi et al., 1999; Carrica et al., 1997; Mahmoudi et al., 2014; Migliaccio et al., 2013; Takano et al., 1996; McGranaghan et al., 2014). Various aspects of nucleate boiling have been studied, including the combined influence of electric fields and nanoparticles on boiling (Sheikhbahai et al., 2012), relations between convective flow and heat transfer (Bologa et al., 2012), realization of nucleate boiling at lower superheats (Wang et al, 2009), and elimination of hysteresis (Zaghdoudi et al., 2005). Microgravity studies show that electric fields can replace buoyancy to maintain boiling characteristics by promoting bubble departure and inhibiting bubble coalescence (Di Marco et al., 2011; Di Marco et al., 2011). Enhancements (Figure 1.3) of the critical heat flux (CHF) and heat transfer coefficient have been measured using pool boiling experiments (Kweon et al., 2000; Zaghdoudi et al., 1999; Carrica et al., 1997). These increases are attributed primarily to modified bubble behavior (rapid generation and increased detachment frequency) under electric fields. It should also be noted that the heat transfer enhancement is more pronounced at lower superheats (Kweon et al., 2000). In addition to pool boiling experiments, studies have investigated electric field-based boiling heat transfer enhancement under jet impingement (showing flattening of the boiling curve in the post CHF-regime (Mahmoudi et al., 2014)). Boiling heat transfer enhancement has also been demonstrated using droplets (showing electrowetting-induced effects (Migliaccio et al., 2013; Takano et al., 1996)), and in a microchannel flow boiling configuration (McGranaghan et al., 2014).

c. Enhancement of film boiling heat transfer

Heat transfer is substantially degraded in the film boiling regime because of the vapor layer which acts as a thermal insulator (Bergman et al., 2011). Studies have shown (Verplaetsen et al., 1999; Pandey et al., 2016; Cipriani et al., 2004) that an EHD-induced instability of the vapor-liquid interface can enhance heat transfer. A recent study (Pandey et al., 2016) reported a threshold voltage above which electric fields are effective. Greater enhancement was observed at higher electric fields and lower superheats (Cipriani et al., 2004).

The extent to which electric fields can influence boiling heat transfer is summarized in Figure 1.3. Figures 1.3a and 1.3b show experimental measurements of the maximum enhancements of CHF and the heat transfer coefficient, respectively, as a function of the electric field. Various insulating fluids were used in these studies including electronics cooling fluids (FC and HFE fluids from 3M), refrigerants (R113 and R123) and other liquids (*e.g.* liquid nitrogen). Figure 1.3 indicates that the CHF and heat transfer coefficient can be enhanced by up to 4X and 7X, respectively. It is important to note that Figure 1.3 includes data obtained from various experimental configurations, multiple working fluids, and with different experimental procedures. Direct comparisons of various data points will therefore have very limited utility. However, Figure 1.3 clearly suggests that electric fields can enhance heat transfer, and that any heat transfer enhancements will be less than one order of magnitude.

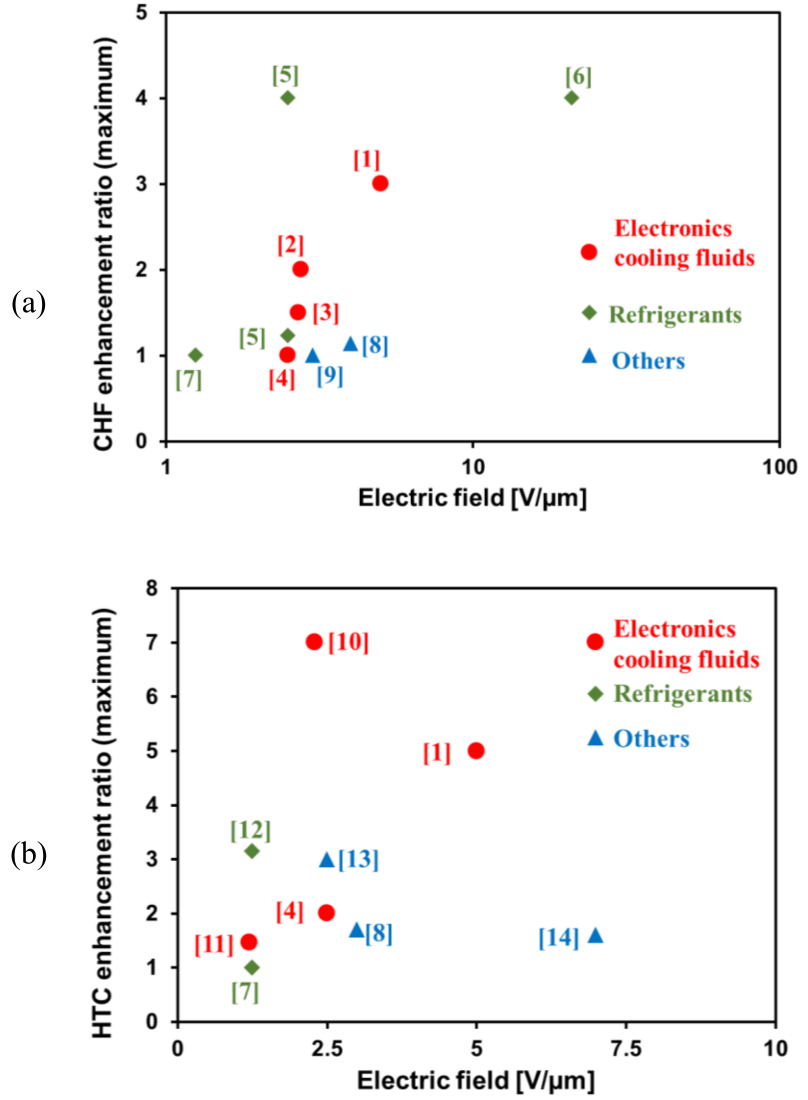

[1] Cipriani et al., 2004

[2] Mahmoudi et al., 2014

[3] Verplaetsen et al., 1999

[4] Di Marco et al., 2011a

[5] Zaghdoudi et al, 2005

[6] Carrica et al., 1997

[7] Quan et al., 2015

[8] Sheikhbahai et al., 2012

[9] Wang et al., 2009

[10] McGranaghan et al., 2014

[11] Di Marco et al., 2011b

[12] Kweon et al., 2000

[13] Zaghdoudi et al., 1999

[14] Bologa et al., 2012

Figure 1.3. Enhancement of (a) critical heat flux, and (b) heat transfer coefficient versus the applied electric field for insulating liquids. Experimental data was obtained from the citations in brackets. The baseline for the enhancement was the heat transfer in the absence of an electric field for that particular study. Figure 1.3 reprinted with permission from Shahriari et al. Copyright 2017 Taylor & Francis.

Influence of electric fields on boiling heat transfer with electrically conducting liquids

This section focusses on recent work on boiling heat transfer enhancement of electrically conducting liquids. These include liquids such as water and organic solvents (methanol, isopropanol, ethanol) with conductivities ranging from 10^{-6} S/m-10^{-4} S/m. In contrast to insulating liquids, such liquids will be equipotential (no electric field inside the liquid). Consequently, the applied voltage falls entirely across the relatively insulating vapor layer or bubbles near the surface. This concentrated interfacial electric field can influence boiling-related phenomena more strongly than the volumetric electric field in insulating liquids. Therefore, electric fields can be a powerful tool for boiling heat transfer enhancement for liquids with finite electrical conductivities. Despite the above benefits, boiling heat transfer enhancement of conducting liquids via electrical means has not received a lot of research attention.

The most relevant study in this area was conducted in 1964 by Markels and Durfee (Markels and Durfee, 1964), who investigated the influence of an electric field on boiling of isopropanol and water on a cylindrical surface. A horizontal 3/8" chrome plated copper tube was heated internally by saturated steam generated by boiling oleic acid. DC and AC voltages were used for isopropanol and water-based studies, respectively. The applied voltage magnitude varied from zero to 10 kV. The AC frequency was varied between 50 to 5000 Hz. A slight decrease in the heat flux was reported at the lowest and highest frequencies, however the underlying reasons were not discussed. The entire boiling regime (nucleate, transition and film) was experimentally investigated.

Markels and Durfee also studied the influence of an electric field on flow boiling (Markels and Durfee, 1965a). Isopropanol or water flow (of up to 5 gallons/min) through a vertical annulus (3/8" inner diameter and 0.96" outer diameter) was studied. The annulus was either heated from the inner pipe or from the outer pipe by steam generated by boiling oleic acid. AC voltages (60 Hz frequency) and up to 3kV magnitude were used. They calculated the surface wetting ratio by assuming that the electrical resistance between the surface and the electrode is inversely proportional to the wetted area (Markels and Durfee, 1965a). The wetted fraction converged to 50% of the total surface area as the voltage increased. Therefore, the influence of surface wetting was important when the voltage was below 3 kV. When maximum wetting was reached (~50%), the heat flux increased linearly, mainly due to better mixing and more favorable bubble shape factors (Markels and Durfee, 1965b).

Takano (Takano et al., 1996) reported that an electric field across the vapor gap can eliminate the Leidenfrost state to enhance heat transfer. This work demonstrated Leidenfrost state suppression for R113 (insulating) and ethanol (conducting) droplets, and reported heat transfer enhancements of upto 2.8X and 7.6X, respectively.

A recent study discussed electrical suppression of the Leidenfrost state (Celestini et al., 2012). It was reported that an electric field applied across the vapor gap could completely eliminate the Leidenfrost state for water droplets.

In a more recent study (Cho et al., 2015), tunable nucleate boiling using electric fields and charged surfactants was demonstrated, with water as the working fluid. This study used low applied electrical potentials (< 2 V), to control bubble nucleation by electrostatically absorbing and desorbing charged surfactants (SDS and DTAB) to change the surface wettability. The ability to turn bubbles 'on' and 'off' spatially and temporally by applying suitable electric potentials was demonstrated. Pool boiling measurements indicated heat transfer enhancement approaching one order of magnitude. These findings are especially significant in view of the very low voltages utilized. Optimization of the electrical waveform and an optimized spatial configuration for nucleating bubbles can likely enhance heat transfer performance further. This study also highlights the benefits of combining multiple approaches (surfactants and electric fields) to improve boiling heat transfer.

1.2. MOTIVATION OF PRESENT WORK AND APPLICATIONS

The present work is intended to highlight the advantages of electric fields in the control and enhancement of boiling heat transfer, as compared to passive surface engineering approaches. One of the most important benefits of the use of electric fields is that the CHF limit can be made irrelevant, by forcing fluid to wet the surface.

The CHF limit of surfaces has been widely studied, with the objective of enhancing the CHF (Dhir, 1998; Roh, 2014; Lie et al., 2005; Mahmoudi et al., 2013; Raj et al., 2010; Liu et al, 2007; Lee et al., 2011; Bar-Cohen et al., 2000; Arik et al., 2011). Surface engineering (O'Hanely et al., 2013; Adera et al., 2013; Kown et al., 2013; Vakarelski et al., 2012; Zou et al., 2013; Chu et al., 2012; Chen et al., 2009; Li et al., 2007), is the most commonly explored CHF enhancement tool. Surface wettability (which depends on surface chemistry and texture) and texture (geometry, porosity, re-entrant cavities) can significantly influence the CHF. In general, it has been shown that hydrophilic surfaces increase CHF since they promote rapid rewetting after bubble departure. Similarly, texture-induced wicking promotes rewetting and enhances CHF. Similar results have also been observed using nanofluids, wherein nanoparticle deposition increases the wettability and CHF. Hydrophobic surfaces, on the other hand, promote bubble nucleation and growth (to minimize water contact), which increases the heat transfer coefficient but lowers CHF. It is noted that roughness-causing textures also act as bubble nucleation sites, and thus affect heat transfer coefficients. There have also been related studies of the Leidenfrost effect to identify parameters which determine the Leidenfrost (dryout) temperature.

To summarize, surface engineering offers avenues for CHF enhancement that have been explored significantly. However, all current CHF enhancement techniques are based on coatings or engineered surfaces. Such technologies have many limitations resulting from the low durability, performance degradation and fouling associated with surface textures. Additionally, scalable coating deposition techniques do not yet exist for many materials. Special challenges include coating deposition on non-flat surfaces and deposition in non-line of sight areas. The use of electric fields offers options to overcome some of these challenges and additionally provide the option of real-time, dynamic control of boiling heat transfer. It is noted that electrification of boiling systems does introduce formidable new challenges, but eventual decisions on the heat transfer enhancement method will be based on analysis of the benefits versus the challenges.

Table 1.1 highlights the advantages of electric field over surface engineering-based approaches. Table 1.1 summarizes recently reported CHFs and Leidenfrost temperatures on various surfaces. Existing surface engineering-based approaches cannot prevent the Leidenfrost state even at moderate superheats (< 50 °C) and have modest CHF's. The second row (results from present work) shows related experimental results on electrical suppression of the Leidenfrost state (detailed in chapter 2 of this dissertation). It is clearly seen that the electric field-based approach can elevate the Leidenfrost temperature significantly (reduce dryout risks) and result in very high CHF's.

Research group	**Fluid**	**Surface details**	**Dryout Superheat [°C]**	**CHF [W/cm^2]**
Shahriari et al., 2014	**Water, Organic solvents**	**Interfacial electric field**	**> 450**	**> 400**
Li et al., 2007	DI water	Microporous textures	65	350
Rahman et al., 2014	Water	Hierarchical textures	35	257
Chu et al., 2014	Water	Hierarchical textures	35	250
Cooke et al., 2012	Water	Microchannel	20	245
Dhillon et al., 2015	DI water	Regular textures	-	200
Chen et al., 2009	Water	Nanowires	30	200
Kwark et al., 2012	Nanofluids	Nanoparticle coated	30	200
Zou et al., 2013	DI water	Regular textures	35	180
O'Hanley et al., 2013	DI water	Porous hydrophilic	-	160
Mahmoudi et al., 2014	HFE7100	Volumetric electric field	30	70
Zaghdoudi et al., 2005	R-123	Volumetric electric field	25	60

Table 1.1. Superheat required for dryout, and CHF values from recent literature.

This section also briefly discusses the applications of electrically-enhanced boiling as discussed in this dissertation. These applications significantly impact the performance of various systems involved in power generation and materials processing.

- Boilers, steam generators: Boiling heat transfer enhancement can lower fuel consumption and/or increase steam quality.
- Instability control: Film boiling control concepts can be applied to control two-phase flow instabilities. This has applications in microchannel flows, boiling water reactors, etc.
- Quenching: Boiling heat transfer rates determine the cooling curve and the resulting microstructure and properties.

- Distillation: Enhanced boiling heat transfer enables efficient, compact separation.

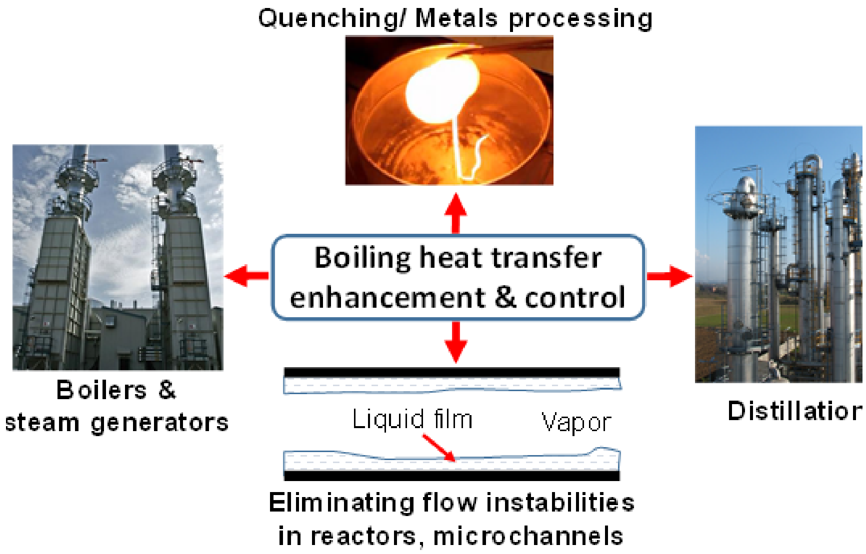

Figure 1.4. Applications which can benefit from electrically-enhanced boiling heat transfer.

1.3. OBJECTIVES OF PRESENT WORK

There are significant fundamental gaps in our understanding of electrostatic suppression and film boiling that must be addressed to enable new technologies in this area. This dissertation answers the following fundamental questions:

1. Can interfacial electric fields suppress film boiling?
2. To what extent can dryout and film boiling be prevented by electrically-induced wetting?
3. What are the mechanisms underlying electrostatic suppression using DC and AC electric fields?

4. What is the minimum voltage/electric field to trigger successful electrostatic suppression?
5. How does electrostatic suppression work in a two-liquid system, where the Leidenfrost droplets rests on another liquid?
6. How can acoustics enable a better understanding of boiling heat transfer?
7. What is the enhancement in boiling heat transfer enhancement resulting from suppression of film boiling?
8. What is the CHF enhancement from the use of electric fields for film boiling suppression?
9. Can electric field-based enhancement reshape the boiling curve by enhancing boiling heat transfer coefficients and making the CHF limit irrelevant?

1.4. LITERATURE REVIEW

In this section, previous studies which are relevant to the objectives of this dissertation, are briefly reviewed.

1.4.1. Previous experimental studies on electrostatic suppression of the Leidenfrost state

Numerous classical studies have investigated pool boiling heat transfer (Dhir, 1998; Kwark et al., 2012; Roh, 2014; Lie et al., 2005; Mahmoudi et al., 2013; Raj et al., 2010; Lie et al., 2005; Arik et al., 2011; Tong et al., 1997; Carey, 2007; Bergman et al., 2011; Bar-Cohen et al., 2000) and assessed the Leidenfrost phenomenon (Bernardin et al. 1999; Biance et al., 2014; Orzechowski et al., 2014; Huang et al. 2007; Burton et al., 2012; Mahadevan et al., 1999; Gottfried, 1966) in detail. It is seen that both surface chemistry and texture influence the Leidenfrost temperature and the stability of the droplet in the

Leidenfrost state. While surface modification-based approaches to control the Leidenfrost state and increase critical heat flux have received significant attention (O'Hanely, 2013; Adera, 2013; Kwon, 2013; Vakarelski, 2012; Cooke, 2012; Chu, 2013; Kim, 2010; Li, 2007; Chen, 2009; Chu, 2012; Zou, 2013; Lee, 2011), there has been much less research into alternative ways to enhance boiling heat transfer and suppress the Leidenfrost state. There have been efforts to study electric fields to control boiling and enhance heat transfer rates (Li, 2012; Kweon, 2000; Mahmoudi, 2014; Bologa, 2012; Welch, 2007; Verplaesten, 1997; McGranaghan, 2014; Schweizer, 2013; Zaghdoudi, 1999; Zaghdoudi, 2005; Cipriani, 2004; Di Marco, 2011). However, the overwhelming majority of such studies are confined to electrically insulating liquids like oils and refrigerants. For such liquids, the electric field exists in the bulk of the liquid, and the field magnitude in the 'near surface' region is similar to that in the bulk. The resulting weak volumetric field (~ 0.1 V/μm), does not affect boiling-influencing surface phenomena strongly and has only a moderate effect on heat transfer.

It should be noted that the suppression mechanism is not the same as the electrowetting (Lippmann, 1875; Mugele et al., 2005; Chen et al., 2014; Miljkovic et al., 2014; Bahadur et al., 2007) on dielectric principle which relies on electrical modulation of liquid-solid interfacial tension. The concept for suppression described in this dissertation is based on electrostatic liquid attraction towards the surface, which significantly reduces the need for surface treatments or modifications. The present work on "Experimental study of electrostatic suppression of the Leidenfrost state" is discussed in chapter 2 of this dissertation.

1.4.2. Previous analytical studies on mechanisms underlying the Leidenfrost state suppression

Instability analyses have been previously used in the field of boiling heat transfer (Panzarella et al., 2000) to estimate the critical heat flux. Rayleigh-Taylor (Kim et al, 2015) and Kelvin-Helmholtz (Kim et al., 2016) instabilities are typically analyzed in such models.

There are no studies on the instabilities associated with electrostatic suppression of the Leidenfrost state, where electrostatic forces are important in addition to surface tension and evaporation-induced pressure buildup. A reasonable starting point for the analyses of instabilities underlying Leidenfrost state suppression is existing studies on instabilities of thin films during electrohydrodynamic patterning (Schaffer et al., 2000; Gambhire et al., 2011; Yang et al, 2013; Elele et al., 2015; Mondal et al., 2014), which analyze electrostatic and surface tension forces. The present work on "Analysis of Leidenfrost state suppression mechanisms" is discussed in chapter 3 of this dissertation.

1.4.3. Previous studies on the Leidenfrost state suppression on deformable surfaces

From a fundamental standpoint, the Leidenfrost state does not necessarily require a solid substrate, and can also be attained on another hot superheated liquid. There exist limited studies (Snezhko et al., 2008; Merrer et al., 2011; Adda-Bedia et al., 2016; Kim et al., 2006; Ding et al., 2016; Maquet et al., 2016; Janssens et al., 2016) on the Leidenfrost state on heated liquid surfaces. Snezhko et al. (Snezhko et al., 2008) studied pulsating-gliding transitions of levitating liquid nitrogen droplets on different supporting liquids. Merrer et al. (Merrer et al., 2011) measured the deceleration of liquid nitrogen droplets floating on the surface of a liquid bath. Adda-bedia et al. (Adda-Bedia et al., 2016) and Kim (Kim et al., 2006) explored the interaction of a water droplet on a bath of liquid nitrogen (inverse Leidenfrost effect). Ding et al. (Ding et al., 2016) explored dynamic interactions of Leidenfrost isopentane droplets on liquid metal surfaces. In a recent study, Maquet et. al. (Maquet et al., 2016) explored the Leidenfrost state of ethanol droplets on a hot pool of silicone oil. This study showed that the Leidenfrost state can be attained with ultralow superheat (~ 1 °C); this was attributed to the molecularly smooth nature of the substrate. In another recent study, Janssens et al. (Janssens et al., 2016) explored self-propulsion behavior and drag of Leidenfrost acetone droplets on a water bath. Davanlou (Davanlou, 2016) studied the role of liquid properties on the lifetime of levitated droplets. Besides these studies, there exist related studies (Shabani et al., 2013; Couder et al., 2005; Savino et al., 2003) on floating aqueous droplets on the free surface of immiscible liquids; however, they do not involve the Leidenfrost effect.

There exist two studies from the1960's which briefly allude to the influence of electric charge on the stability of a floating mass (boule) of liquid in the Leidenfrost state, on the same host liquid. Hickman (Hickman, 1964; Hickman, 1967) studied the floatation of such boules for multiple liquids and observed that applying a potential difference results in a smaller boule size before it bursts. There are also a few studies which analyze the influence of Marangoni flows on the Leidenfrost state on liquid substrates (Davanlou, 2016; Savino et al., 2003; Davanlou et al., 2015). However, an in-depth analysis of the impact of Marangoni flows on the vapor layer thickness in the Leidenfrost state has not been conducted. The present work on "Leidenfrost state suppression on soft surfaces" is discussed in chapter 4 of this dissertation.

1.4.4. Previous experimental studies on the Leidenfrost state suppression during quenching

Leidenfrost effect influences a significant portion of the cooling curve associated with quenching of metals (Bernardin et al., 1996; Sher, 2012; Babu et al., 2011; Unal et al, 1992). Control of cooling rates (Petrov et al., 2012; Lolla, 2012) during heat treatment is a widely employed tool to influence the metallurgy and the resulting mechanical properties of metals. For instance, the development of high strength steels has been made possible by control of the cooling rate along with the use of alloying elements (Al-Ahmadi, 2008; Ravikumar, 2013). Ultrafast cooling (UFC), in particular, has attracted significant attention with the development of techniques like jet impingement (Wang et al., 2012), air atomized spray cooling (Mohapatra et al., 2013), and the use of custom fluid formulations (Mitra et al., 2012) to enhance the cooling rate.

None of the above approaches overcome the fundamental heat transfer limitation associated with vapor layer formation above the Leidenfrost temperature. The Leidenfrost temperature depends on the fluid and surface characteristics (chemistry, texture), and typically varies between 150-250 °C. This is significantly lower than the temperatures associated with heat treatment processes. Significant research (Bernardin et al., 1999; Biance et al., 2003; Huang et al., 2007; Burton et al., 2012) has targeted an analysis of the Leidenfrost phenomenon, with surface chemistry and texture explored (O'Hanley et al., 2013; Adera et al., 2013; Kwon et al., 2013; Chu et al., 2012; Vakarelski et al., 2012; Kim et al., 2011) as the primary avenues to elevate the Leidenfrost temperature. However, such passive surface modification-based approaches work only up to certain temperatures. The present work on "Experimental study of Leidenfrost state suppression during quenching" is discussed in chapter 5 of this dissertation.

1.4.5. Previous studies on acoustic detection of the Leidenfrost state

One limitation in previous studies on Leidenfrost state, is the reliance on visual and optical measurements to infer the physics underlying suppression. In recent studies

(Shahriari et al., 2014; Shahriari et al., 2017a; Ozkan et al., 2017) high speed imaging was used to detect instabilities at the liquid-vapor interface, which indicate suppression. Celestini et al. (Celestini et al., 2012) used interferometry in their study on electrical suppression. While such techniques do yield important insights, the measurements are subjective, and have significant uncertainty. Furthermore, these techniques cannot be used to study more complex situations, e.g. Leidenfrost state on a deformable liquid surface, where the vapor gap is not visible from the side.

Acoustic emission (AE) is a non-destructive complementary method for characterization of micro-mechanisms of boiling. Previously, acoustic measurements have been used to characterize fundamental mechanisms underlying nucleate and film boiling like bubble generation, collapse and coalescence (Lykof et al., 2005; Kwatny et al., 1975; Carmi et al., 2011; Korolev et al., 2002; Smrke et al., 2012; Alhashan et al., 2016; Ravnik et al., 2012; Ravnik et al., 2010; Mojškerc et al., 2018; Neil et al., 1997; Cudina et al., 2003; Oguz et al., 1990). Bubble-related phenomena have an acoustic signature, which depends on the bubble size, superheat and liquid properties. Application-oriented studies have utilized acoustic signature tracking to understand boiling in a reactor core (Kwatny et al., 1975), quenching of metals (Ravnik et al., 2012; Ravnik et al., 2010; Mojškerc et al., 2018) and pump cavitation (Neil et al., 1997; Cudina et al., 2003). Acoustics has also been utilized to study droplet impact on surfaces (Oguz et al., 1990). Two recent studies (Grounds et al., 2012; Padilla et al., 2014) used acoustics to confirm the existence of the Leidenfrost state. Absence of an acoustic signature indicated the Leidenfrost state; distinct sound signals were recorded upon loss of the Leidenfrost state when the droplet touched the surface. The present work on "Acoustic detection of electrostatic suppression of the Leidenfrost state" is discussed in chapter 6 of this dissertation.

1.5. ORGANIZATION OF REST OF DISSERTATION

This dissertation is divided into five main chapters. Chapter 2 describes experimental studies on electrostatic suppression of the Leidenfrost state using AC and DC electric fields, and measurements of the resulting heat transfer enhancement. Chapter 3 discusses analysis of the mechanism underlying suppression of the Leidenfrost state. This chapter includes instability analysis of perturbations on the liquid-vapor interface in the Leidenfrost state. Chapter 4 describes studies on Leidenfrost state suppression on soft, deformable surfaces. It is seen that electrostatic suppression on a liquid substrate is markedly different, when compared to rigid surfaces. In chapter 5, experimental studies on film boiling suppression during quenching are described. It is shown that an electric field can alter boiling patterns and re-shape the boiling curve. Chapter 6 describes acoustic detection of electrostatic suppression of the Leidenfrost state.

Appendix A and B include detailed derivations of the analytical model to predict the vapor layer thickness on solid and deformable surfaces, respectively. Appendix C includes a derivation of the analytical model to predict radial temperature distribution in a sphere for quenching experiments. Appendix D includes a complementary project (on electronucleation of hydrates) that was completed during the PhD program. Appendix E describes another project (on flow regime mapping of high inertial microflows) under the supervision of Prof. Carlos Hidrovo (former advisor).

Chapter 2: Experimental study of electrostatic suppression of the Leidenfrost state [2]

This chapter describes studies on the influence of an electric field in liquids with moderate electrical conductivity (electrical conductivity of a few liquids are provided in Appendix A). For such liquids the fluid largely remains equipotential (there is a weak electric field inside the liquid). Consequently, the entire potential difference falls across the vapor gap resulting in a concentrated electric field (~ 10 V/µm). The presence of this concentrated electric field can influence boiling-related phenomena significantly, which is the hypothesis underlying the present work. There is one previous study on the role of electric fields on electrically conducting liquids on a hot surface. Celestini et al. (Celestini et al., 2012) used an electric field to forcibly wet a 280 °C metallic surface with water. Leidenfrost state suppression on a bare metal surface for electrically conducting liquids will however lead to electrical shorting that reduces the electrostatic force and also results in unwanted electrolysis and chemical reactions in the droplet.

In this chapter, stable and robust Leidenfrost state suppression at ultrahigh surface temperatures (above 500 °C) is demonstrated. Leidenfrost state suppression with ultralow power consumption is demonstrated for surface superheats greater than 8X the Leidenfrost superheat (Leidenfrost temperature minus Boiling point) for certain liquids. These superheat temperatures are the highest at which dryout prevention has ever been successfully reported. Electrically tunable heat transfer is demonstrated for multiple liquids, and the measured heat fluxes exceed 500 W/cm^2. Electrostatic Leidenfrost state

---

[2] The contents of this chapter have been published in the following journal articles: (1) **Shahriari A**, Wurz J, Bahadur V. (2014) Heat transfer enhancement accompanying Leidenfrost state suppression at ultrahigh temperatures. Langmuir, 30 (40), 12074–12081. (2) Ozkan O, **Shahriari A**, Bahadur V. (2017) Electrostatic suppression of the Leidenfrost state using AC electric fields. Applied Physics Letters, 111, 141608.

suppression is seen effective for a variety of liquids including electrically conducting aqueous solutions, deionized water and low electrical conductivity polar organic solvents. As expected, Leidenfrost state suppression is not observed for insulating liquids at voltages up to 2000 V, since the electric field is not concentrated at the surface. The experimental results provide important physical insights on the role of fluid electrical conductivity on electrostatic suppression of the Leidenfrost state. Overall, this study highlights the potential of electric fields to render the traditional CHF limit to heat transfer irrelevant, and reshape the boiling curve.

2. 1. EXPERIMENTAL METHODS

A schematic of the experimental setup is shown in Figure 2.1. Unpolished aluminum wafers were spin coated (Laurell Technologies) with a dielectric layer (~ 1 µm Teflon AF1600). In addition to providing the surface capacitance, the dielectric layer reduces electrical current leakage upon liquid-solid contact. The use of a dielectric layer is not essential for low electrical conductivity liquids like organic solvents, as explained in the discussion section. Liquid droplets were dispensed on the hot surface (above the Leidenfrost temperature) using a micropipette (Eppendorf). Droplets were dispensed while touching a 100 µm diameter aluminum wire, to restrict the mobility of the Leidenfrost droplet. This wire also provides the electrical voltage to bias the droplet using a direct current (DC) power supply (Kepco). Leidenfrost state suppression was observed with a side view high magnification camera (Basler). The entire experimental setup was mounted on a modified goniometer stage (Biolin Scientific).

Experiments were conducted with liquid volumes ranging from small droplets (volume ~ 5 µL) to larger pools of liquid (volume ~ 1 mL). The working fluids were deionized (DI) water, organic solvents (isopropanol, methanol, and acetone) and aqueous sodium chloride (NaCl) solutions of various concentrations (*i.e.* electrical conductivities). It should be noted that all experiments were repeated multiple times and the reported results are the average of at least 5 individual measurements.

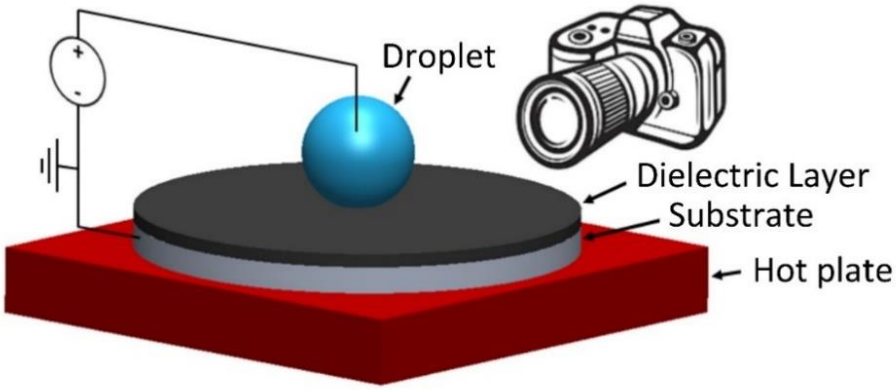

Figure 2.1. Schematic of experimental setup to study electrostatic Leidenfrost state suppression. Figure 2.1 reprinted with permission from Shahriari et al. Copyright 2014 American Chemical Society.

2.2. RESULTS

Table 2.1 shows the measured Leidenfrost temperatures for DI water and isopropanol. It should be noted that the Leidenfrost temperature is not solely an inherent fluid property, but depends on the physical (roughness, nature of texturing) and chemical (surface energy) properties of the underlying surface, as well as the droplet volume. The measured Leidenfrost temperatures were used to estimate the Leidenfrost superheat. This parameter is used to compare results for different fluids.

Fluid	Droplet size [µL]	Surface temperature [°C]	Surface superheat [°C]
Deionized water (DI)	5	230	130
Deionized water (DI)	100	265	165
isopropanol	5	140	57
isopropanol	100	155	72

Table 2.1. Leidenfrost temperatures for water and isopropanol.

Figure 2.2 shows electrostatic Leidenfrost state suppression using concentrated electric fields. Figure 2.2a shows a 100 µL isopropanol droplet on a 360 °C surface in the Leidenfrost state without any applied voltage. As the voltage is increased, 'liquid fingers' from the droplet are attracted towards the surface (Figure 2.2b). These fingers are the result of interfacial instabilities, as the fluid tries to wet the surface. The voltage corresponding to the onset of 'liquid fingering' is called the threshold voltage. As the voltage is further increased (Figure 2.2c), more intimate liquid-solid contact indicates significant Leidenfrost state suppression.

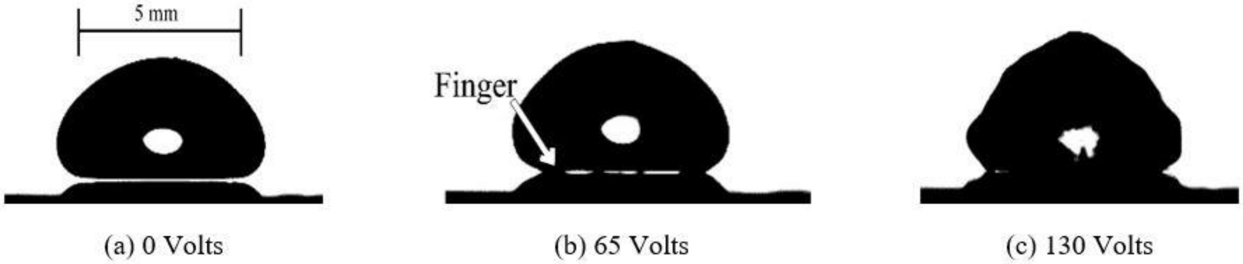

(a) 0 Volts (b) 65 Volts (c) 130 Volts

Figure 2.2. Illustration of Leidenfrost state suppression of a 100 µL isopropanol droplet on a 360 °C surface. a) Leidenfrost state with a visible vapor gap. b) At the threshold voltage, (65 Volts) liquid fingers protrude towards the surface (shown by arrow). c) Enhanced suppression of the Leidenfrost state at a higher voltage (130 Volts). Figure 2.2 reprinted with permission from Shahriari et al. Copyright 2014 American Chemical Society.

Figure 2.3 shows the measured threshold voltages for Leidenfrost state suppression as a function of the surface temperature for water and isopropanol. These results clearly demonstrate that electrostatic Leidenfrost state suppression works even at ultrahigh temperatures (above 500 °C) using moderate applied voltages. The maximum achievable surface temperature (due to practical limitations) in the present experiments was 540 °C. The superheat at this temperature is eight times the Leidenfrost superheat for isopropanol. Even at such extreme temperatures, Leidenfrost suppression was observed for voltages above 80 Volts. Based on these results, it is expected that electrostatic Leidenfrost state suppression will work at even higher temperatures. Furthermore, a very significant observation from Figure 2.3 is the gentle slope of the curves, which indicates that high surface temperatures do not require a steep voltage increase for Leidenfrost state suppression.

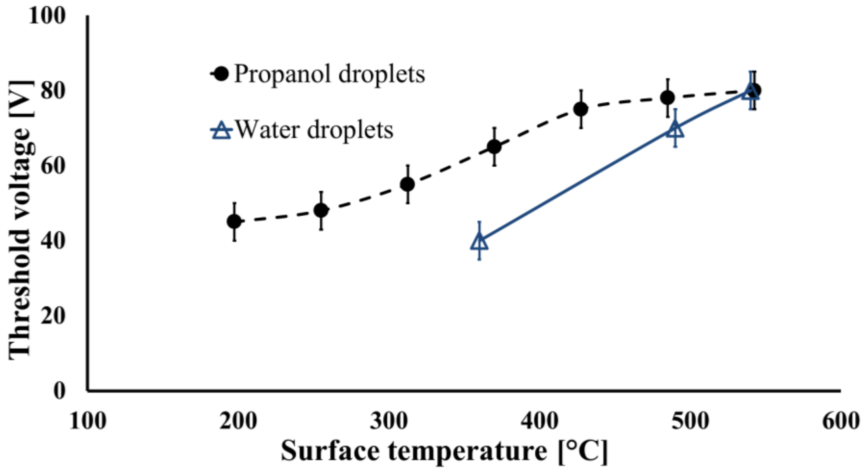

Figure 2.3. Threshold voltage to suppress the Leidenfrost state versus surface temperature for 5µL droplets. Figure 2.3 reprinted with permission from Shahriari et al. Copyright 2014 American Chemical Society.

This study lays the foundation for electrically tunable boiling heat transfer and offers a powerful tool to control boiling heat transfer in the film boiling regime. It should be noted that the heat flux at the Leidenfrost point is typically two orders of magnitude less than the critical heat flux (CHF). This huge reduction is attributed to the high thermal resistance of the vapor layer and depends on the thickness and thermal properties of the vapor layer. More intimate liquid-solid contact resulting from electric fields will reduce the thermal resistance of the vapor layer. The present experimental setup was used to obtain a first-order estimate of the heat transfer benefits accompanying Leidenfrost state suppression.

Heat transfer enhancement can be quantified by measuring the boiling/evaporation rate of the droplet (after the Leidenfrost state is suppressed). Droplet boiling and evaporation depends on the heat pickup rate from the surface. Higher heat transfer rates will lead to faster boiling and shorter droplet lifetimes. These observations are confirmed in Figure 2.4, which shows the droplet (5 μL) lifetime as a function of the applied voltage. The droplet lifetime is the time difference between the onset of the Leidenfrost state suppression and complete droplet evaporation/boiling. Droplet lifetime can be extracted from high speed imaging of droplet boiling. Figure 2.4 shows that the droplet lifetime varies inversely with the applied voltage. This increase in the heat transfer rate is directly attributed to more intimate solid-liquid contact with increasing voltages. An alternative explanation for the reduced lifetime at higher voltages is the increased footprint area of the droplet (*i.e.* droplet spreading). However, high speed visualizations show that the footprint area does not increase significantly with the applied voltage. The reduced droplet lifetime can thus be directly attributed to enhanced fluid-solid contact at higher voltages. At ultrahigh voltages (>1000 Volts), droplet lifetimes can be reduced by a factor of 20 and it is possible to boil off a 5 μL isopropanol droplet in less than 1 second.

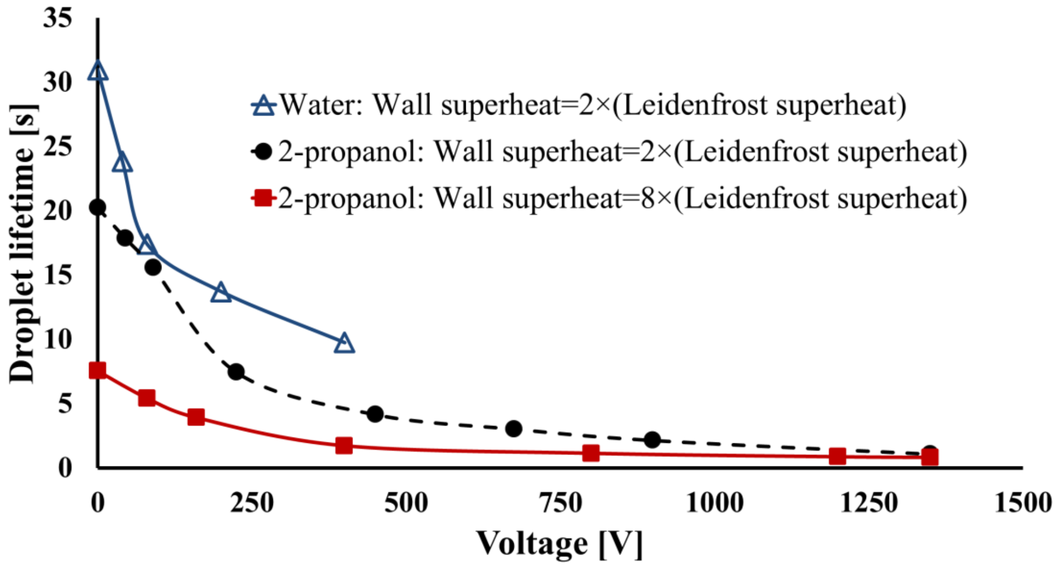

Figure 2.4. Lifetime dependence of isopropanol and water droplets (5 μL) versus voltage. Figure 2.4 reprinted with permission from Shahriari et al. Copyright 2014 American Chemical Society.

The droplet lifetime also depends on the surface superheat, with droplets on a hotter surface having a lower lifetime, as seen in Figure 2.4. It should be noted that the surface temperatures for the same superheat level for deionized water (DI) and isopropanol are not the same, since their Leidenfrost temperatures are different. It should also be noted that experimental results are not reported for DI water above 400 Volts. This is because of satellite droplet emission (Mugele et al., 2005) from the main droplet, which contributes to mass loss. Satellite droplet emission is a well-known phenomenon occurring at high electric fields, and is not discussed in the present work. It should be noted that Leidenfrost suppression works for larger volumes of water (where satellite droplet emission will not occur); however, the present experiments were setup to analyze individual droplets only.

The results of Figure 2.4 can be used to estimate the heat transfer benefits due to elimination of the vapor thermal resistance. A first order energy-balance based estimate of the heat flux picked up by the droplet can be obtained by knowing the droplet mass m, the latent heat of vaporization h_{fg}, the droplet lifetime t_b and the liquid-solid contact area A_s as $q''=(m.h_{fg})/(A_s.t_b)$. Figure 2.5 shows the heat dissipation increase as a function of the applied voltage. This plot shows the utility of the currently approach to enable electrically tunable boiling heat transfer. Heat transfer enhancement factors of more than twenty (compared to the no voltage case) were observed at the maximum voltages applied in this study (1350 Volts). Heat flux dissipation capacities as high as 500 W/cm^2 were obtained, which is five times the critical heat flux (CHF) of water on common engineering surfaces (Bergman et al., 2011). The present results thus constitute a significant advancement in the field of boiling heat transfer. Even higher heat dissipation values are possible through thin film boiling instead of the present droplet-based experiments. It should be noted that the contribution of Joule heating to the overall heat pickup by the droplet is negligible. This was verified by measurements of the leakage currents (10's of µA's) during Leidenfrost state suppression. For example, the worst case contribution of Joule heating on a surface at 2X Leidenfrost superheat temperature with 1350 Volts is ~ 1.4% of the total heat picked up by the droplet. It should also be noted that the added thermal resistance of the low thermal conductivity dielectric layer is insignificant compared to the thermal resistance reduction benefits associated with the vapor gap elimination. Overall, these experiments clearly indicate that electrostatic Leidenfrost state suppression will lead to greater than an order of magnitude heat transfer enhancement.

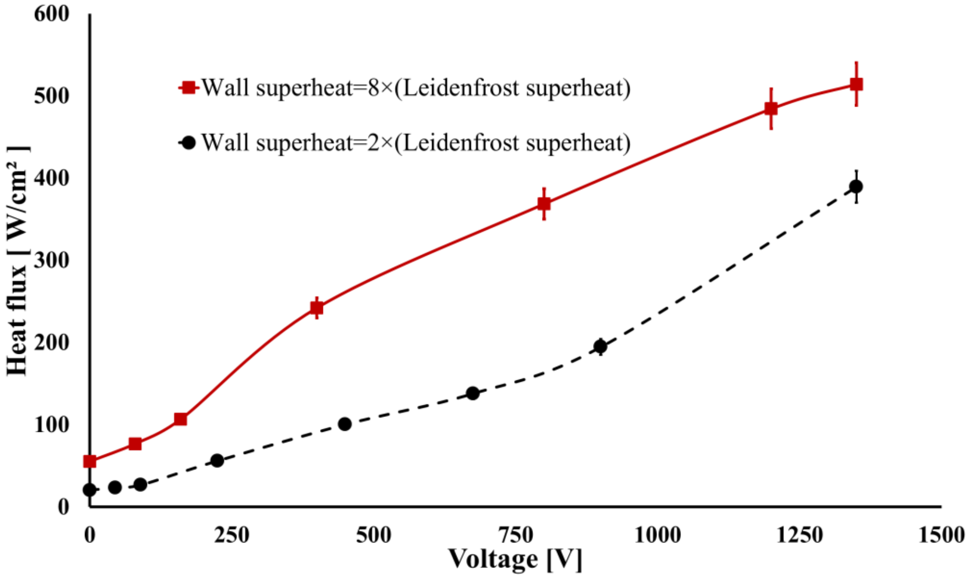

Figure 2.5. Heat flux dissipation associated with boiling 5 μL isopropanol droplets versus the applied voltage. These results illustrate electrically tunable boiling heat transfer. Figure 2.5 reprinted with permission from Shahriari et al. Copyright 2014 American Chemical Society.

An important consideration in the present concept is the role of the dielectric layer in Leidenfrost state suppression. The dielectric layer not only provides a surface capacitance (for electrostatic suppression), but also limits the electrical current leakage and reduces the possibility of electrolysis and other unwanted surface chemical reactions. The dielectric layer and vapor layer essentially constitute two capacitors in series. However, a scaling analysis reveals that for the Leidenfrost vapor layer thickness of O (10) μm and dielectric layer thickness of O (1) μm, the total capacitance is determined primarily by the vapor layer capacitance. Another function of the dielectric layer is limiting current when liquid contacts the surface. This is especially important for aqueous liquids which will short the circuit (in the absence of the dielectric layer), and eliminate the potential difference across the vapor layer. Indeed, this was observed in experiments with aqueous salt solutions. For organic solvents with low electrical conductivities, the dielectric layer is not strictly essential. However, for practical applications, a dielectric layer will be desirable for other reasons including safety and fouling prevention.

The relative location of the dielectric layer on Leidenfrost state suppression was briefly explored in the present work. All the experiments described so far were conducted with a dielectric layer between the conducting substrate and the liquid; this configuration is referred to as ‘dielectric on inside’. It was hypothesized that the location of the dielectric layer could be changed without affecting the Leidenfrost suppression of low electrical conductivity liquids. As an illustration, consider the case of a dielectric layer deposited below the substrate, as shown in Figure 2.6a; this configuration is referred to as ‘dielectric on outside’. The dielectric layer still remains in series with the vapor layer capacitance, and the suppression mechanism is not expected to change. Experiments to verify this hypothesis were conducted with an equivalent Teflon AF1600 layer deposited below the substrate. It is seen that the ‘dielectric on outside’ configuration does not change the results as seen in the droplet lifetime curves in Figure 2.6c. An advantage of this configuration is that the dielectric layer material does not contact the fluid directly, and the possibility of unwanted dielectric-fluid reactions at high temperatures is completely eliminated. This configuration also has important fabrication benefits, since it is much easier to deposit a dielectric layer on the outside of heat transfer equipment (e.g. boiler tubes), instead of on the inside. Figure 2.6c also shows that Leidenfrost suppression works even in the complete absence of a dielectric layer for isopropanol. This is also true for other low electrical conductivity organic solvents as described earlier. However, for high conductivity fluids like aqueous water, the presence of a dielectric layer is essential for stable suppression.

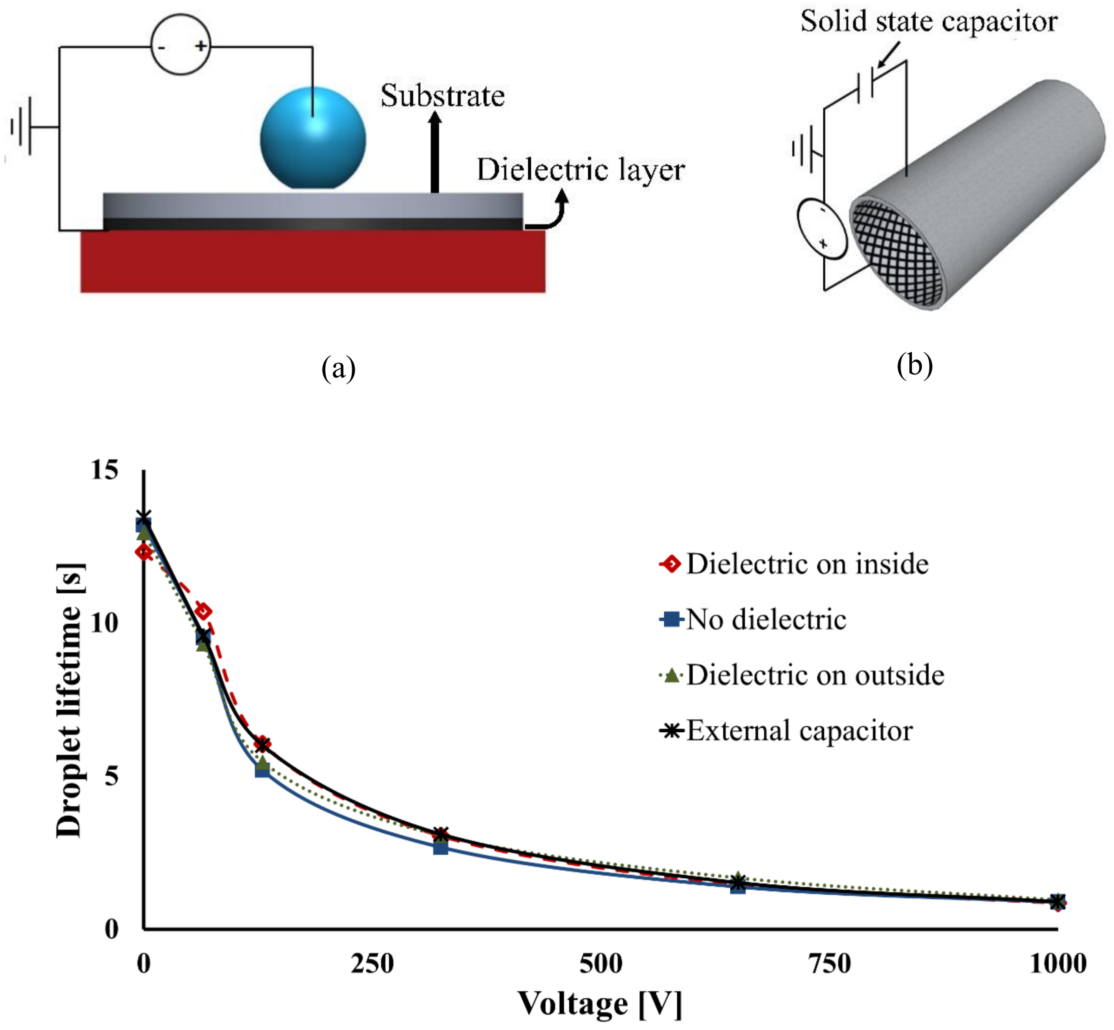

(a)

(b)

(c)

Figure 2.6. Influence of capacitance on Leidenfrost state suppression for 5 µL isopropanol droplets. (a) shows a ‘dielectric on outside’ configuration, where the dielectric layer is below the substrate, (b) shows the dielectric layer replaced by an external solid state capacitor for a boiler tube application. (c) It is seen that the location or nature (dielectric layer versus solid state capacitor) of the capacitance does not affect Leidenfrost state suppression for low electrical conductivity liquids. Figure 2.6 reprinted with permission from Shahriari et al. Copyright 2014 American Chemical Society.

Insights gained from the above experiments were used to conceptualize a new approach to achieve Leidenfrost state suppression. The capacitive action of the dielectric layer can be obtained by replacing it with an equivalent solid state capacitor connected in series with the circuit. This concept is beneficial since it reduces requirements for surface modifications or coating deposition. Furthermore, issues like dielectric layer degradation at high temperatures are eliminated since the solid state capacitor can be located away from the surface. This ‘external capacitor’ concept was experimentally validated by adding a 0.2 μF solid state capacitor in series with the vapor gap. As expected and shown in Figure 2.6c, there was no difference in replacing the dielectric layer, with a solid state capacitor. These results highlight many possibilities for the Leidenfrost state suppression in practical conditions. As an illustration, Figure 2.6b shows a schematic of boiler tubes with an external solid state capacitor included in the circuit. It should be noted that the liquid inside the tube will need to be electrically biased. This can be achieved using periodically spaced electrical feedthroughs in the tube or by a continuous electrode mesh running along the tube (shown in Figure 2.6b).

It is important to note that Leidenfrost state suppression was observed for other organic solvents including methanol, acetone, deionized water and aqueous saltwater solutions. Leidenfrost state suppression was not observed for insulating liquids like FC-40 (electronics cooling liquid made by 3M). This is expected, since the voltage gradient is distributed in the liquid and is not concentrated at the surface. Leidenfrost state suppression for such liquids will require the use of ultrahigh voltages (exceeding 10,000 Volts), and was not attempted in the present work. Overall, electrostatic suppression will work for a wide variety of liquids ranging from high conductivity salt solutions to low conductivity polar organic solvents.

Another important insight from the present work concerns the mechanism of the Leidenfrost state suppression. It is important to distinguish this concept from electrowetting which is an increase in liquid wettability (contact angle reduction) upon the application of an electrical voltage across an underlying dielectric layer. The mechanism underlying Leidenfrost state suppression does not depend upon wettability, and is purely an electrostatic phenomenon. As mentioned earlier, surface wettability will influence the magnitude of suppression, but is a secondary effect. The practical significance of this observation is that Leidenfrost state suppression will work not only for droplets but for larger liquid volumes as well. In conclusion, this concept is a robust tool to eliminate dryout and drive up heat transfer rates in pool and flow boiling applications.

2.3. ANALYTICAL MODELING TO PREDICT LEIDENFROST STATE SUPPRESSION

This section presents a first order model to understand the physics underlying Leidenfrost state suppression. This multiphysics model draws upon analyses from the fields of electrostatics, thermal transport and fluid mechanics to estimate the threshold voltage required for suppressing the Leidenfrost state. The model is based on a force balance on the droplet in the Leidenfrost state, where an upward force due to vapor pressure below the droplet is balanced by the droplet weight.

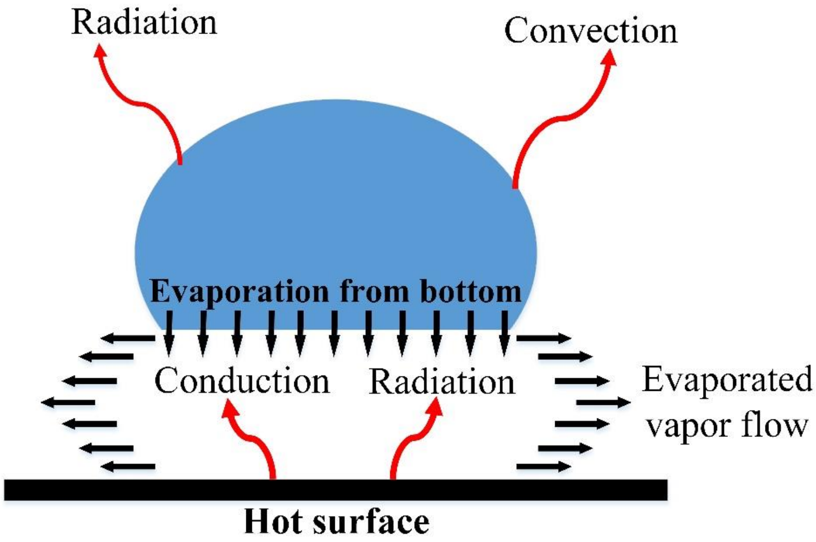

Figure 2.7. Schematic depicting the modeling approach: Poiseuille vapor flow between droplet and substrate. Figure 2.7 reprinted with permission from Shahriari et al. Copyright 2014 American Chemical Society.

The flow in the vapor gap responsible for the upward force on the droplet can be simulated as Poiseuille flow (Figure 2.7). The evaporation rate from the bottom of the droplet determines the magnitude of the pressure buildup. This evaporation rate depends on the heat transfer in the vapor layer and conduction in the droplet. A detailed analytical model was developed to estimate the droplet heat gain (via conduction and radiation through the vapor layer) and droplet heat losses (convection and radiation to the surroundings). The entire model is described in detail in Appendix A. The final outcome is an estimate of the upward force F_{up} on the droplet as:

$$F_{up} = \frac{3\pi}{2}\frac{\mu R^4}{{L_v}^3}\left\{ f_1 \frac{\Delta T_{LF}}{\rho h_{fg}}\left\{ \frac{1}{\left(\frac{L_d}{k_d}+\frac{L_v}{k_v}\right)} + h_{rd} \right\} - f_2 \frac{(h_{rt}+h_c)\overline{\Delta T}}{\rho h_{fg}} \right\} \tag{2.1}$$

In the above equation μ is vapor viscosity, R is droplet base radius, ΔT_{LF} is the surface superheat, ρ is vapor density, h_{fg} is latent heat of vaporization, L_d is dielectric layer thickness, k_d is the thermal conductivity of the dielectric layer, L_v is the vapor layer thickness, k_v is the vapor thermal conductivity, $\overline{\Delta T}$ is the effective temperature difference for estimating heat losses, h_c is the convective heat transfer coefficient, and (h_{rd}, h_{rt}) are radiative heat transfer coefficients on the bottom and top of the droplet, respectively. $f_1=A_{base}/A_{total}$ and $f_2=A_{top}/A_{total}$ are geometrical factors that account for the areas at the bottom and top of the droplet.

The vapor layer thickness is estimated by balancing the upward force and the weight of the droplet. The thickness of the vapor layer depends on many parameters including the surface temperature and the thermal properties of the liquid and the substrate. The above model shows a reasonable match with measurements of the Leidenfrost layer thickness using a high magnification lens, and also agrees with other reported values in literature (Biance et al., 2003; Gottfried et al., 1966; Celestini et al., 2012; Aussillous, 2001). For a 5 μL water droplet at a surface temperature of 360°C, the measured Leidenfrost thickness is ~ 15 μm, which is a reasonable match with the predicted thickness of 9 μm.

Next, the effect of applying an electric field to suppress the Leidenfrost state is investigated. The mechanism underlying suppression can be understood by using the analogy of a parallel plate capacitor, which consists of two electrically conducting plates separated by a dielectric medium. These plates attract each other when the capacitor is charged. In the present application, the droplet meniscus acts as one of the plates, and can move in response to the applied electrostatic attraction force. It should be noted that the entire applied potential difference falls across the surface capacitance which is a series combination of the vapor layer and the dielectric layer capacitances.

The attraction force can be calculated by estimating the electrostatic energy (*E*) stored in the capacitance. The gradient of the electrostatic energy yields the electrostatic attraction force on the droplet as:

$$F_{attraction} = \frac{dE}{dz} = \frac{d}{dz}\left(\frac{1}{2}C_{eq}V^2\right) = -\frac{1}{2}\frac{\varepsilon_0\varepsilon_{vap}AV^2}{\left(L_v + \frac{\varepsilon_{vap}}{\varepsilon_d}L_d\right)^2} \tag{2.2}$$

In the above equation, C_{eq} is equivalent capacitance of the vapor layer and the dielectric), ε_0 is vacuum permittivity, (ε_{vap}, ε_d) are the dielectric constants of the (vapor, dielectric layer) and A is the footprint area of the droplet. Details of the derivation are provided in Appendix A.

Equation 2.2 predicts the Leidenfrost suppression force on the droplet and can be used to estimate the threshold voltage. Assuming, a lumped mass approximation for the droplet, the differential equation governing downward motion of the meniscus can be obtained as:

$$F_{attraction} + F_{weight} - F_{up} = m_{drop}\frac{d^2h}{dt^2} \tag{2.3}$$

in which h is transient vapor gap thickness. The solution of the above equation predicts the transient downward motion of the droplet upon the application of a potential difference. Figure 2.8 shows the transient response of the droplet to various voltages. At low voltages (Case a), the droplet is only slightly pulled towards the surface. It should be noted that the both the electrostatic attraction force and the vapor-pressure upward force will increase as the vapor layer becomes thinner. The electrostatic force scales as ~ $1/h^2$ whereas the upward force scales as ~ $1/h^4$. This implies that the liquid meniscus will ideally never touch the surface. In reality, there are a lot of secondary effects that take place during Leidenfrost suppression. It is observed that as the voltage increases, liquid fingers emerge from the liquid meniscus. These liquid fingers are the results of various instabilities in the vapor film and include electrostatic instabilities as well as Rayleigh-Taylor (Tong et al., 1997) instabilities in the meniscus. All these instabilities help to bridge the liquid-surface gap and complete the Leidenfrost state transition. For low voltages these instabilities are not strong enough, and the droplet bounces back upwards. At the threshold voltages, these instabilities are strong enough for the liquid to bridge the liquid-surface gap.

In view of the above complexities involved during suppression, a zone near the surface, which marks the boundary for successful Leidenfrost state suppression, is defined. If the applied voltage is sufficient to attract the liquid meniscus to this zone, Leidenfrost suppression is considered complete. In this study, Leidenfrost suppression was considered successful if the meniscus was attracted downwards at least 2/3rd of the initial gap as shown in Figure 2.8. Under these considerations, the predicted threshold voltage for 5 μL water droplets is about 85 Volts, as shown in Figure 2.8 (Case b). This threshold voltage is in reasonable agreement with the experimentally obtained threshold voltages (shown in Figure 2.3), given the limitations of a purely analytical model. Higher voltages will also successfully eliminate the Leidenfrost state and lead to a very rapid downward motion as shown in Figure 2.8 (Case c).

It should be noted that the above model is a first-order multiphysics analytical model which assumes a uniform flat meniscus and one dimensional planar transition. A detailed study of the suppression mechanism and instability analysis is included in chapter 3. It should also be noted that the model in this chapter is accurate for droplets smaller than the capillary length, and not for larger pools of liquids. Overall, the model is a very useful tool to understand the influence of geometry, material properties and the relative influence of various heat transfer mechanisms on Leidenfrost state suppression.

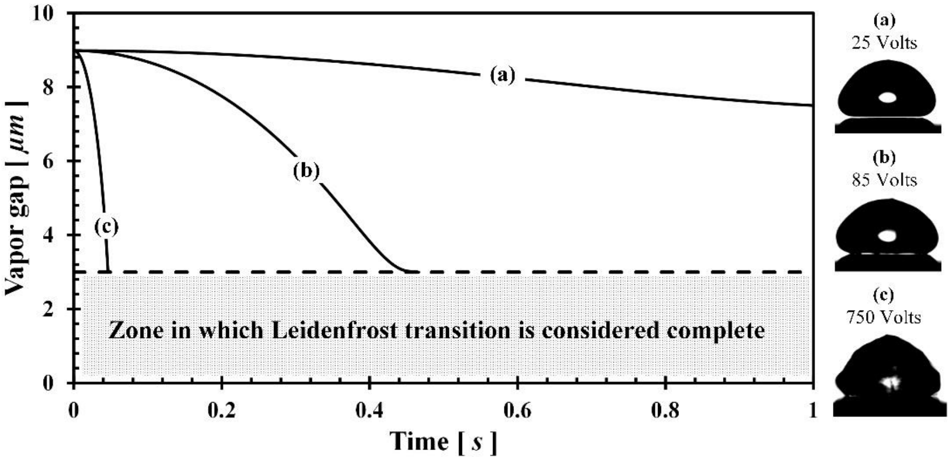

Figure 2.8. Influence of the applied voltage on Leidenfrost state suppression of 5 μL water droplets: (a) At low voltages (b) At the threshold voltage c) At higher voltages. Figure 2.8 reprinted with permission from Shahriari et al. Copyright 2014 American Chemical Society.

2.4. ELECTROSTATIC SUPPRESSION OF THE LEIDENFROST STATE USING AC ELECTRIC FIELDS [3]

This section analyzes the influence of AC electric fields on electrostatic suppression of the Leidenfrost state (previous sections utilized DC electric fields). In particular, the influence of the frequency of the AC waveform on Leidenfrost state suppression is analyzed using high speed visualization of liquid-vapor instabilities and heat transfer measurements of evaporating droplets. It is seen that the extent of suppression is reduced with increasing AC frequency. At sufficiently high frequencies, the influence of an applied

---

[3] Experiments on electrostatic suppression using AC electric fields were conducted jointly with another Ph.D. student, Onur Ozkan.

voltage is completely negated, and electrostatic suppression of the Leidenfrost state can be completely eliminated.

The influence of AC fields on Leidenfrost state suppression was studied by varying the AC frequency at a constant voltage. Figure 2.9 shows a set of isopropanol droplets at AC voltages (rms) of 60, 80 and 100 V, with varying frequencies. At 80 V DC (Figure 2.9a), instabilities and liquid fingers are clearly seen to protrude and bridge the vapor layer. The instabilities persist when the DC voltage is replaced by 80 V, 100 Hz AC voltage (Figure 2.9b). However, at 80 V, 1000 Hz, AC voltage, the instabilities disappear (Figure 2.9c), indicating that the Leidenfrost state is no longer suppressed. Exactly the same trend is observed at 100 V. Instabilities are seen at 100 V, 1 kHz AC (Figure 2.9d) and 100 V, 10 kHz AC (Figure 2.9e). However, no instabilities are observed at 100 V, 100 kHz AC (Figure 2.9f), indicating that the Leidenfrost state is not suppressed. The third row of Figure 2.9 shows the influence of AC frequencies at voltages below the threshold voltage. Figure 2.9g shows the vapor layer in the absence of any applied voltage and Figure 2.9h shows the vapor layer under the influence of 60 V DC. Below the threshold voltage (Figure 2.9h), the sinusoidal instabilities are not observed, although there are occasional disturbances at the liquid-vapor or liquid-air interfaces. However, the vapor layer thickness is less than the no voltage case (Figure 2.9g). Interestingly, at 60 V, 100 Hz AC (Figure 2.9i), the vapor layer is thicker than the DC voltage (Figure 2.9h), indicating that the electrostatic force on the droplet is reduced under AC electric fields.

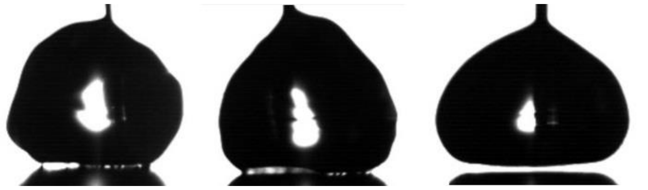

a. 80 V, DC b. 80 V, 100 Hz c. 80 V, 1000 Hz

d. 100 V 1 kHz e. 100V, 10 kHz f. 100V, 100 kHz

g. NO EW h. 60 V, DC i. 60 V, 100 Hz

Figure 1.9. Influence of AC frequency on suppression of the Leidenfrost state for isopropanol droplets. Figures 2.9a-c and Figures 2.9d-f show that the liquid-vapor instabilities reduce and eventually vanish as AC frequency is increased. At 60 V (less than threshold voltage), no instabilities are observed; however, an AC voltage (Figure 2.9i) results in a lower electrostatic force as compared to DC voltage (Figure 2.9h). Figure 2.9 reprinted with permission from Ozkan et al. Copyright 2017 AIP Publishing LLC.

Experiments indicate that frequency of the AC waveform can counter the applied voltage and can completely prevent suppression at high frequencies. Furthermore, the AC frequency required to negate the influence of the applied voltage, increases with the voltage. The physics underlying these observations can be understood by analyzing past studies (Jones et al., 2003; Jones et al., 2004; Kumari et al., 2008) on electrowetting-based droplet actuation using AC voltages. These studies reveal that the electric field penetrates inside the droplet as the AC frequency increases, thereby reducing the field strength. Similarly, the absence of a concentrated electric field in the vapor layer at high frequencies reduces the electrostatic force, thereby reducing the extent of suppression. At sufficiently high frequencies, an electrically conducting droplet behaves as an electrically insulating droplet, due to penetration of the electric field inside the droplet.

Another important finding in this work is the suitability of anodized aluminum as a dielectric for high temperature electrowetting applications. While there are multiple good polymeric dielectrics available (Chen et al., 2014) for room temperature electrowetting applications, most of them are not well-suited for high temperatures. Although the thickness (25 μm) of the dielectric (anodized aluminum) used presently was high, it exhibited pinhole-free, defect-free behavior at high temperatures. At 420 °C, the leakage current at 200 V was less than 1 μA in an electrowetting experiment with DI water. Repeating the experiment with a corrosive 1 M NaCl solution did not increase the leakage current. This dielectric did not exhibit a change in properties even after more than 10 hours of high temperature experiments.

2.5. CONCLUSIONS

It is demonstrated that electrostatic liquid attraction can be used to suppress film boiling and prevent surface dryout, even at ultrahigh temperatures exceeding 500 °C. Electric fields in the vapor layer can attract liquid towards the surface and promote wetting. Elimination of the vapor layer increases heat dissipation capacity by more than one order of magnitude. Heat removal capacities exceeding 500 W/cm^2 are measured for isopropanol, which is five times the critical heat flux (CHF) of water on common engineering surfaces. This principle constitutes a disruptive advancement in the field of boiling heat transfer by making the traditional CHF (critical heat flux) limit irrelevant, and enabling electrically tunable boiling heat transfer enhancement. The underlying science is explained via a multiphysics analytical model which captures the coupled electrostatic-fluid-thermal transport phenomena underlying electrostatic Leidenfrost state suppression. Furthermore, it is expected that electrostatic fields will also influence nucleate boiling by controlling boiling-related phenomena like bubble nucleation, growth and detachment. Electric fields are thus a very powerful tool for heat transfer enhancement across the boiling curve for liquids having finite electrical conductivities.

Leidenfrost state suppression using AC electric fields has also been investigated. It is seen that the frequency of the AC waveform is an important consideration in addition to the applied voltage. An increase in frequency can counter the influence of the applied voltage, due to penetration of the electric field inside the liquid. At high frequencies, the influence of the applied voltage is completely negated. Overall, this work uncovers the physics underlying dryout prevention and demonstrates electrically tunable boiling heat transfer with ultralow power consumption.

Chapter 3: Analysis of the Leidenfrost state suppression mechanisms [4]

This chapter discusses analysis of the mechanism underlying suppression of the Leidenfrost state. Liquids with finite electrical conductivity are considered, wherein the fluid remains equipotential and the entire potential difference falls across the vapor gap. The electrohydrodynamic instabilities occurring above the threshold voltage (that result in a wavy liquid-vapor pattern with a characteristic wavelength) are analyzed.

As mentioned in chapter 1, there are no studies on the instabilities associated with electrostatic suppression of the Leidenfrost state, where electrostatic forces are important in addition to surface tension and evaporation-induced pressure buildup. A reasonable starting point for the analyses of instabilities underlying Leidenfrost state suppression is existing studies on instabilities of thin films during electrohydrodynamic patterning (Schaffer et al., 2000; Gambhire et al., 2011; Yang et al, 2013; Elele et al., 2015; Mondal et al., 2014), which analyze electrostatic and surface tension forces. In this work, the distinguishing feature is the presence of evaporation that adds an additional stabilizing force and leads to a critical electric field for suppression. Through a combination of linear stability analysis and experimentation, the influence of material properties and surface temperature on the threshold electrical potential necessary to suppress the Leidenfrost effect are determined. Also the wavelength and time constant of the fastest growing mode of disturbance at the interface are predicted and analyzed.

---

[4] Analysis of the mechanism underlying suppression of the Leidenfrost state was conducted jointly with Prof. Roger Bonnecaze and Mr. Soumik Das. The contents of this chapter have been published in the following journal article: **Shahriari A**, Soumik D, Bahadur V, Bonnecaze R. (2017) Analysis of the instability underlying electrostatic suppression of the Leidenfrost state. Physical Review Fluids, 2, 034001.

3.1. EXPERIMENTAL METHODS

The experimental setup was previously described in chapter 2.1. Figure 3.1 shows a schematic of the experimental setup. Liquid droplets (5-100 μL were dispensed on a hot surface (unpolished aluminum wafer) above the Leidenfrost temperature using a micropipette. A thin wire connected to a power source is used to set the potential of the droplet relative to the substrate, while also restricting droplet mobility. The instabilities associated with Leidenfrost state suppression were visualized from the side using a high magnification camera.

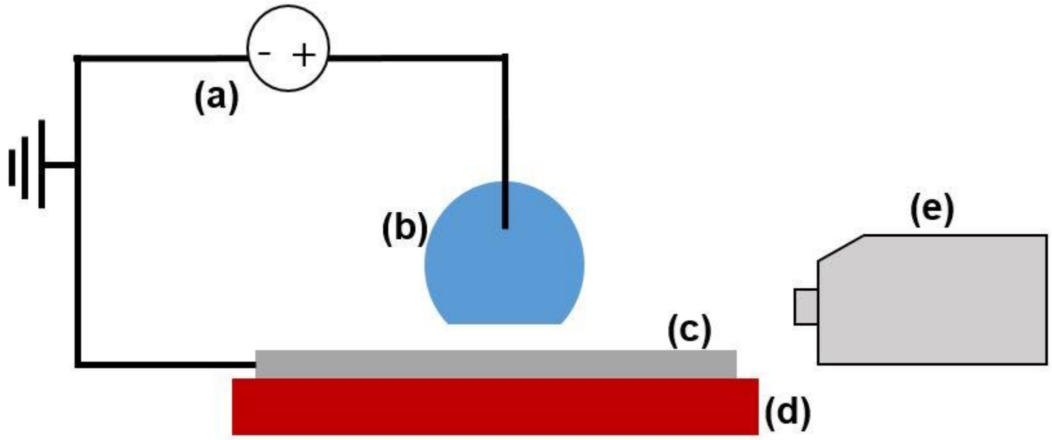

Figure 3.1. Schematic of experimental setup to visualize instabilities at the liquid-vapor interface: (a) power supply, (b) liquid droplet, (c) aluminum wafer, (d) hot plate and (e) high speed camera. Figure 3.1 reprinted with permission from Shahriari et al. Copyright 2017 American Physical Society.

Figure 3.2 shows the effect of an applied DC voltage on an isopropanol droplet (5 μL) on a hot surface at 400°C. In the absence of a voltage, the droplet will remain in a stable Leidenfrost state for many minutes. As the applied voltage is increased, undulations on the liquid-vapor interface are observed. Figure 3.2b shows four or five troughs or fingers, which tend to bridge the vapor gap. The voltage corresponding to the onset of this fingering is referred to as the threshold voltage. The undulations in Figure 3.2b are not steady state corrugations with finite amplitude. From the visualizations the wavy interfacial instabilities are time dependent, and travel due to the base flow of vapor from the center of the film to the outer perimeter or edge of the droplet. Due to limited resolution, it is not certain that all the undulations have the same amplitude all over the interface. Increasing the voltages results in more intimate liquid-solid contact (Figure 3.2c) and enhanced heat transfer.

It is hypothesized that there are several competing forces on the perturbed interface of the droplet as the voltage approaches its threshold value. The attraction (interface destabilizing) force is due to the electrostatic attraction between the charged fingers of a disturbance on the interface and the electrically grounded surface. There are two repulsive or stabilizing effects acting on these fingers. Firstly, there are capillary forces that smooth out disturbances at the interface, especially the high wave number disturbances (Oron et al., 1997). Secondly, as a finger gets closer to the interface, the rate of vaporization of the liquid increases locally and creates an additional stabilizing pressure to suppress the finger. If the applied voltage is large enough, the electrostatic forces dominate and the fingers will grow and bridge the vapor gap completely, enabling liquid-solid contact. Figure 3.3a shows a high magnification image of the liquid fingers completely bridging the gap.

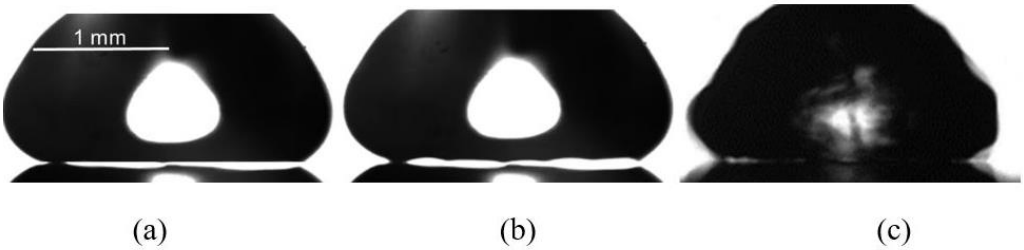

(a) (b) (c)

Figure 3.2. 5 μL isopropanol droplet on a hot substrate at 400°C. (a) Leidenfrost state in the absence of a voltage, $N_C = 10.93$, $N_H = 1.15$ and $N_E = 0$; (b) wavy instability at the liquid-vapor interface under the influence of an electrical voltage of 65 volts, $N_E = 2.52$; and (c) intimate liquid-solid contact at a higher voltage (130 volts), $N_E = 10.09$. Dimensionless numbers are defined in section 3.2. Note that a reflection of the droplets is also seen in the aluminum wafer below the vapor gap. Figure 3.2 reprinted with permission from Shahriari et al. Copyright 2017 American Physical Society.

3.2. MODELING INSTABILITIES ASSOCIATED WITH LEIDENFROST STATE SUPPRESSION

This section describes an analytical model to understand these competing forces and estimate the threshold voltage for suppression of the Leidenfrost state. Consider a radially axisymmetric vapor layer of thickness $h(r,t)$ between the bottom surface of the droplet and hot surface with an electrical potential V applied across the gap (Figure 3.3b). As discussed in chapter 2, droplet evaporation results in a pressure-driven radial flow from center to the edge (Figure 3.3), generating an upward force against the weight of the droplet and setting up the Leidenfrost state. The pressure field in the vapor gap depends on the evaporation, which in turn depends on the heat transfer to the droplet. In the presence of an electric field, the bottom surface of the droplet and the hot surface act as the plates of a parallel-plate capacitor, with the liquid being electrostatically attracted to the hot surface (Shahriari et al., 2014). A force balance which considers the weight of the droplet, the downward electrostatic force and the upward pressure force on the droplet predicts the base or undisturbed vapor gap thickness h_0.

In general, the dynamics of the thickness of the vapor film, the pressure field in the gap (P) and the evaporation rate are related by the thin film lubrication equation as (Oron et al., 1997):

$$\frac{\partial h}{\partial t} = u_{vap} + \frac{1}{12\mu r}\frac{\partial}{\partial r}\left(rh^3\frac{\partial P}{\partial r}\right) \tag{3.1}$$

where u_{vap} is the velocity of the vapor evaporating from the bottom of the droplet and μ is the viscosity of the vapor. The evaporation rate depends on the temperature difference between the droplet and surface, the conduction and radiative heat transfer, and the latent heat of vaporization of the liquid.

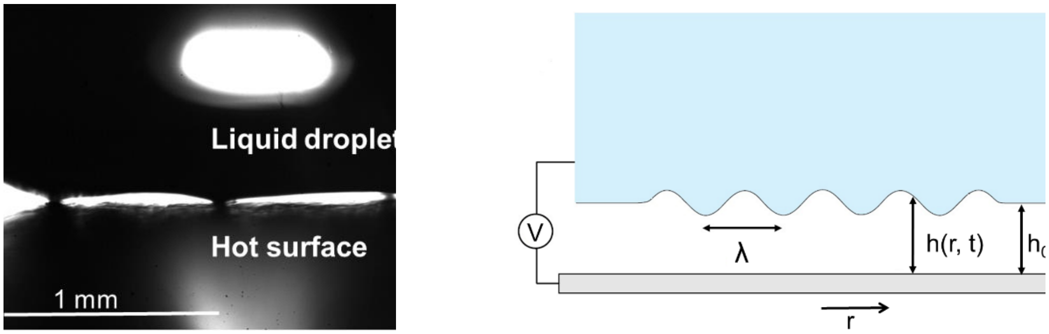

(a) (b)

Figure. 3.3. Interfacial instabilities upon the application of an electrical voltage. (a) Magnified view of instabilities below a liquid droplet on a hot surface. The capillary and evaporation numbers are NC=10.93, NH=1.15 and NE=2.52, respectively. (b) Schematic of the vapor gap and two-dimensional flow between the bottom of the droplet and the hot solid surface. h_0 is the initial vapor gap thickness and λ is the wavelength of a sinusoidal disturbance to the interface. Figure 3.3 reprinted with permission from Shahriari et al. Copyright 2017 American Physical Society.

In order to estimate normal velocity of vapor ejecting from the bottom meniscus of the droplet, all the thermal transport mechanisms must be taken into account (Figure 3.4). This has been done by Shahriari et al. (Shahriari et al., 2014) and is detailed in Appendix A. The evaporation from the bottom of the drop u_{vap} is given by:

$$u_{vap} = \frac{A_b \Delta T_{LF}\left(\frac{k_v}{h} + h_r\right) - A_t h_t \Delta T_t}{A_{tot} \rho_v \Delta H_v} \tag{3.2}$$

where h is vapor gap thickness, k_v is vapor thermal conductivity, h_r is the effective radiative heat transfer coefficient, $\Delta T_{LF} = T_{surface} - T_{drop}$ is the Leidenfrost superheat, $T_{surface}$ is the temperature of the hot surface, T_{drop} is the temperature of the drop, A_b is the flattened bottom surface of droplet, A_t is the top surface of droplet, $A_{tot} = A_b + A_t$, ΔH_v is latent heat of evaporation, ρ_v is the density of the vapor, h_t is the combined convective and radiative heat transfer from the top of the droplet, $\Delta T_t = T_{drop} - T_{ambient}$, and $T_{ambient}$ is the ambient temperature. Estimates of the heat transfer coefficients are found in Shahriari et al. (Shahriari et al., 2014) The base value of the evaporation u_{vap}^{0} is given by equation 3.2. with $h = h_0$ and is constant in space.

It is assumed that the droplet volume remains constant and the droplet is isothermal. The small (millimetric) droplet size, and low heat transfer coefficients (since the droplet is surrounded by vapor everywhere) imply the absence of significant temperature gradients within the droplet. It is noted that the electrical suppression of the Leidenfrost state is based on electrostatic attraction and does not involve the flow of large amounts of current. There is a small but finite amount of leakage current; however, the Joule heating associated with this current is negligible compared to the heat absorbed by the droplet (Shahriari et al., 2014). Convection within the droplet may influence the suppression with an applied voltage, but it is neglected here. The resulting predictions, as will be shown in section 3.3, match experimental observations very well.

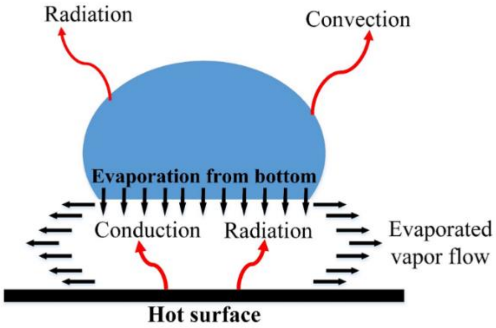

Figure. 3.4. Heat transfer modes involved in the Leidenfrost state. Figure 3.4 reprinted with permission from Shahriari et al. Copyright 2017 American Physical Society.

For a flat interface and radially axisymmetric flow in the absence of any disturbances, the base case satisfies:

$$u_{vap}^{0}+\frac{1}{12\mu r}\frac{d}{dr}\left(rh_{0}^{3}\frac{dP_{0}}{dr}\right)=0 \tag{3.3}$$

and the base pressure distribution P_0 in the vapor gap is given by:

$$P_{0}\left(r\right)=P_{atm}+\frac{3\mu R^{2}u_{vap}^{0}}{h_{0}^{3}}\left(1-\frac{r^{2}}{R^{2}}\right)+\frac{\varepsilon_{v}V^{2}}{2h_{0}^{2}} \tag{3.4}$$

where P_{atm} is the ambient atmospheric pressure, R is radius of the droplet, and ε_v is the electrical permittivity of the vapor. The second term in the above equation represents the pressure generated due to droplet evaporation, and the third term represents the electrostatic pressure upon the application of an electric voltage (Shahriari et al., 2014). It is noted that van der Waals forces are negligible since the vapor gap is a few microns thick prior to complete collapse of the film above the threshold voltage.

A small perturbation $\eta(r,t)$ to the interface is considered, so that $h(r,t) = h_0 + \eta(r,t)$. Assuming that $|\eta|/h_0 \ll 1$ and the pressure within the droplet is constant, the pressure P in the gap is now given by (Oron et al., 1997):

$$P = P_0(r) - \gamma \frac{1}{r}\frac{\partial}{\partial r}\left(r\frac{\partial \eta}{\partial r}\right) - \frac{\varepsilon_v V^2 \eta}{h_0^3} \tag{3.5}$$

where γ is liquid-vapor surface tension. The first term represents the base pressure field while the second term and third term represent the capillary and additional electrostatic pressures resulting from the wavy interface in the presence of the perturbation. Hydrostatic effects on the pressure for a vapor film are negligible compared to the capillary and electrostatic forces.

Substitution of the pressure distribution (equation 3.5) into the evolution equation of the interface (equation 3.1) yields the linearized form of the evolution of the disturbance to the interface as:

$$\frac{\partial \eta}{\partial t} = \left(\left.\frac{\partial u_{vap}}{\partial h}\right|_{h_0} \right)\eta - \frac{1}{12\mu r}\frac{\partial}{\partial r}\left(\frac{18\mu u_{vap}^0 r^2 \eta}{h_0} + \varepsilon_v V^2 r \frac{\partial \eta}{\partial r} + \gamma r {h_0}^3 \frac{\partial}{\partial r}\left(\frac{1}{r}\frac{\partial}{\partial r}\left(r\frac{\partial \eta}{\partial r}\right)\right)\right) \tag{3.6}$$

Next, a disturbance of the form $\eta(r,t) = \hat{\eta}(r) h_0 e^{st}$ is assumed, where s is the inverse time constant of the disturbance growth. Note from here forward, the radial position and time are made non-dimensional by scaling with R and h_0/u_{vap}^0, respectively. Substitution of this disturbance in equation 3.6 yields a fourth-order dimensionless eigenvalue equation for $\hat{\eta}(r)$ given by:

$$\frac{1}{N_c}\frac{1}{r}\frac{d}{dr}\left(r\frac{d}{dr}\left(\frac{1}{r}\frac{d}{dr}r\frac{d\hat{\eta}}{dr}\right)\right)+N_E\frac{1}{r}\frac{d}{dr}\left(r\frac{d\hat{\eta}}{dr}\right)+\frac{18}{r}\frac{d(\hat{\eta}r^2)}{dr}+12N_H\hat{\eta}=-12s\hat{\eta} \qquad (3.7)$$

where $N_C=\mu u_{vap}^0R^4/\gamma h_0^4$, $N_E=\varepsilon_V V^2h_0/\mu u_{vap}^0R^2$ and $N_H=-\left(h_0/u_{vap}^0\right)\left(\partial u_{vap}/\partial h\right)_{h_0}$. N_C and N_E are the dimensionless capillary and electroviscous numbers, which represent the relative magnitudes of viscous and interfacial forces, and electrostatic and viscous forces, respectively. N_H represents the sensitivity of the evaporation rate to the perturbations of the initially flat interface. A list of the physical parameters and ranges of experimental conditions and the resulting ranges of dimensionless N_C, N_H and N_E are shown in Table 3.1.

Parameter	Range of Values
Temperature	473 – 823K
Vapor viscosity, μ	10^{-5} – 1.7×10^{-5} Pa-s
Evaporation rate, u_{vap}^0	0.001 – 0.07 m/s
Droplet radius, R	10^{-3} – 3×10^{-3} m
Surface tension, γ	0.0196 N/m
Base vapor layer thickness, h_0	2×10^{-5} – 7×10^{-5} m
Vapor permittivity, ε_V	8.904×10^{-12} F/m
Voltage, V	40 – 80 V
$\left(\partial u_{vap}/\partial h\right)_{h_0}$	-15 – -4000 s^{-1}
N_C	8 - 250
N_H	1 – 1.5
N_E	0 - 20

Table 3.1. Ranges of physical parameters and dimensionless numbers N_C, N_H and N_E.

Equation 3.7 is an eigenvalue problem which is solved numerically by assuming flat interfaces at both ends and no net flow at the center, namely:

$$\left.\frac{d\hat{\eta}}{dr}\right|_{r=0}=0,\quad \left.\frac{d\hat{\eta}}{dr}\right|_{r=1}=0,\quad \left.\frac{d}{dr}\left(\frac{1}{r}\frac{d}{dr}\left(r\frac{d\hat{\eta}}{dr}\right)\right)\right|_{r=0}=0 \tag{3.8}$$

The fourth solvability condition is obtained from the zero force contribution of the perturbed pressure, under the assumption that the weight of the droplet is constant so that:

$$\int_{r=0}^{r=1} r\hat{\eta}(r)dr=0 \tag{3.9}$$

Equations 3.7 through 3.9 are solved numerically using a finite difference method to obtain eigenvalues s and the corresponding eigenfunctions. The sign of the real part of the eigenvalues determines the stability in the system for each mode of disturbance. Neutral stability corresponds to a vanishing real part of the eigenvalue for a disturbance given by its eigenfunction.

3.3. DISCUSSIONS

The real part of first few eigenvalues (Tables 3.2 and 3.3) and eigenfunctions (Figure 3.5) correspond to the conditions for a 5μL isopropanol drop at 200 °C and 500 °C, at different voltages (different N_E). The imaginary part of the eigenvalues represents a traveling wave that is due to the base flow from the center of the vapor gap outwards, but do not contribute to the growth or decay of the disturbance. The eigenfunctions plotted in Figure 3.5a and 3.5b are for the conditions in the middle columns of Tables 3.2 and 3.3, which correspond to the lowest value of N_E (lowest threshold voltage) for neutral stability, which occurs essentially for the mode 1 or mode 2 disturbance. The magnitudes of the eigenfunctions shown in Figure 3.5 were normalized according to:

$$\eta_{norm}(r) = \frac{\hat{\eta}(r)}{\left(\int_{r=0}^{r=1} \left| \hat{\eta}(r) \right|^2 dr \right)^{1/2}} \tag{3.10}$$

Disturbance mode	N_E =0.5	N_E =2.33	N_E =5
1	-31.25	0.0028	50.51
2	-81.04	-174.3	110.83
3	-368.57	-766.3	-291.1
4	-1092	-2115	-1388
5	-2614	-4536	-3507

Table 3.2. The real part of the first six eigenvalues for N_C = 28.13 and N_H = 1.44 for N_E = 0.5, 2.33 and 5.0. These values are typical for a 5μL isopropanol droplet at 200°C.

Disturbance mode	N_E =0.5	N_E =2.98	N_E =15
1	-36.18	0.0029	193.8
2	-282.9	-161.0	231.8
3	-1268	-1011	426.1
4	-3658	-3219	-1082
5	-8667	-7994	-4722

Table 3.3. The real part of the first six eigenvalues for N_C = 8.76 and N_H = 1.11 for N_E = 0.5, 2.98 and 15.0. These values are typical for a 5μL isopropanol droplet at 500°C.

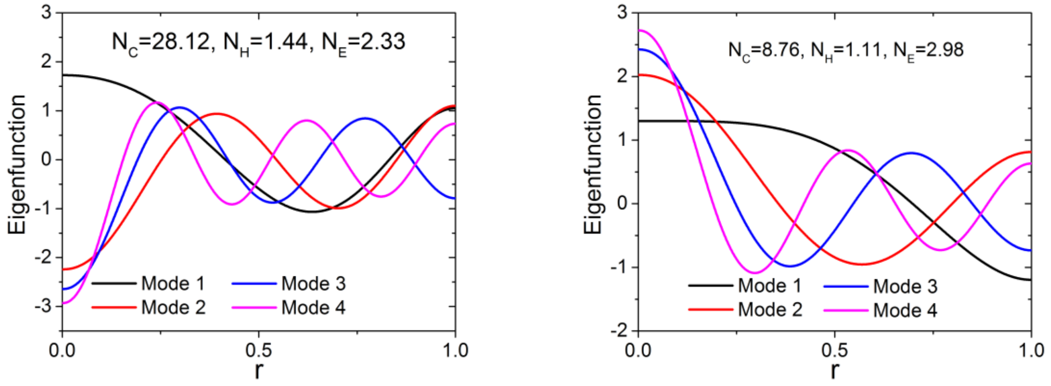

(a)

(b)

Figure 3.5. First four eigenfunctions for (a) $N_C = 28.12$, $N_H = 1.44$ and $N_E = 2.33$ and (b) $N_C = 8.76$, $N_H = 1.11$ and $N_E = 2.98$. Figure 3.5 reprinted with permission from Shahriari et al. Copyright 2017 American Physical Society.

Typical values of N_H and N_C range from 1-1.5 and 8-200. Eigenvalues with positive real components represent an unstable system where the applied voltage is high enough to initiate Leidenfrost suppression. The neutral stability curves in which the real part of s vanishes are shown in Figure 3.6.

A simple analytical solution can be obtained if the term $18r^{-1}d(\hat{\eta}r^2)/dr$ is neglected. This term is due to the advection of the base flow and only contributes to the imaginary component of the eigenvalue s and thus the traveling waves portion of the solution. It should not significantly affect the magnitude of the real part of s, as is indeed shown to be the case below. It is informative to study this simplified problem before reviewing the full numerical solution as it clearly reveals the competing physical effects that determine the threshold voltage. Upon neglecting the aforementioned term, equation 3.7 becomes:

$$\frac{1}{N_c}\frac{1}{r}\frac{d}{dr}\left(r\frac{d}{dr}\left(\frac{1}{r}\frac{d}{dr}r\frac{d\hat{\eta}}{dr}\right)\right)+N_E\frac{1}{r}\frac{d}{dr}\left(r\frac{d\hat{\eta}}{dr}\right)+12N_H\hat{\eta}=-12s\hat{\eta} \tag{3.11}$$

which allows a solution of the form $\hat{\eta}(r)=J_0(\lambda_n r)$, which is the zeroth order Bessel function. Here λ_n are the roots of the equation $J_1(\lambda_n)=0$. Although there are four linearly independent solutions of equation 3.11, $J_0(\lambda_n r)$ is the only eigenfunction that satisfies equation 3.11 and the boundary conditions. This approximate solution is qualitatively close in form to the numerically computed eigenfunctions of equation 3.7. The inverse time constant for the evolution of the disturbance is then given by:

$$s=\frac{u_{vap}^0}{h_0}\left(\frac{\lambda_n^2}{12}N_E-N_H-\frac{\lambda_n^4}{12N_C}\right) \tag{3.12}$$

Equation 3.12 clearly shows that the disturbances grow ($s>0$) with a sufficiently large electric field and are suppressed ($s<0$) by sufficiently large capillarity and evaporation. Note that for a vanishing electric field $N_E=0$, the vapor film is stable to all radial disturbances. The fastest growing mode occurs for the $\lambda_n \approx \sqrt{\frac{1}{2}N_E N_C}$ and $s_{\max}\approx\frac{u_{vap}^0}{h_0}\left(\frac{1}{48}N_E^2 N_C-N_H\right)$. These equations are approximate since λ_n are discrete. A neutral stability curve for $s=0$ is obtained when:

$$N_E=\frac{12N_H}{\lambda_n^2}+\frac{\lambda_n^2}{N_C} \tag{3.13}$$

Equation 3.13 estimates the non-dimensional electroviscous number as a function of evaporation and non-dimensional capillary forces introduced in equation 3.7. Based on this approximate model, it is seen that low frequency disturbances are stabilized by evaporation and high spatial frequency disturbances are stabilized by capillary forces. The neutral stability curves for different values of N_C and N_H are plotted in Figure 3.6.

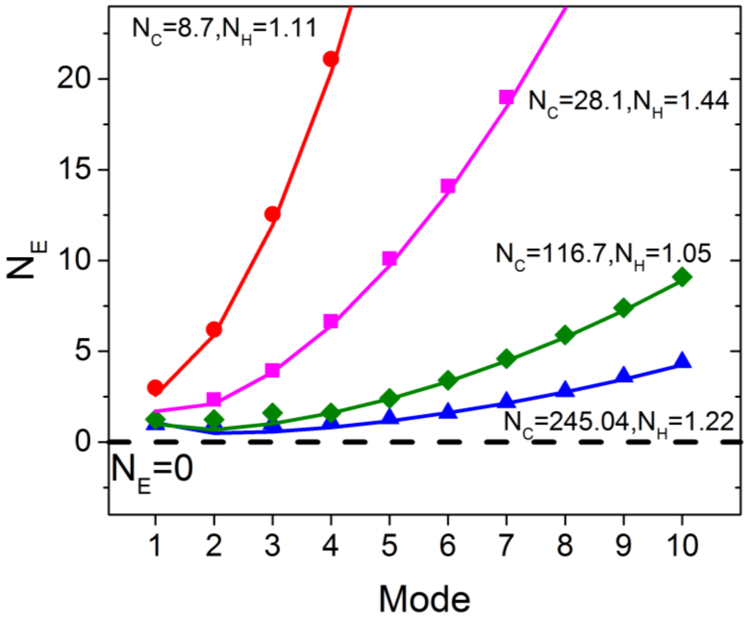

Figure 3.6. Neutral stability curve of the dimensionless electrostatic force versus the mode k for varying N_C and N_H. Symbols represent the numerical solution of the neutral stability point for a given mode. The solid lines correspond to the results based on the approximate theory represented by equation 3.13. Figure 3.6 reprinted with permission from Shahriari et al. Copyright 2017 American Physical Society.

Figure 3.6 shows the influence of various phenomena that determine the interface stability and Leidenfrost suppression. Firstly, it is noted that that for a given capillary and evaporation numbers, the Leidenfrost state will be suppressed for values of N_E above the curves of neutral stability. For values of N_E below the neutral stability curve, stable Leidenfrost states are predicted, namely the base state for the analysis. For the values of

N_E along the neutral stability curve, there are corresponding threshold voltages V_T above which surface instabilities will grow and the Leidenfrost state will be suppressed. Additionally, the neutral stability curves and the threshold voltages decrease with increasing capillary number. Secondly, the interplay of competing forces is reflected in the curves in Figure 3.6. At high spatial frequency or the mode λ_n of the disturbance, capillary forces dominate in stabilizing the vapor layer. In this case, the neutral stability curve increases quadratically with λ_n as predicted by equation 3.13. For low frequency disturbances evaporation becomes an additional stabilizing mechanism. Evaporation becomes the dominant mechanism at low frequencies when the capillary number is large. For medium frequency disturbances, both capillary and evaporation effects have a comparable influence in stabilizing the disturbance.

An estimate of the first mode to go unstable can be estimated from the λ_n that minimizes equation 3.13. For this $\lambda_n \approx \left(12N_H N_C\right)^{1/4}$ and the minimum electroviscous number, $N_E^{\min} \approx 4\left(3N_H / N_C\right)^{1/2}$. For typical physical parameters, $N_E^{\min}$ on the curves of neutral stability occur at low spatial frequencies, namely the first or second modes. These first two modes correspond to two or three fingers, respectively, along the film before they become unstable. Figure 3.2b shows about four to five fingers. While Figure 3.2b is representative of the fingers that form below the critical voltage, it cannot be concluded whether the image in Figure 3.2b is representative of the first mode that becomes unstable. The experimental setup was intended to determine the threshold voltage, but it is not at sufficient resolution to clearly identify the modes. Nonetheless, the theory accurately predicts the threshold voltage as is shown below.

Figure 3.7a depicts the variation of the threshold voltage with the volume of isopropanol droplets at two different surface temperatures. V_T is found to increase with increasing surface temperatures and droplet volumes because of the higher evaporation rates associated with these two factors. There is good agreement between the theoretical prediction and experimental observations. Figure 3.7b shows a comparison of the experimentally measured and theoretically predicted values of V_T for 5μL and 100 μL isopropanol droplets at different surface temperatures. The data here include results from (Shahriari et al., 2014) and additional experiments for this study. The agreement between theory and experiment is very good.

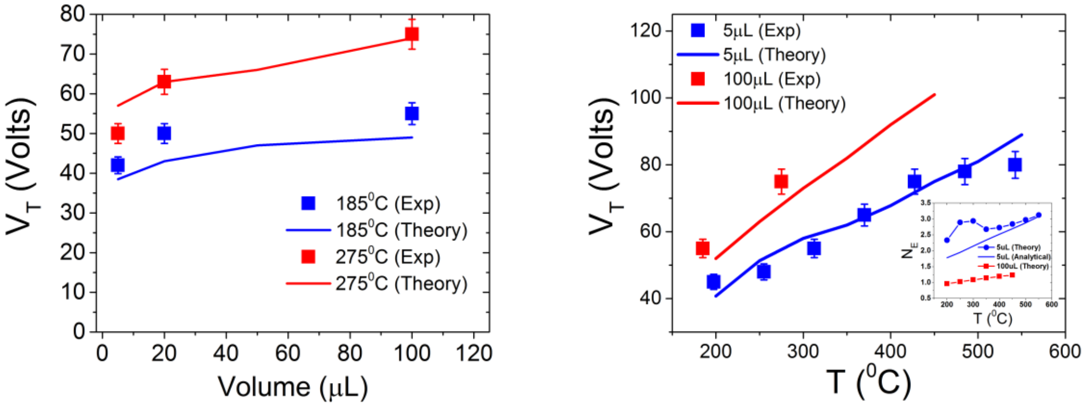

(a) (b)

Figure 3.7. Analytical and experimental measurements of the threshold voltage for suppressing the Leidenfrost state in isopropanol droplets: (a) Threshold voltage as a function of droplet volume (μL) for different surface temperatures (°C) and (b) threshold voltage as a function of surface temperature for a fixed droplet volume (5μL and 100μL). The reported results are the average of five or more measurements. The temperatures reported in this chapter are accurate to within ± 2°C and the droplet volume is accurate to within ± 3%. The data here include results from (Shahriari et al., 2014) and additional experiments for this study. The inset in (b) shows the dimensional N_E for the experimental conditions for the two droplets and the analytic prediction for the smaller drop extracted from equation 3.13. Figure 3.7 reprinted with permission from Shahriari et al. Copyright 2017 American Physical Society.

Note in Figure 3.7b there is a slight kink in the theoretical prediction of the threshold voltage for the 5 μL droplet but not for the 100 μL droplet. The origin of this can be deduced from the inset in Figure 3.7b, which plots the N_E at neutral stability, from which the threshold voltage is derived, as a function of temperature for the two droplet sizes and the analytic prediction for the smaller drop extracted from equation 3.13. For the smaller droplet, N_E has a small maximum, which gives rise to the kink in Figure 3.7b. No such behavior is observed for the larger droplets. The analytic prediction for the smaller drop (solid blue line in the inset of Figure 3.7b) is monotonically increasing. Thus, the origin of the kink is due to the traveling wave in the stability analysis, which was neglected in the analytic model. The traveling wave is suppressed for large N_C (high viscous forces and low capillary forces). Since $N_C \sim R^4$, viscous (capillary) forces are much higher (lower) for the larger droplet and so no kink is observed in Figure 3.7b.

3.4. CONCLUSIONS

In conclusion, it is demonstrated theoretically and experimentally that for a sufficiently high electrostatic potential on the droplet, the formation of the vapor layer is suppressed. The interplay of the destabilizing electrostatic force and stabilizing capillary force and evaporation determines the minimum voltage requirements (threshold voltage) to suppress the Leidenfrost effect. Linear stability theory accurately predicts threshold voltages for different size droplets and varying temperatures. The developed modeling framework shows a good match with experimental data, and identifies the electroviscous number as the key determinant of Leidenfrost state suppression. This approach does not utilize any fitting factors and is based on fundamental linear stability theory and thermal-fluid transport. It is noted that this model does not predict the Leidenfrost temperature, which will depend on properties of the fluid and the surface, along with surface texture and chemistry. This model also does not consider the influence of surface texturing and chemistry on suppression, since the solid-liquid contact is very small under threshold conditions. The model can be used for other fluids used in electrowetting studies such as deionized water and low electrical conductivity organic solvents. The model cannot be used for insulating liquids like oils or refrigerants, wherein the electric field diffuses into the droplet.

Chapter 4: Leidenfrost state suppression on deformable surfaces [5]

This chapter describes the first detailed study on electrostatic suppression of the Leidenfrost state on liquid substrates. Experiments and high-speed visualization reveal several interesting and non-intuitive aspects of Leidenfrost state suppression on liquids. It is seen that the nature of suppression is strongly dependent on properties of the liquid substrate, and can be fundamentally very different from that on a solid substrate.

Electrostatic suppression on silicone oil and Wood's metal (liquid alloy) is studied via experimentation, high-speed imaging and analyses. It is seen that the nature of electrostatic suppression can be drastically different from that on a solid substrate. Firstly, the Leidenfrost droplet completely penetrates into the silicone oil substrate, and converts to a thin film under an electric field. This is due to the existence of an electric field inside the substrate, and the deformability of the silicone oil interface. A completely different type of suppression is observed for Wood's metal and solid substrates, which have low deformability and lack an electric field in the substrate. Secondly, the minimum voltage to trigger suppression is significantly lower on silicone oil when compared to Wood's metal and solid substrates. Fundamental differences between these transitions are analyzed and a multiphysics analytical model is developed to predict the vapor layer thickness on deformable liquids. Overall, this study lays the foundation for further studies on electrostatic manipulation of the Leidenfrost state on liquids.

---

[5] The contents of this chapter have been published in the following journal article: **Shahriari A**, Ozkan O, Bahadur V. (2017) Electrostatic suppression of the Leidenfrost state on liquid substrates. Langmuir, 33 (46), 13207–13213.

4.1. EXPERIMENTAL METHODS

Electrostatic suppression of droplets of organic solvents such as isopropanol, acetone and methanol was studied in this work. Two nonvolatile liquids were used as the substrate, namely silicone oil and Wood's metal (which is a liquid metal). Wood's metal is also known as Lipowitz's alloy and is a eutectic alloy of bismuth, lead, tin and cadmium, with a melting point of 70 ºC. A schematic of the experimental setup is shown in Figure 4.1. The substrate liquid was maintained at a higher temperature than the boiling temperature of the droplet (82.5 °C for isopropanol). The thickness of the pool was varied by controlling the volume of liquid added to the reservoir. Pool temperature was controlled using a hot plate and surface temperatures were measured with an IR camera. As observed in a previous study (Maquet et al., 2016), liquid droplets attained the Leidenfrost state at lower superheats compared to that on a solid substrate.

Liquid droplets (isopropanol, acetone and methanol) were dispensed on the hot liquid substrate (above Leidenfrost temperature) using a micropipette. Droplets were dispensed while in contact with a 100 μm diameter aluminum wire, to restrict the mobility of the Leidenfrost droplet. The Leidenfrost state and the suppression dynamics were visualized from the side using a high-speed camera. Electrostatic suppression was achieved by applying a DC electric field in the vapor gap. The droplet was electrically biased using the wire holding it; the counter electrode was a flat aluminum sheet at the bottom of the substrate pool. This arrangement leads to an important and fundamental difference in the experiments with silicone oil and Wood's metal. Silicone oil is an insulator, and the applied voltage will be expressed across the vapor gap and the silicone oil substrate layer (droplet is considered equipotential, due to its relatively higher electrical conductivity as compared to the vapor layer and silicone oil). On the other hand, Wood's metal is electrically conducting; consequently, the substrate liquid remains equipotential and the entire voltage is expressed solely across the vapor layer.

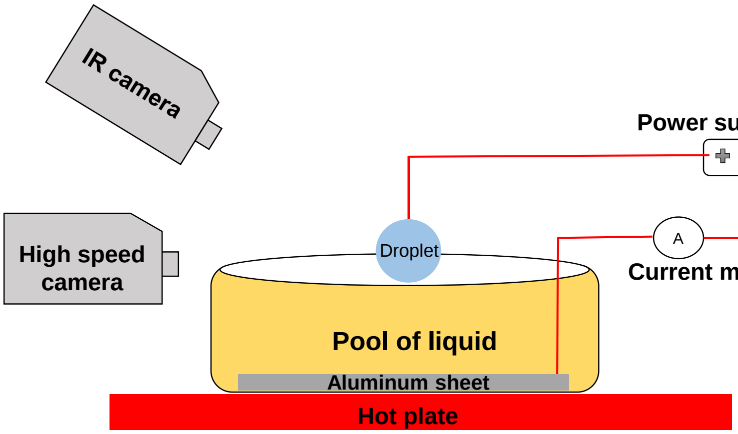

Figure 4.1. Experimental setup for studying electrostatic suppression of the Leidenfrost state on a liquid substrate. Figure 4.1 reprinted with permission from Shahriari et al. Copyright 2017 American Chemical Society.

Experiments were conducted with liquid droplets of volumes ranging from 5 µL to 3 mL. The temperature of the liquid substrate (as measured by an IR camera) was set at 150 ºC for silicone oil and 230 ºC for Wood's metal. All experiments were repeated multiple times and the reported results are the average of at least eight individual measurements. It is noted that the size of the liquid pool was more than ten times larger than the droplet size. Also, the Leidenfrost behavior of the droplets does not change as long as the substrate pool depth remains larger than the deformation of the liquid substrate.

4.2. RESULTS

This section discusses the results of experiments with silicone oil and Wood's metal as the substrate. On a silicone oil substrate, it is observed that droplets of organic solvents (isopropanol, acetone and methanol) retain their spherical shape at the expense of deformation of the silicone oil layer. This is evident in Figures 4.2a and 4.3e. The cross section is schematically shown in Figure 4.2b and is the basis for the analytical model developed in section 4.3.

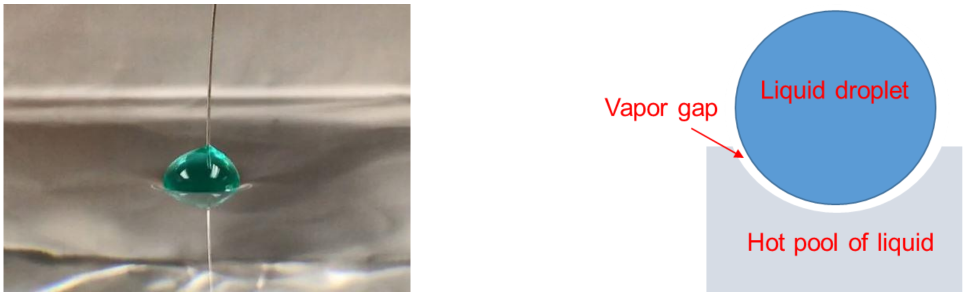

(a) (b)

Figure 4.2. (a) 10 µL isopropanol droplet levitating on top of silicone oil at 150 °C. Green dye is added to the droplet to improve visualization, (b) schematic showing the deformation of the silicone oil surface. Figure 4.2 reprinted with permission from Shahriari et al. Copyright 2017 American Chemical Society.

The nature of Leidenfrost state suppression is fundamentally different on silicone oil as compared to that on a solid substrate. Firstly, and most interestingly, the droplet completely loses its 'droplet-like' shape above the threshold voltage. It is attracted towards the liquid substrate, penetrates into the liquid substrate, rises back up as a thin film, and then evaporates (Figure 4.3). In contrast, on solid substrates, the same droplet will increase its wettability (which is voltage dependent), but will still retain its droplet characteristics (Figure 4.5b and 4.5c). The penetration of the droplet into the liquid substrate is remarkable since the density of the droplet (*e.g.* ~ 786 kg/m^3 for isopropanol) is less than that of silicone oil (~ 971 kg/m^3), indicating that the droplet impacts the surface with significant kinetic energy. Figure 4.3 shows side view snapshots of various stages of the suppression transition for isopropanol droplets. These transitions are also visible from the top by adding dye to the droplet (for contrast); it is clearly seen that the isopropanol droplet penetrates the silicone oil to a significant depth. This behavior is also clearly seen in high-speed videos of Leidenfrost state suppression. Very similar behavior was observed for methanol and acetone droplets as well.

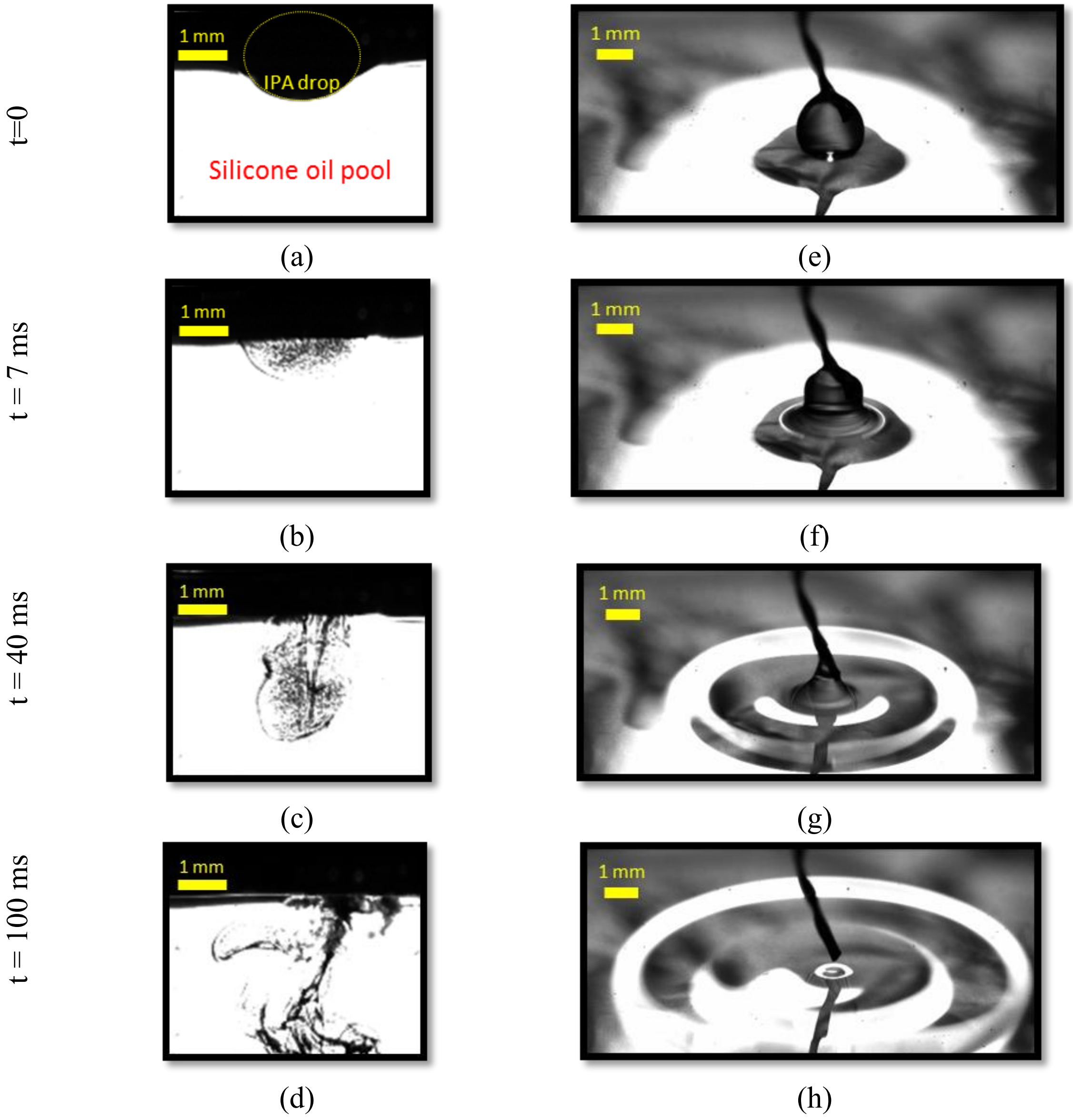

Figure 4.3. Sequence of images from the side (a-d) and from the top (e-h) depicting the suppression of the Leidenfrost state of a 10 µL isopropanol droplet on a silicone oil surface upon application of 20 V. Figure 4.3 reprinted with permission from Shahriari et al. Copyright 2017 American Chemical Society.

Secondly, the threshold voltages required for suppressing the Leidenfrost state on silicone oil are far lower than those on solid substrates. The threshold voltage was estimated by measuring the droplet lifetime on the superheated silicone oil pool. Droplet lifetime was defined as the time from the instant that the electrowetting voltage was applied to when the droplet completely evaporated/disappeared. Figure 4.4 shows the voltage-dependent lifetime of 10 μL isopropanol droplets on a pool of silicone oil at 150 °C surface temperature. The thickness of the silicone oil substrate was varied from 4 mm to 12 mm. The droplet lifetime is high in the Leidenfrost state as a result of reduced evaporation, which is a consequence of reduced heat pickup due to the low thermal conductivity of the vapor gap. As the applied voltage exceeds the threshold voltage, the droplet suddenly switches away from the Leidenfrost state, resulting in rapid heat absorption, evaporation and reduced lifetime.

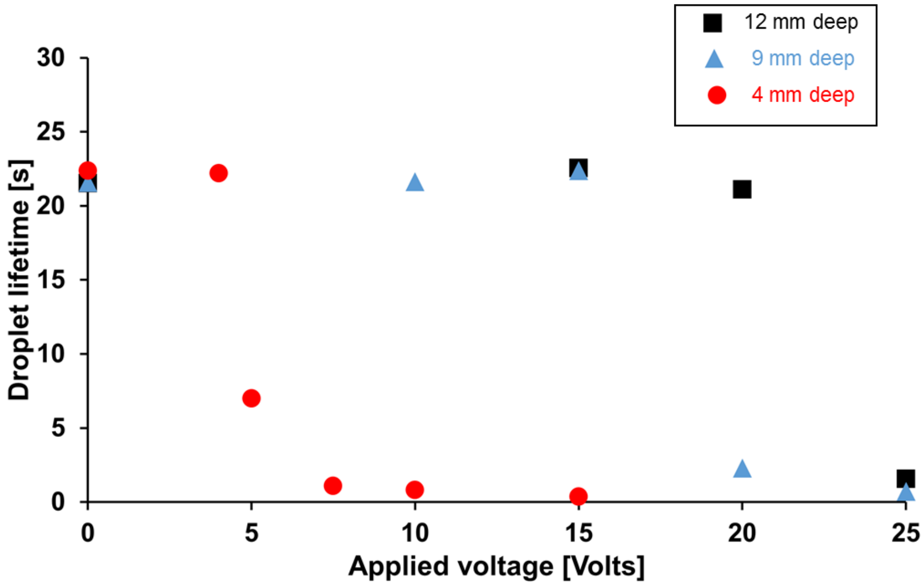

Figure 4.4. Lifetime of 10 μL isopropanol droplets on silicone oil (150 °C) for different depths of the silicone oil substrate. Figure 4.4 reprinted with permission from Shahriari et al. Copyright 2017 American Chemical Society.

From Figure 4.4, it is concluded that the threshold voltages are approximately 20 V, 15 V and 5 V for substrate/pool thickness of 12, 9 and 4 mm, respectively. These voltages are very low when compared to those on solid substrates, where threshold voltages range from 60-80 V (Shahriari et al., 2014; Shahriari et al., 2016a, Shahriari et al., 2016b; Shahriari et al., 2017a) for the same liquid droplets. More significantly, a majority of this applied potential difference will be expressed across the silicone oil layer, instead of across the vapor layer. It is noted that silicone oil is an insulator, and the applied voltage will be divided between the silicone oil and vapor layer. Assuming a representative average vapor layer thickness of 15 μm (as per the model developed in section 4.3), the actual potential difference between the vapor layer is expected to be only 0.062 V, 0.062 V and 0.046 V for substrate thickness of 12, 9 and 4 mm, respectively. A thicker silicone oil substrate does require a larger applied voltage; however, a majority of the voltage drop occurs across the silicone oil layer itself. The physical mechanisms responsible for the ultralow threshold voltage on silicone oil are not well-understood presently and possible explanations are discussed at the end of section 4.3.

Similar experiments were also conducted with Wood's metal substrate, with the surface temperature maintained at 230 ºC. In stark contrast to silicone oil, the nature of suppression was identical to that on solid substrates. Upon the application of an electrowetting voltage (above the threshold value), the droplet wetted and spread out on the surface as the Leidenfrost state was suppressed. More intimate solid-liquid contact results in rapid evaporation/boiling of the droplet. There was no loss of 'droplet shape' and no penetration of the droplet into the liquid metal substrate, unlike the case of silicone oil. Figure 4.5 compares the nature of Leidenfrost state suppression on silicone oil, Wood's metal and an aluminum surface. It is clearly seen that nature of Leidenfrost state suppression is similar for Wood's metal (Figure 4.5b) and aluminum (Figure 4.5c) and fundamentally different for silicone oil (Figure 4.5a). These features are also evident in comparison videos. Interestingly, the threshold voltage on Wood’s metal was observed to range from 60-80 V, which is identical (Shahriari et al., 2014; Shahriari et al., 2017a) to that on a solid surface, and much higher than that on silicone oil. It is noted that all temperatures reported in this work are accurate to within ±2 ◦C, and the droplet volume is accurate to within ±3%. The voltage measurements are accurate within ± 0.5 V. The measured results are droplet lifetimes, which are the average of five or more measurements, with standard deviations less than 1 second.

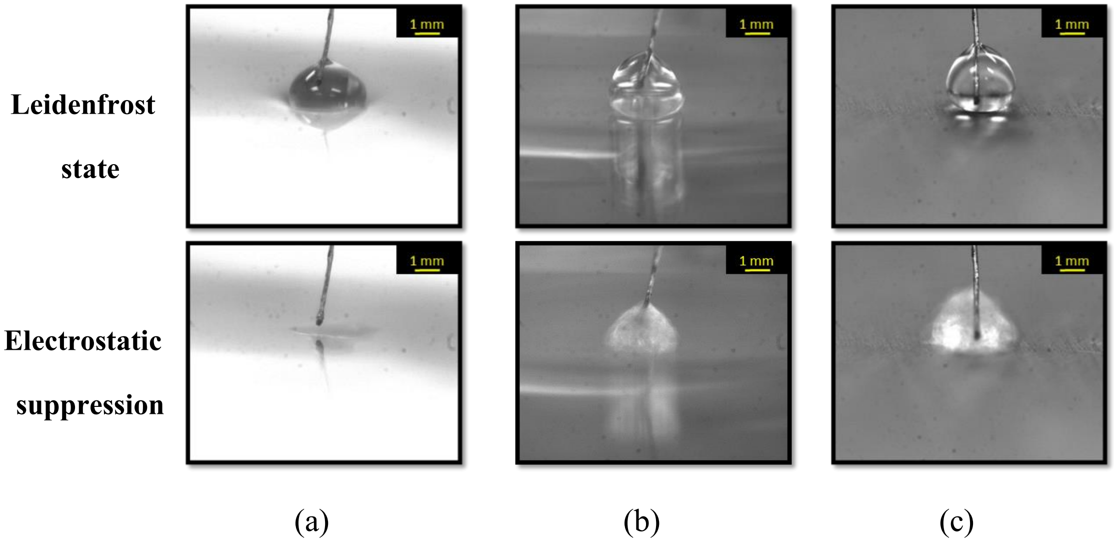

Figure 4.5. Nature of electrostatic Leidenfrost state suppression on different substrates: (a) deformable liquid (silicone oil), (b) liquid metal (Wood’s metal), and (c) solid (aluminum). On silicone oil, the droplet detaches from the top electrode, penetrates the substrate completely and eventually forms a thin film. On the other two substrates, increased droplet wettability is observed upon the application of an electric field. Figure 4.5 reprinted with permission from Shahriari et al. Copyright 2017 American Chemical Society.

4.3. DISCUSSIONS AND MODELING

This section describes various interfacial phenomena responsible for the contrasting nature of suppression on silicone oil, Wood's metal, and solid substrates. An analytical model of the Leidenfrost state on liquid substrates is developed. Two factors are responsible for the markedly different transitions on silicone oil and Wood's metal; namely the electric field distribution and the substrate deformability. Firstly, the significant penetration of the Leidenfrost droplet into the silicone oil substrate can be understood by considering the electric field in the system. There is a finite electric field inside the silicone oil substrate (Figure 4.6a), which will pull the droplet into the substrate and towards the bottom of the silicone oil pool (before the droplet has completely detached from the top electrode). On the other hand, there is no electric field inside the pool of Wood's metal (Figure 4.6b), which is electrically conducting, and therefore equipotential. There is thus no force to cause the droplet to penetrate into the Wood's metal substrate. The density and surface tension of silicone oil is also lower than Wood's metal, which makes it easier for the Leidenfrost droplet to penetrate into a silicone oil pool. It is noteworthy, that solid metal substrates (*e.g.* aluminum) also lack an electric field distribution in the substrate and are non-deformable. These common attributes with Wood's metal can explain the similar nature of electrostatic suppression in these two substrates.

It is noted that there is no electric field in the droplet in all cases, since isopropanol has much higher electrical conductivity than the vapor gap (and silicone oil). The droplet remains equipotential, and the electrode position does affect the electric fields. This has been confirmed in a recent study (Ozkan et al., 2017). For a silicone oil substrate, the entire applied voltage falls across the silicone oil and vapor gap (Figure 4.6a). For Wood's metal (and aluminum substrate), the voltage drop is concentrated in the vapor gap only (Figure

4.6b). A table of electrical properties of isopropanol and silicone oil is included in Appendix B.

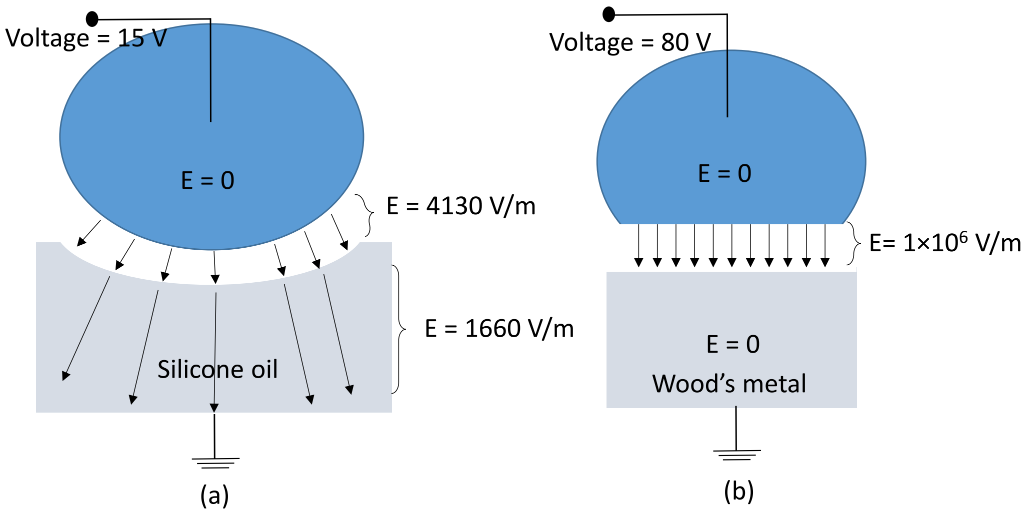

Figure 4.6. Electric field strengths in the droplet, vapor layer and substrate for (a) silicone oil substrate, and (b) Wood's metal substrate. The applied voltage corresponds to the threshold voltage. No electric field exists in the droplet and the substrate for case (b). Figure 4.6 reprinted with permission from Shahriari et al. Copyright 2017 American Chemical Society.

Secondly, the deformability of silicone oil is very different from that of Wood's metal. On silicone oil, the liquid substrate is substantially deformed, as evident in Figures 4.2a and 4.3e. On the other hand, the surface of Wood's metal is hardly deformed, similar to a solid substrate. The extent of deformability on these substrates is then quantified, which is an input to the Leidenfrost state model developed later in this section. The extent of deformation can be estimated using the results of a previous study (Shabani et al., 2013), which develops a fundamentals-based model to predict deformation of the interface between two liquids. The extent of deformation is correlated with the density ratio of the liquids and the Bond number. According to this model (Shabani et al., 2013), substrate deformation will be reduced as the Bond number decreases. In another study, Ding et. al. (Ding et al., 2016) studied deformation of liquid metal and solid substrates as a function of the Bond number. Based on this model, lower Bond numbers will result in lower deformation. In this section, these two models (Shabani et al., 2013; Ding et al., 2016) are used to predict deformation of silicone oil, Wood's metal and aluminum in contact with isopropanol droplets at Leidenfrost state. Table 4.1 shows the relevant comparisons. It is clearly seen that the low density and surface tension of silicone oil results in substantial substrate deformation as compared to the other two substrates. It is noted that other studies also model substrate/droplet deformation for different types of substrates (Janssens et al., 2017); their results are in line with experimental observations discussed in this dissertation.

Substrate	**Silicone oil**	**Wood's metal**	**Aluminum**
Density ratio ($\rho_{substrate}/\rho_{drop}$)	~1.25	~12.5	~3.5
Inverse of Bond number ($Bo = \left(\rho_{drop} g R^2\right)/\gamma_{substrate-air}$)	~0.3	~0.03	~0.02
Substrate deformation (Quantified in terms of θ_m which is the angular location corresponding to undeformed substrate)	Considerable (60 °)	Negligible (0.73 °)	Negligible (0.5 °)

Table 4.1. Estimate of deformation of substrate based on models from Shabani et al., 2013 and Ding et al., 2016.

In Table 4.1, γ is the surface tension, ρ_{drop} is density of the droplet, $\rho_{substrate}$ is density of substrate, g is gravity and R is droplet radius.

Next, an analytical model for the Leidenfrost state on a deformable silicone oil substrate is developed; in contrast there exist multiple models of the Leidenfrost state on solid substrates (Burton et al., 2012; Ng et al., 2016; Farokhnia et al., 2017; Shahriari et al., 2014; Shahriari et al., 2016a; Shahriari et al, 2017a). Upon gentle dispensing of an isopropanol droplet on hot silicone oil, the droplet will rest on the stretched free surface of silicone oil, which is deformed by the weight of the droplet. In other words, Leidenfrost droplets, smaller than the capillary length will maintain their spherical shape at the expense of deformation of the silicone oil substrate.

Figure 4.7 shows a schematic of a Leidenfrost droplet on a deformed silicone oil surface. It is assumed that the substrate surface will conform to the curvature of the spherical droplet and that the variation in vapor gap is negligible. The droplet radius is assumed to be *R*, vapor gap thickness is *h* and the radius corresponding to the substrate is *kR* where *k=1+h/R*.

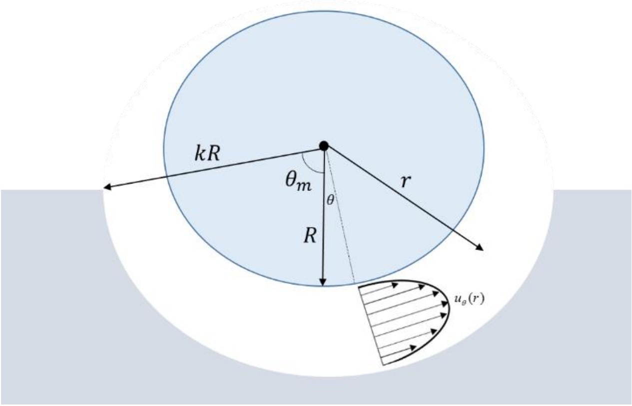

Figure 4.7. Geometry used in the development of the analytical model of the Leidenfrost state on deformable liquid substrates. Figure 4.7 reprinted with permission from Shahriari et al. Copyright 2017 American Chemical Society.

Vapor flow is responsible for pressure build-up in the vapor layer, which supports the droplet in the Leidenfrost state. Since the vapor layer thickness is significantly lower than droplet radius ($h << R$), classical lubrication theory is used to estimate the pressure distribution in the layer. A detailed derivation of the model is included in Appendix B and only the major equations are highlighted in in this section. With assumptions of steady state, incompressible, laminar and axisymmetric flow, the Navier-Stokes equation to estimate the velocity of Poiseuille flow in the vapor layer is:

$$u_\theta = \frac{1}{2\mu_{vapor}} \frac{\partial P}{\partial \theta} \left[r + \frac{kR^2}{r} - \left(k+1\right) R \right] \tag{4.1}$$

where u_θ is the angular velocity of the vapor, μ_{vapor} is dynamic viscosity of the vapor and P is the pressure buildup inside the vapor gap. Since $h << R$, $u_\theta = u_\theta(\theta, r)$ and $\frac{\partial P}{\partial \theta}$ is independent of radial location r.

Assuming uniform vaporization along the θ-direction and invoking mass balance conservation yields the pressure distribution as:

$$P(\theta) - P_{atm} = \frac{\mu_{vapor}}{R} \frac{\theta_m^2}{2k\ln(k) - \left(k^2 - 1\right)} \left(1 - \left(\frac{\theta}{\theta_m} \right)^2 \right) \overline{u_{vap}} \tag{4.2}$$

where P_{atm} is atmospheric pressure, θ is the angular coordinate along the vapor gap, θ_m is the angular location corresponding to undeformed substrate (Figure 4.7), and $\overline{u_{vap}}$ is the vaporization velocity. The uniform vapor layer and lubrication approximation is valid for $\theta<\theta_m$. Beyond θ_m, the free surface of the substrate starts to relax to a flat undisturbed line. Essentially, θ_m is a measure of substrate deformation, with the deformation increasing at larger values of θ_m. It is noted that since silicone oil is nonvolatile, pressure buildup is solely due to evaporation of the Leidenfrost droplet. Furthermore, effects related to mixing of the vapor and silicone oil, and Marangoni flows in the liquid substrate and droplet are not analyzed.

The evaporation rate from the droplet determines the magnitude of pressure buildup. Assuming 1D heat conduction in the vapor layer, the evaporation rate can be estimated as:

$$\overline{u_{vap}} = \frac{k\left(1-\cos\theta_m\right)}{2R\left(k-1\right)} \frac{k_{vapor}}{\rho_{vapor} h_{fg}} \left(T_{surface} - T_{sat}\right) \tag{4.3}$$

where k_{vapor} is the thermal conductivity of vapor, ρ_{vapor} is the density of vapor, h_{fg} is the latent heat of evaporation, $T_{surface}$ is surface temperature of the substrate and T_{sat} is the saturation temperature of droplet.

It is noted that the experimental observations suggest that $\theta_m = 60^\circ$, which is in agreement with recent studies (Janssens et al., 2017; Shabani et al., 2013). Integrating the vertical component of pressure over the effective area (up to an angle of 60º), provides the total upward force (which balances the droplet weight) as:

$$F_{vapor} = 0.37\left(\frac{k}{\left(k-1\right)\left(2k\ln(k) - \left(k^2-1\right)\right)}\right)\left(\frac{\mu_{vapor} k_{vapor}}{\rho_{vapor} h_{fg}}\right)\left(T_{surface} - T_{sat}\right) \tag{4.4}$$

The vapor layer thickness can be estimated by balancing the pressure force with the droplet weight. Since there is no liquid-liquid contact or triple line, surface energy terms are not included. The vapor layer thickness can be estimated using:

$$\frac{\left(\frac{h}{R}\right)^3}{1+\frac{h}{R}} = \left(\frac{0.088}{R^3}\right)\left(\frac{1}{\left(\rho_{droplet}-\rho_{air}\right)g}\right)\left(\frac{\mu_{vapor}k_{vapor}\Delta T_{LF}}{\rho_{vapor}h_{fg}}\right) \tag{4.5}$$

Based on equation 4.5, the magnitude of thickness of the vapor layer depends on the surface temperature, droplet size and the thermal properties of the droplet and its vapor. Figure 4.8 plots the vapor layer thickness as a function of the superheat for 10 µL isopropanol droplets on silicone oil. For a 67.5 °C superheat (as in present experiments), the predicted vapor layer thickness is ~18 µm. This thickness is significantly less than the 50-100 µm thickness of the vapor layer for Leidenfrost droplets of isopropanol on a solid aluminum surface, as predicted by (Shahriari et al., 2014). The differences can primarily be attributed to the geometrical differences between the two Leidenfrost situations.

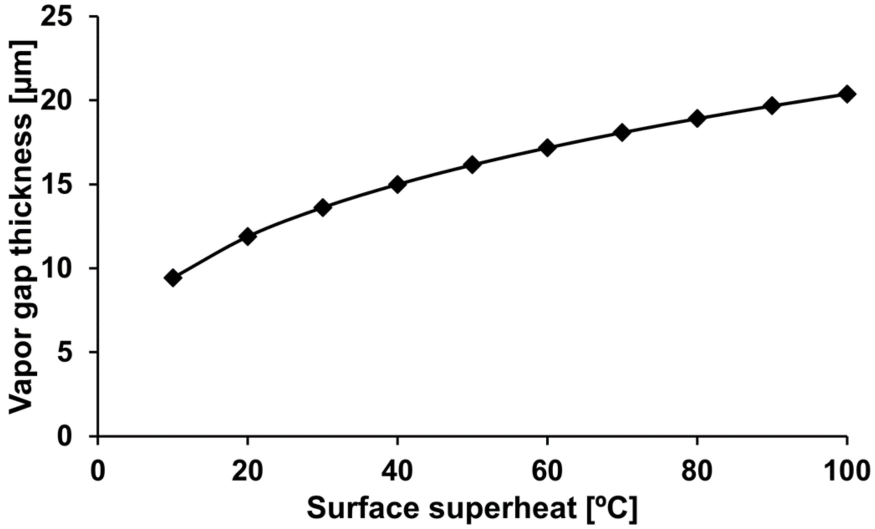

Figure 4.8. Vapor layer thickness for 10 µL isopropanol droplets in the Leidenfrost state on silicone oil at different superheats. Figure 4.8 reprinted with permission from Shahriari et al. Copyright 2017 American Chemical Society.

This considerable difference between the vapor layer thickness on solid and liquid substrates can partly account for the lower voltage requirements to suppress the Leidenfrost state on silicone oil. The electrostatic attraction force can be estimated from the total electrostatic energy stored in the vapor layer (for both liquid and solid substrates). Details of the derivation are provided in Appendix B. Assuming that the same force is required for suppression allows the comparison of the voltage requirements of the two cases as using:

$$\frac{1}{2}C_{liquid-liquid}V_{liquid-liquid}^{2}=\frac{1}{2}C_{liquid-solid}V_{liquid-solid}^{2} \tag{4.6}$$

where C is the capacitance and V is the applied voltage. First order estimates of the capacitances (using a parallel plate capacitor approach) reveal that the capacitance of the liquid-solid case is only 15% of liquid-liquid Leidenfrost case. This suggests that the required suppression voltage for the Leidenfrost state on a liquid substrate will be ~40% of that on a solid substrate.

While this analysis does suggest that the threshold voltage for suppression will be lower for silicone oil, it does not closely match the experimental results. This suggests that additional considerations/phenomena are at play, beyond those studied in this work. Firstly, it is noted that the model developed in this work assumes a constant vapor layer thickness, a perfectly spherical droplet and 1D conduction heat transfer in the vapor layer. Deviations from these assumptions will change the results. Also, electrostatic suppression on deformable substrates involves more complex interfacial phenomena, which are not accounted for in this model. Firstly, the substrate will deform under the influence of an electric field, which results in both the interfaces moving in a coupled manner during suppression. Secondly, there will be macroscopic natural convection currents setup in the liquid pool (with the strength of the convection current dependent on the substrate thickness). Analyzing these complex phenomena is beyond the scope of this work, which is primarily an experimental investigation of the phenomena underlying suppression.

4.4. INFLUENCE OF MARANGONI FLOWS ON THE LEIDENFROST STATE

Another key aspect of this work is the focus on surface tension gradients on the surface of the liquid (Leidenfrost droplet or liquid substrate), which actuate thermo-capillary driven Marangoni flows. The presence of Marangoni flows has non-trivial implications on the resulting thickness of the Leidenfrost vapor layer. The influence of Marangoni flows on the Leidenfrost state and vapor layer thickness on both solid and liquid substrates is briefly studied in this section. The pumping effect generated in the vapor layer due to Marangoni flows can significantly reduce the Leidenfrost vapor layer thickness (Shahriari et al., 2018).

The first-order analytical model to predict the Leidenfrost state vapor layer thickness provided in chapter 2, is further extended in this chapter to account for the influence of Marangoni flows. A detailed derivation of the model is provided in Appendix B and only the major equations are highlighted ahead.

In chapter 2, the Leidenfrost droplets resting on hot solid substrates were assumed to have an isothermal bottom surface. This is clearly not a good assumption, and the existence of temperature (and hence surface tension) gradients can lead to thermo-capillary driven Marangoni flows. The analysis starts with the steady state classical lubrication equation and follows the same criteria mentioned in chapter 2. Appropriate boundary conditions to estimate the vapor velocity profile are the existence of no-slip and Marangoni stress on the bottom interface (solid-liquid) and top interface (liquid-vapor) respectively, as follows:

$$u_r = 0 \quad @ z = 0 \tag{4.7a}$$

$$\mu \frac{du_r}{dz} = \frac{d\sigma}{dr} \quad @ z = h \tag{4.7b}$$

The influence of Marangoni actuated flows is inherent as a surface tension gradient term. This can be related to the temperature gradient on the bottom surface of the droplet as:

$$\left.\begin{array}{l} \sigma(T) = -aT + b \\ T(r) = T_c - mr \end{array}\right\} \Rightarrow \frac{d\sigma}{dr} = \frac{d\sigma}{dT}\frac{dT}{dr} = am > 0 \tag{4.8}$$

Following the procedure described in chapter 2, the force exerted on bottom surface of the liquid droplet with inclusion of the effects of the Marangoni flows is estimated as:

$$F_{vapor} = \underbrace{\frac{3\mu\pi R_b^4 \overline{u_{vap}}}{8h^3}}_{\text{vapor thrust}} - \underbrace{\frac{\pi a \Delta T_{marangoni} R_b^2}{2h}}_{\text{Marangoni thrust}} \tag{4.9}$$

It is evident that the upward force acting on the Leidenfrost droplet has two components: a force due to the vapor pressure buildup which scales as ($1/h^3$), and a Marangoni effect-related force which scales as ($1/h$). Furthermore, equation 4.9 shows that thermally driven Marangoni effects act to reduce the influence of the vapor pressure force. This is in concurrence with the physical picture that Marangoni flows help drain out the vapor in the layer.

Since the temperature at the outer edge of the droplet is lower, the surface tension is higher than at the center of the droplet (a linear decrease of surface tension with temperature is assumed in this work). This implies that the fluid will be pulled away from the center of the droplet towards the outer edges. This fluid motion will drag the vapor at the liquid-vapor interface along with it and hence augments drainage, resulting in a reduced thin film thicknesses. This is clear from equation 4.9, where the second term (which is the result of the Marangoni shear stress condition) is negative. Furthermore, the force acting due to the Marangoni effect depends strongly on the temperature (and hence the surface tension) gradient in the radial direction.

Figure 4.9 shows the variation of the Leidenfrost vapor gap thickness for a 10 μL isopropanol droplet as a function of surface super heat, with and without the influence of Marangoni flows. It is clearly seen that the inclusion of Marangoni stress reduces the predicted vapor gap thickness. Due to thermally driven shear stresses on the liquid surface, the radial velocity of the vapor flow is augmented. This leads to an enhanced drainage (favorable pumping effect) and hence reduces vapor layer thickness. Higher superheats will result in higher evaporation and thicker vapor layers; however, the analysis shows that thickness is not very sensitive to the Leidenfrost superheat.

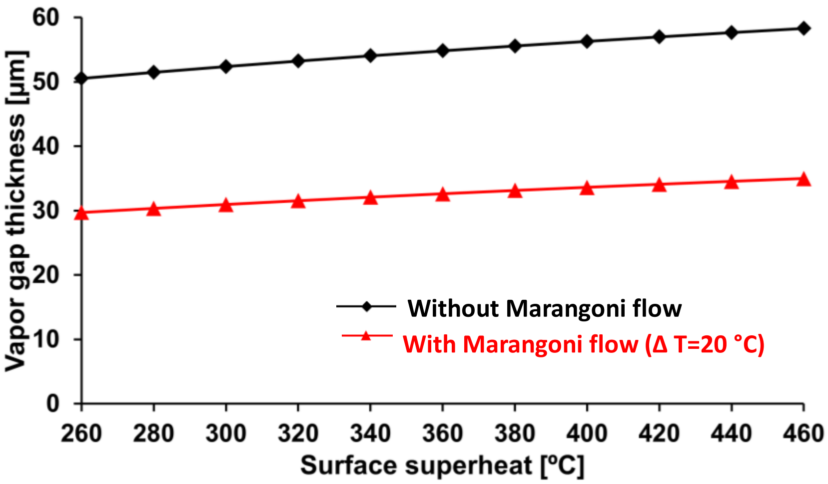

Figure 4.9. Vapor layer thickness for a 10 μL isopropanol droplet in the Leidenfrost state on aluminum surface at different surface superheats.

Figure 4.9 is based on a temperature difference ($\Delta T_{\text{Marangoni}}$ from the center to the edge of the droplet) of 20 ˚C. Figure 4.10 shows the influence of Marangoni temperature gradients on the vapor layer thickness.

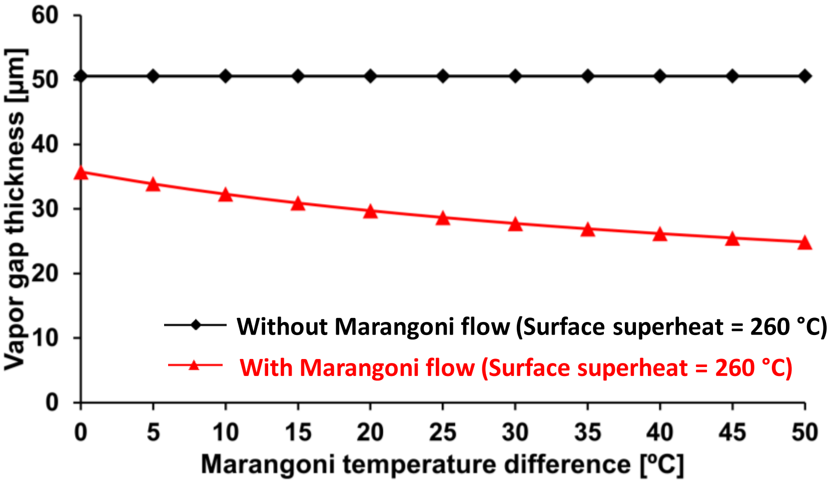

Figure 4.10. Vapor layer thickness for a 10 μL isopropanol droplet in the Leidenfrost state on an aluminum surface for various Marangoni temperature gradients.

There are two primary features of interest in Figure 4.10. The vapor layer thickness reduces with the inclusion of Marangoni stresses for all values of the Marangoni temperature gradient, which is evident from the offset between the two curves. This is due to the Marangoni stress condition applied at the top surface of the vapor layer which results in no shear stress condition (as opposed to no slip), even in the absence of temperature gradients.

For the case of Marangoni flows, it is seen that as the temperature gradient is increased, a non-trivial reduction in the vapor layer thickness is observed, which varies inversely with the magnitude of the temperature gradient. This is in agreement with the underlying physics governing the Marangoni shear stress condition wherein the vapor layer thickness decreases due to the augmented vapor pumping effect.

The influence of thermally-driven Marangoni flows on the Leidenfrost state on liquid substrates is further analyzed by using the same procedure mentioned earlier. The appropriate boundary conditions are:

$$\mu r \frac{d}{dr}\left(\frac{u_\theta}{r}\right) = \frac{1}{r}\frac{d\sigma}{d\theta} \quad @r = kR \quad \& \quad @r = R \tag{4.10}$$

A detailed derivation of the model is provided in Appendix B and only the major equations are highlighted in the following. The upward pressure force can be estimated as:

$$F_{vapor} = \underbrace{\frac{(1.48)R\mu\overline{u_{vap}}}{(k^2-1)}}_{\text{Vapor thrust}} - \underbrace{\frac{(3.83)Ram}{(k+1)}}_{\text{Marangoni thrust}} \tag{4.11}$$

A force balance including the droplet weight and the vapor pressure force yields the vapor layer thickness. Figure 4.11 shows the variation in the vapor layer thickness versus surface super heat, with and without the inclusion of Marangoni flows. As expected, an increase in surface super heat increases the evaporation rate and the vapor layer thickness. The inclusion of Marangoni flows in the analysis augments pumping in the vapor layer, and predicts a significant reduction of the vapor layer thickness. Importantly, the vapor layer thickness on liquid substrates is much smaller, as compared to solid substrates.

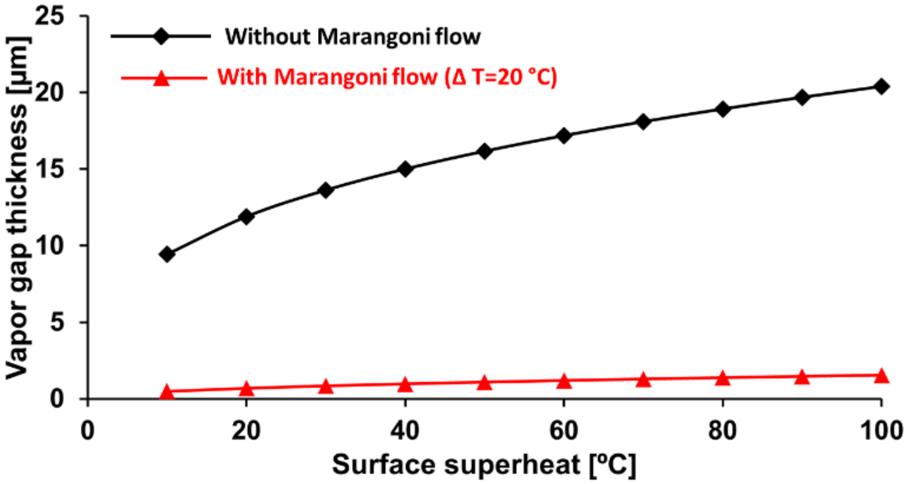

Figure 4.11. Vapor layer thickness for a 10 µL isopropanol droplet in the Leidenfrost state on a pool of silicone oil at different surface superheats.

Figure 4.12 shows the influence of the Marangoni temperature gradient on vapor layer thickness. It is seen that even small temperature differences result in a significant pumping effect, which reduces the vapor layer thickness significantly. This is a very significant prediction, and can explain a striking experimental result reported in this chapter. The voltages required to suppress the Leidenfrost state on a liquid substrate were 10X lower than the voltages required on a solid substrate. The present analysis explains the low voltage requirement on liquid substrates. Marangoni flows result in very low vapor layer thickness on liquid substrates (as compared to solid substrates).

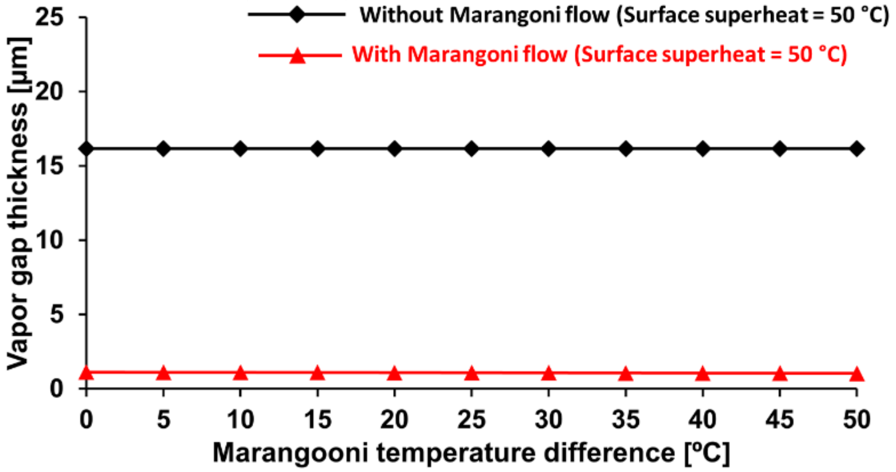

Figure 4.12. Vapor layer thickness for a 10 µL isopropanol droplet in the Leidenfrost state on silicone oil for various Marangoni temperature gradients.

4.5. CONCLUSIONS

In conclusion, this study analyzes various interfacial phenomena underlying electrostatic suppression of the Leidenfrost state on liquid substrates. It is seen that the nature of suppression is strongly dependent on the electrical properties and deformability of the substrate. On non-conductive, deformable substrates, the Leidenfrost droplet can completely penetrate inside the substrate and lose its ‘droplet-like’ shape. On the other hand, for electrically conducting and low deformability liquid substrates, the nature of electrostatic suppression is similar to that on solid metal substrates. Importantly, the voltage requirement for suppressing the Leidenfrost state is significantly lower for deformable liquid substrates. The differences between these transitions is studied and an analytical model of the Leidenfrost state on deformable liquid substrates is developed. It is also shown that thermally driven Marangoni flows have non-trivial implications on the resulting Leidenfrost vapor layer thickness. It is shown that temperature gradients, which are responsible for the Marangoni flow enhance the drainage in the vapor layer, and significantly reduce the vapor layer thickness (especially for the Leidenfrost state on liquid substrates). Overall, this study will enable several follow on efforts on the Leidenfrost state on liquids, with applications in microfluidics, energy, material processing and fire suppression.

Chapter 5: Experimental study of Leidenfrost state suppression during quenching [6]

This chapter studies the physical mechanisms underlying electrically-induced elimination of film boiling during quenching. EW-induced disruption of the vapor layer is experimentally analyzed, and the resulting enhanced cooling during the process of quenching is measured. Temperature measurements and visualizations are used to analyze boiling patterns upon the application of an interfacial voltage. The threshold voltage to disrupt the vapor layer and the upper limit on cooling rate enhancement are experimentally measured.

It is seen that EW can fundamentally alter the classical cooling curve and enable electrically-tunable quenching. Heat conduction across the vapor gap is replaced with transient convection. This fundamental switch in the heat transfer mode significantly accelerates cooling during quenching. An order of magnitude increase in the cooling rate is observed, with the heat transfer seen approaching saturation at higher voltages. An analytical model is developed to extract voltage dependent heat transfer rates from the measured cooling curve. The results show that electric fields can alter and tune the traditional cooling curve. Overall, this study presents an ultralow power consumption concept to control the mechanical properties and metallurgy, by electrically tuning the cooling rate during quenching.

---

[6] The contents of this chapter have been published in the following journal article: **Shahriari A**, Hermes M, Bahadur V. (2016) Electrical control and enhancement of boiling heat transfer during quenching. Applied Physics Letters, 108, 091607.

5.1. EXPERIMENTAL METHODS

Classical quenching experiments were conducted, with provisions for introducing an electric field across the vapor layer as shown in Figure 5.1. High temperature-corrosion resistant 316 stainless steel spheres (7/8” diameter) and copper spheres (1” diameter) were quenched in an isopropanol bath (saturation temperature 82.5 °C). The sphere was instrumented with an ungrounded K-type thermocouple at the center. A separate metallic lead was used to bias the sphere. The potential difference across the vapor layer was established using a ground electrode immersed in the bath. The experiments involved heating the sphere (outside the bath) to 400 °C, immersing it in the bath and turning on the voltage (maximum 2 kV DC). The temperature of the sphere center was measured during the quenching process and the sphere was imaged from the side to visualize the boiling patterns. The current flow in the circuit was recorded to estimate the power consumption required to suppress the film boiling.

While this work reports results of the above experimental configuration, additional experiments were conducted with different sphere metals (chrome-alloy steel), working fluids (ethylene glycol), sphere sizes (0.5”, 1.5”), and temperatures (ranging from 400-800 °C). The repeatability of the results strengthens the findings and demonstrates the robustness of this concept, and highlights the wide applicability of this work. In particular, electrically enhanced quenching works with deionized water; however, this enhancement is complicated by the simultaneous electrolysis of water, and is not discussed in this work. Organic solvents (like isopropanol) on the other hand, have much lower electrical conductivity than water, and show robust film boiling suppression at temperatures as high as 800 °C (Shahriari et al., 2014).

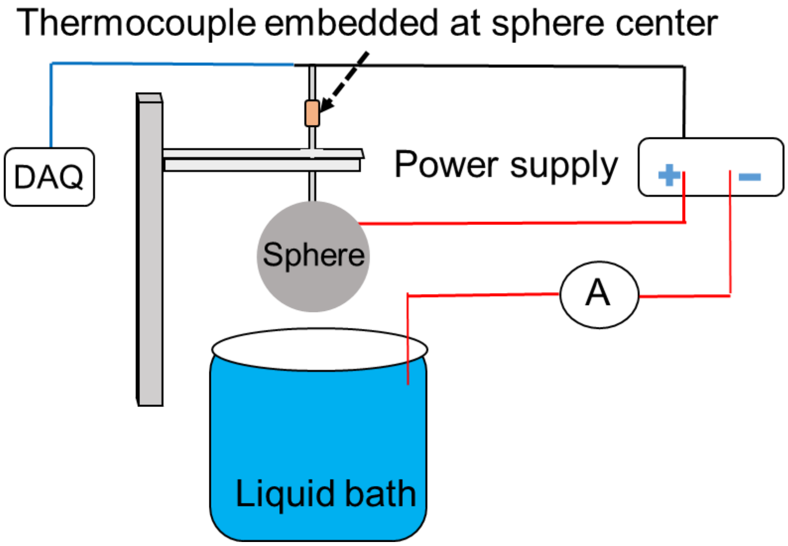

Figure 5.1. Schematic of the setup for the study of electrically-enhanced quenching. Figure 5.1 reprinted with permission from Shahriari et al. Copyright 2016 AIP Publishing LLC.

Figure 5.2 depicts various stages of boiling associated with quenching from 400 °C in the absence (Figures 5.2a-e) and presence (Figures 5.2f-j) of an EW voltage (500 Volts). In the absence of an EW voltage, a stable Leidenfrost layer forms immediately (Figure 5.2a and 5.2b), and persists for ~35 seconds till the sphere cools to ~ 210 °C (Figure 5.2c). An EW voltage however, disrupts the vapor layer immediately (Figure 5.2g), as seen from vigorous bubbling from the surface. Under an EW voltage, the surface sees liquid and vapor alternately, as liquid is electrostatically attracted towards the surface, but is then rapidly vaporized. This mode of boiling is referred to as transition boiling (Carey, 2007) as opposed to film boiling (Leidenfrost state). Increased wettability enhances heat transfer, and cools the electrowetted sphere faster. The differences in boiling modes are evident in Figure 5.3.

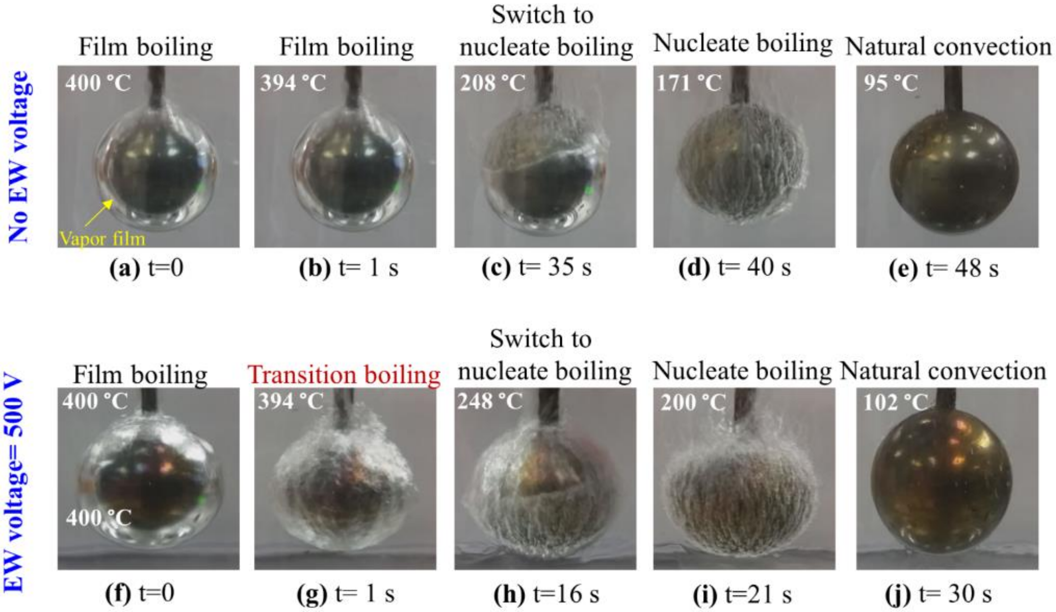

Figure 5.2. Snapshots showing boiling patterns on non-electrowetted (a-e), and electrowetted (f-j) spheres. The Leidenfrost vapor film is disrupted immediately (g) in the electrowetted sphere, and collapses entirely in 16 seconds (h). Natural convection sets in starting at 30 seconds (j). For the non-electrowetted sphere, a stable Leidenfrost layer persists much longer till 35 seconds (c), and natural convection sets in at 48 seconds (e). Overall, much faster cooling is observed for the electrowetted sphere. Figure 5.2 reprinted with permission from Shahriari et al. Copyright 2016 AIP Publishing LLC.

The electrowetted sphere sees a switch to nucleate (Carey, 2007) boiling mode at ~ 250 °C at 16 seconds (Figure 5.2h), wherein the disrupted vapor layer is seen to completely and rapidly collapse within a timeframe of ~ 1 second (Figure 5.3). Nucleate boiling is characterized (Carey, 2007) by smaller, isolated bubbles that convect heat. In the non-electrowetted sphere, this switch to nucleate boiling happens much later at 35 seconds (Figure 5.2c). As the non electrowetted sphere cools further, bubble formation slows down and eventually stops at a temperature of ~ 100 °C (Figure 5.2e). Subsequently, the sphere cools by natural convection currents setup in the bath. It is noted that the switch to natural convection happens much earlier for the electrowetted sphere (30 seconds) as opposed to the non-electrowetted sphere (48 seconds); this is a consequence of the electrowetted sphere cooling faster in the early stages.

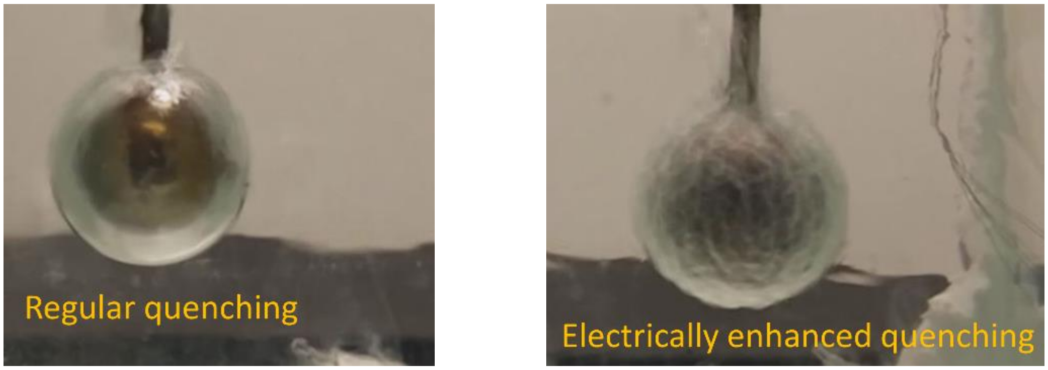

(a) (b)

Figure 5.3. Comparison of quenching in the absence (a) and presence (b) of an electrowetting (EW) voltage. An EW voltage disrupts the vapor layer by promoting wetting and enables faster cooling. The non electrowetted sphere sees a vapor film (Leidenfrost state) for a long time. Figure 5.3 reprinted with permission from Shahriari et al. Copyright 2016 AIP Publishing LLC.

5.2. RESULTS

The fundamental change in the boiling patterns also alters the heat transfer rates. Figure 5.4 shows the cooling curves (sphere center temperature versus time) for 0, 500, 1000 and 2000 Volts. It is clearly seen that EW voltages shift the cooling curve and enable faster cooling. The switch between various boiling patterns is marked on each curve. For the non-electrowetted case, heat transfer sequentially involves the film boiling, nucleate boiling and natural convection modes. For the electrowetted cases, the film boiling mode is replaced by transition boiling, and is followed by nucleate boiling and natural convection. This fundamental switch in the initial phase of quenching alters the cooling curve. Heat transfer increases at higher voltages; however, the gains saturate at high voltages. This can be explained by observing that there is a limit to wettability, which will not keep on increasing with higher voltages. Experiments were also conducted to measure the threshold voltage needed to disrupt the vapor layer. The threshold voltage was determined by visual observations of the vapor layer disruption and was observed to range from 80-100 Volts. It should be noted that the curves in Figure 5.4 are the average of at least 3 experiments; the error in these measurements is estimated to be less than 6%. Details of the uncertainty analysis are provided in Appendix C.

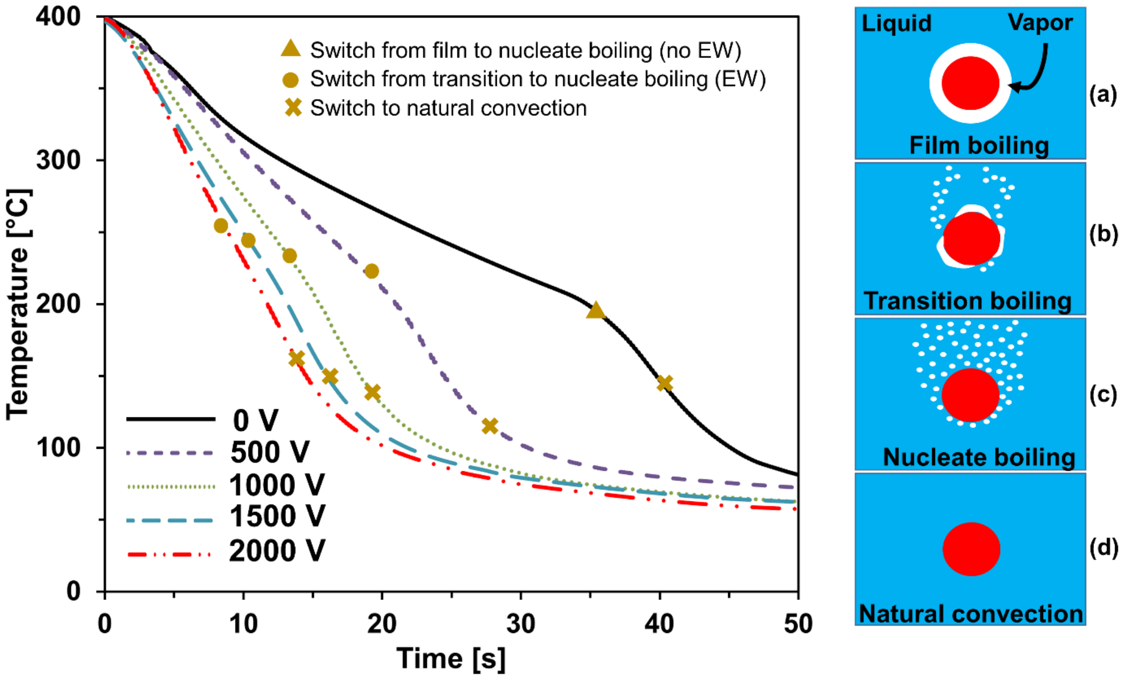

Figure 5.4. Electrically tunable cooling curves showing voltage dependent cooling rates. An EW voltage modifies the boiling patterns, which are depicted schematically in (a)-(d). The points where boiling patterns change are marked on the cooling curves. Figure 5.4 reprinted with permission from Shahriari et al. Copyright 2016 AIP Publishing LLC.

It should be noted that copper spheres can be considered isothermal, due to high thermal conductivity of copper (~ 400 W/mK). However, stainless steel spheres are not isothermal due to low thermal conductivity of stainless steel (~ 15 W/mK). An analytical model (Faghri et al., 2010) is employed to estimate the surface temperature from the center temperature, which can then be used to estimate convective heat transfer rates. This model is based on a solution of the unsteady heat diffusion parabolic equation with convective heat transfer boundary conditions. The dimensionless form of this equation is (Faghri et al., 2010):

$$\frac{1}{r^*}\frac{\partial^2(r^*\theta^*)}{\partial r^{*2}} = \frac{\partial\theta^*}{\partial Fo}, \tag{5.1}$$

where $\theta^* = \frac{T-T_\infty}{T_i-T_\infty}$ is dimensionless temperature, $r^* = \frac{r}{r_0}$ is dimensionless radial position and $Fo = \frac{\alpha t}{L_c}$ is dimensionless time. T is the temperature at radial position r, T_∞ is the bath temperature, T_i is the initial temperature of the sphere, α is the thermal diffusivity of the sphere, t is time and L_c is the characteristic length of the sphere (r_0). The above equation can be solved analytically and the radial temperature θ^* and center temperature θ_0^* can be obtained as (Faghri et al., 2010):

$$\theta^* = \theta_0^*\frac{1}{\xi_1 r^*}\sin(\xi_1 r^*), \tag{5.2}$$

$$\theta_0^* = C_1\exp(-\xi_1^2 Fo), \tag{5.3}$$

In the above equations ξ_1 and C_1 are constants which are estimated analytically. Details of the derivation are provided in Appendix C. The center temperatures reported in Figure 5.4 can be translated to surface temperature using equations 5.2 and 5.3. Figure 5.5

compares the cooling curves based on center and surface temperatures for 0 and 2000 Volts. It is seen that the effect of an EW voltage on the cooling curve is more pronounced when surface temperatures are compared. The direct outcome of increased wettability is an increase in the surface heat flux. This increased heat transfer will enhance the temperature gradient within the sphere. The contrast between the surface and center temperatures can then be attributed to the transient conduction temperature profile. Comparison of surface cooling indicates a nine-fold enhancement in the initial cooling rate, from 4 °C /s in the absence of an EW voltage to 36 °C /s at 2000 Volts. The corresponding enhancement in the center cooling rate is a factor of 3, from 4 °C /s (no voltage) to 13 °C /s (2000 Volts). It should be noted that the error in the predicted surface temperatures is estimated to be less than 7%. Details of the uncertainty analysis are provided in Appendix C.

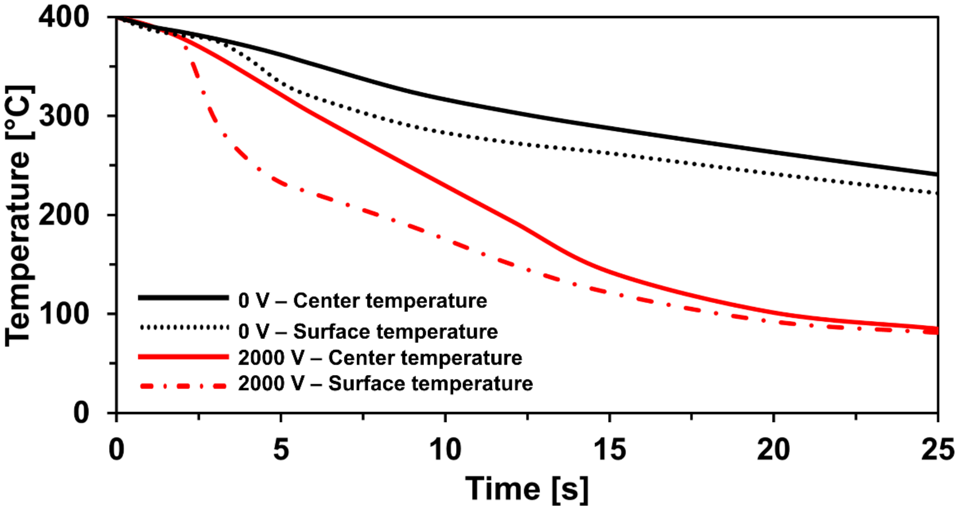

Figure 5.5. Electrically tunable cooling curves based on center and surface temperatures. Figure 5.5 reprinted with permission from Shahriari et al. Copyright 2016 AIP Publishing LLC.

Temperature measurements can also provide estimates of voltage dependent heat dissipation capacity. The transient heat flux at the surface can be calculated analytically. Details of the derivation are provided in Appendix C.

$$q''_{(@\,r=r_0)} = -k\frac{\partial T}{\partial r}_{(@\,r=r_0)} = \frac{(T_0 - T_\infty)}{\xi_1 r_0}(\xi_1 \, cos(\xi_1) - sin(\xi_1)), \tag{4}$$

where k is thermal conductivity and T_0 is measured temperature at center. The present results can be generalized if the applied voltage is expressed in dimensionless terms. The electrowetting number η represents the ratio of the electrostatic energy stored in the vapor layer to the liquid-vapor interfacial tension, and is commonly used to non-dimensionalize EW voltages as:

$$\eta = \frac{\varepsilon_0 \varepsilon_v V^2}{2d\sigma_{lv}}, \tag{5.5}$$

where ε_0 is permittivity of vacuum, ε_v is dielectric constant of vapor, V is applied voltage, d is the initial vapor layer thickness and σ_{lv} is liquid-vapor interfacial tension. The initial vapor gap thickness is the only unknown quantity in equation 5.5. It can be calculated from energy balance considerations which dictate that the change in sphere temperature is a result of heat transfer to the liquid by conduction and radiation across the vapor layer. The underlying energy balance is:

$$-kA\frac{\partial T_s}{\partial r} = \frac{T_s - T_{sat}}{d/Ak_v} + \frac{\sigma A\left(T_s{}^4 - T_{sat}^4\right)}{\frac{1-\varepsilon_s}{\varepsilon_s} + \frac{1}{F_{sl}} + \frac{1-\varepsilon_{liquid}}{\varepsilon_{liquid}}}, \tag{5.6}$$

where m is sphere mass, A is surface area, k_v is vapor thermal conductivity, σ is Boltzmann constant, ε_s is emissivity of sphere, ε_{liquid} is emissivity of liquid and $F_{sl} = 1$ is the view factor - fraction of the liquid area seen by surface (Bergman et al., 2011).

Figure 5.6 shows a section of the boiling curve (Dhir, 1998), which is the heat flux (equation 5.4) as a function of the superheat (surface temperature – saturation temperature). It is seen that the boiling curve progressively shifts up at higher EW numbers. Heat dissipation saturates at higher voltages as significant fractions of the surface are liquid-wetted. It is seen that EW voltages can enhance the heat dissipation by upto 5X, even at lower superheats. It should be pointed out that Figure 5.6 is based on transient heat transfer measurements and is only a first order estimate of heat dissipation. Nevertheless, Figure 5.6 does quantify the enormous potential of electric fields to enhance and tune boiling heat transfer. It is also pointed out that electric fields influence heat transfers in the nucleate boiling regime. Nucleate boiling depends on bubble-related phenomena like nucleation, growth and detachment. Concentrated electric fields will influence such interfacial phenomena and thus affect thermal transport. Such bubble-related effects would have influenced the nucleate boiling region of present results. However, an analysis of the role of electric fields on nucleate boiling is beyond the scope of the present work, which is focused on a study of film boiling.

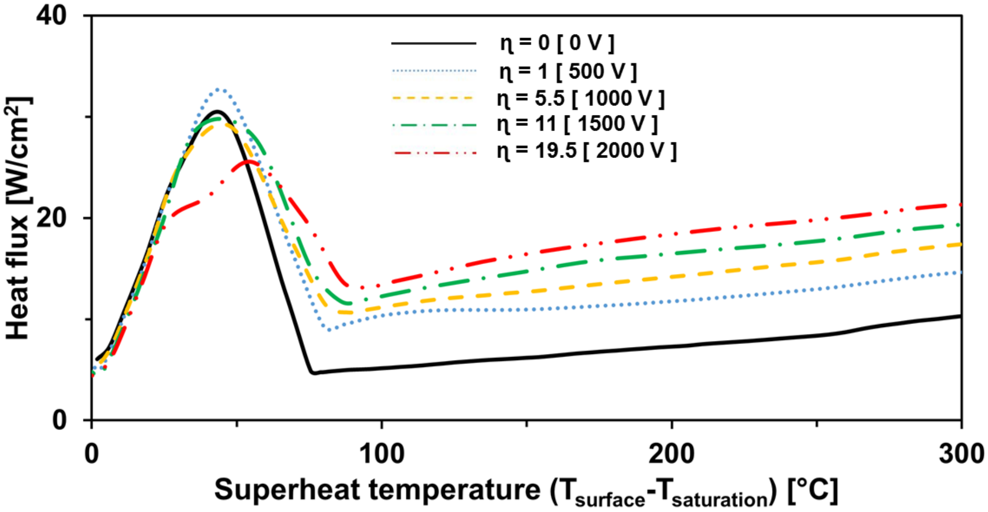

Figure 5.6. Heat dissipation capacity versus superheat for various electrowetting numbers. The boiling curve progressively shifts higher with increasing electric fields. Figure 5.6 reprinted with permission from Shahriari et al. Copyright 2016 AIP Publishing LLC.

It is noted that the concept of film boiling suppression is based on electrostatic attraction, and does not require current flow through the liquid. The current measured during these experiments was very low (< 1mA); the resulting Joule heating is much less than the heat dissipation. It is useful to define a coefficient of performance (COP) as the ratio of the heat transfer enhancement to the electrical power consumption. The measured COP's for the 500, 1000, 1500 and 2000 Volts quenching experiments were 250, 250, 180 and 170, respectively; this highlights the low power nature of this concept.

5.3. CONCLUSIONS

In conclusion, this study demonstrates electrically tunable quenching and analyses the fundamental mechanisms which enhance heat transfer. It is seen that electric fields enhance cooling by up to an order of magnitude and fundamentally alter the classical cooling curve. This study lays the foundation for a tool to control properties of metals by tuning the metallurgy (grain size, composition and orientation) via electrically tunable cooling. It can expand the selection basket of working fluids by enhancing heat transfer associated with fluids which traditionally do not have good heat transfer characteristics. Ultrafast cooling, dryout prevention and vapor instability control are other applications that can directly benefit from the use of electric fields to eliminate the Leidenfrost effect and suppress film boiling.

Chapter 6: Acoustic detection of electrostatic suppression of the Leidenfrost state [7]

This chapter describes acoustic detection of electrostatic suppression of the Leidenfrost state. It is seen that the liquid-vapor instabilities that characterize suppression on solid surfaces can be detected acoustically. Acoustic signal tracking enables objective measurements of the threshold voltage and frequency required for suppressing the Leidenfrost state. It also offers additional physical insights that would not have been possible with visual measurements. For instance, on liquid surfaces, the absence of an acoustic signal indicates a different suppression mechanism (instead of instabilities). Along with droplet-based experiments, this chapter also describes using acoustics to detect boiling patterns associated with electrostatically-assisted quenching. Overall, this work highlights the benefits of acoustics as a tool to better understand electrostatic suppression of the Leidenfrost state, and the resulting heat transfer enhancement.

6.1. EXPERIMENTAL METHODS

Figure 6.1 shows a schematic of the experimental apparatus. Leidenfrost state suppression was studied on solid (aluminum wafer) and liquid (silicone oil pool) surfaces, on a hot plate. Surface temperature was measured with a thermocouple and an infrared camera. Droplets (isopropanol, acetone and methanol) were micropipetted on the surface (above Leidenfrost temperature) while in contact with a 100 μm diameter aluminum wire. This wire restricts droplet mobility and electrically biases the droplet; the substrate is electrically grounded. Suppression was visualized with a high-speed camera, as in previous

---

[7] Acoustic detection of electrostatic suppression of the Leidenfrost state was conducted in collaboration with Prof. Preston Wilson.

studies (Shahriari et al., 2014; Ozkan et al., 2017). All experiments were repeated and the reported results are the average of at least four measurements.

The acoustic signature of the droplet was recorded (24-bit samples at 96 kHz) by a microphone (Earthworks M23), located 10 cm away from the droplet; the microphone was connected to a recorder (Roland R-26). All experiments were conducted in an anechoic chamber, which minimized reflections (down to 250 Hz) and provided a low ambient noise environment. Acoustic signals were analyzed using the software Raven (Cornell University). A high pass filter (>300 Hz) was applied to all measurements to eliminate low frequency noise from the experimental apparatus that was below the frequency range of interest.

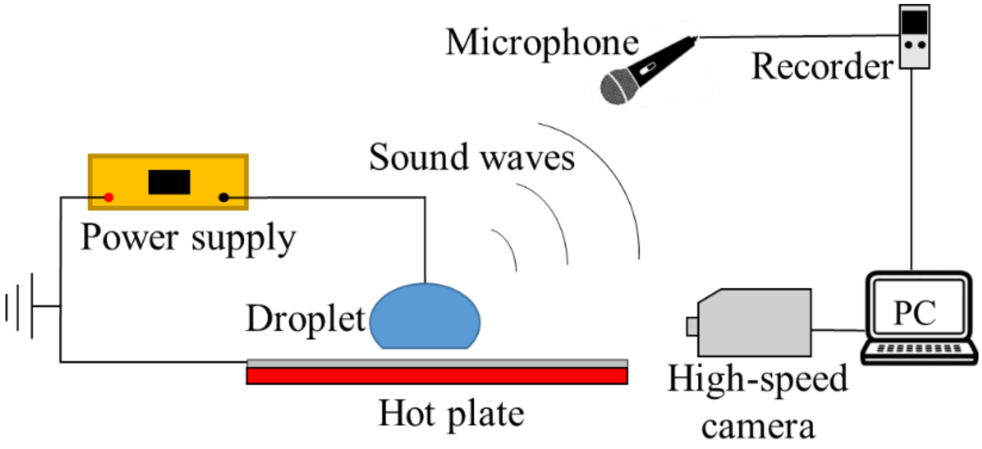

Figure 6.1. Experimental apparatus for acoustic detection of electrostatic suppression of the Leidenfrost state.

Figure 6.2 illustrates the results and analysis methodology employed in this study. It shows the microphone signal (which is proportional to acoustic pressure) and the spectrogram (power spectrum plot of the frequency components of the sound signal versus time) associated with electrostatic suppression of the Leidenfrost state of a 30 μL isopropanol droplet on a 540 °C aluminum surface. In the absence of a voltage (left part of Figure 6.2), the Leidenfrost state is confirmed by the relatively low pressures of the acoustic signal (between zero and 1.5 seconds). Applying 300V (greater than threshold voltage) results in a sudden increase in the acoustic pressure, as liquid wets the surface and the Leidenfrost state is suppressed. Early stage suppression (between 1.5 and 2.5 seconds) has a higher acoustic pressure, which decreases as the droplet evaporates. After the droplet completely evaporates (4.75 seconds), the acoustic pressure returns to the original state.

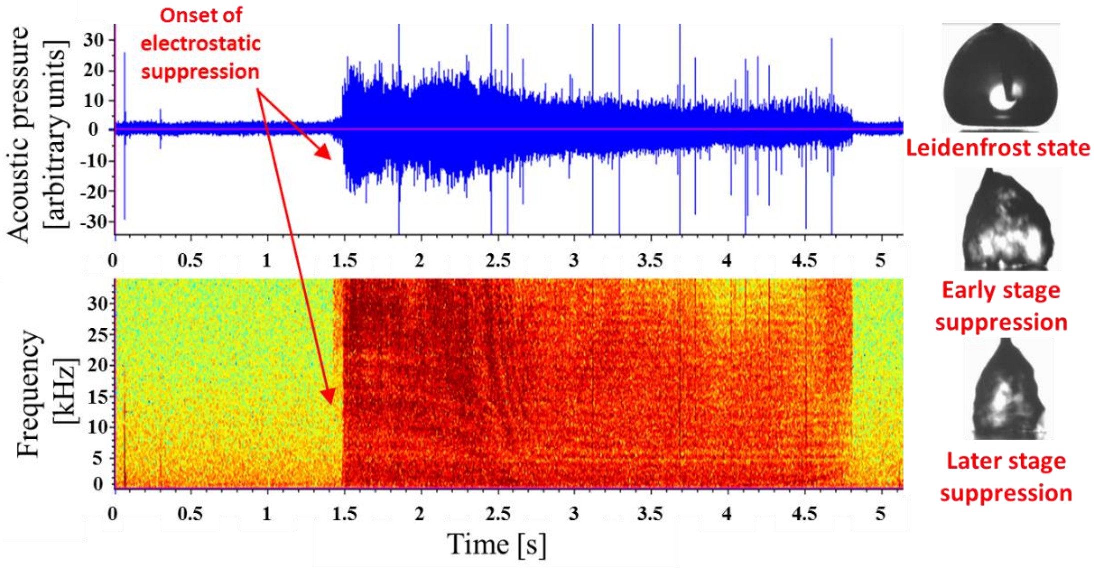

Fig. 2. Acoustic pressure and spectrogram associated with electrostatic suppression of the Leidenfrost state.

Experiments were conducted to estimate the threshold DC voltage for suppression while recording the acoustic output of the process. The microphone signal was converted to an acoustic pressure signal using a standard microphone calibrator. The RMS acoustic pressure was then calculated for the time period corresponding to suppression (*e.g.* between 1.5 s and 4.75 s in Figure 6.2).

6.2 RESULTS

Figure 6.3 shows the RMS acoustic pressure versus applied voltage for 30 μL isopropanol droplets on an aluminum substrate at 300 °C and 540 °C. The inset of Figure 6.3 shows a threshold voltage of 60 V (estimated as the voltage beyond which the slope of the curve changes by 10X). In chapter 2 of this dissertation, the threshold voltage was estimated by visual observation of instabilities at the liquid-vapor interface, which cause liquid fingers to bridge the vapor gap. However, visual detection is subjective and depends on the quality and magnification of imaging. In this study, such instabilities are detected visually only at 75V. The difference between the two methods is significant; these results suggest that visual measurements would over-predict the threshold voltage by 25%. It is noted that the reported RMS acoustic pressures were obtained by averaging from the onset of suppression till complete droplet evaporation. Also, the RMS acoustic pressure below threshold voltage was not zero; the ambient noise floor was 0.5 mPa.

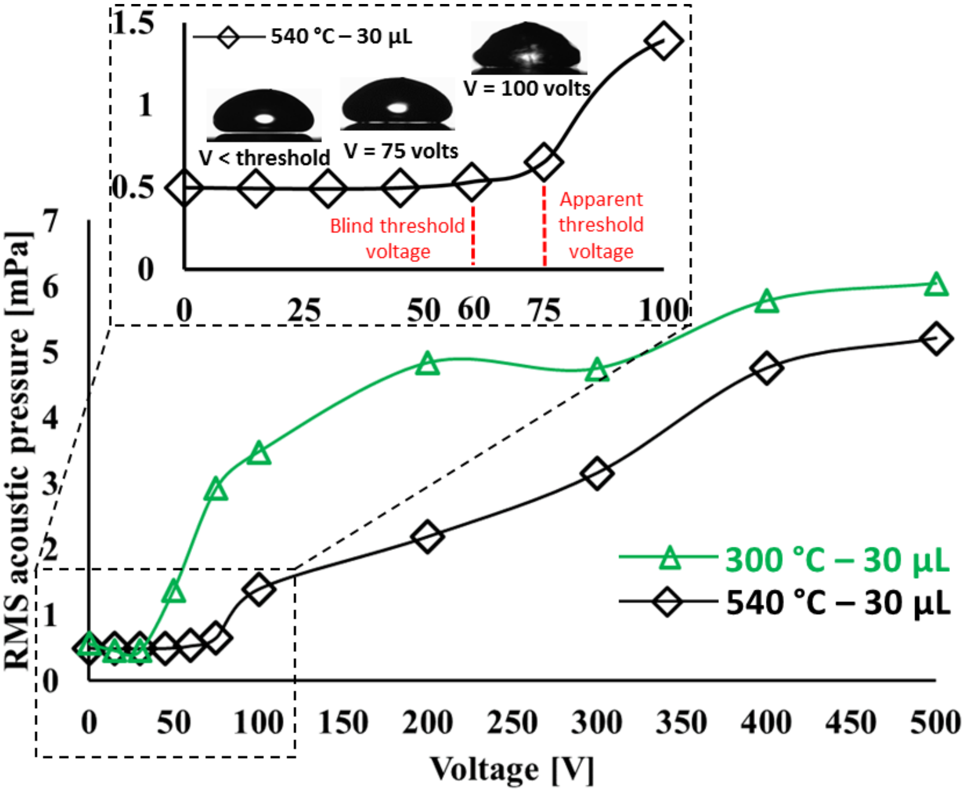

Figure 6.3. RMS acoustic pressure versus applied voltage during Leidenfrost state suppression on an aluminum surface. The inset shows the threshold voltage required to initiate suppression on a 540 °C surface.

Figure 6.3 also shows that the RMS acoustic pressure steadily increases after the Leidenfrost state is suppressed, due to more intimate solid-liquid contact. Surface temperature influences the threshold voltage and acoustic pressures, as seen in experiments at 300 °C and 540 °C. At below-threshold voltages, the two curves overlap, due to the absence of any solid-liquid contact. Using this acoustic technique, the threshold voltage is measured to be 40V and 60V at 300 °C and 540 °C, respectively. This is expected, since a lower temperature reduces vapor pressure build-up beneath the droplet, which needs to be overcome by the electrostatic force. RMS acoustic pressure will increase in the post threshold voltage regime; however, the lower temperature surface offers less resistance to wetting, leading to more frequent instances of wetting, which elevate RMS acoustic pressures. Such distinctions are difficult to obtain from visual measurements and highlight the utility of this technique. These findings also suggest that with careful calibration, this technique can be used to estimate surface temperature.

Acoustic detection of electrostatic suppression using AC fields, was studied next. In a recent study (Ozkan et al., 2017), it was shown that the frequency of the AC waveform significantly determines the extent of suppression. At low frequencies (compared to the inverse of charge relaxation time), the applied electric field concentrates in the vapor gap (droplet is electrically conducting and equipotential), which maximizes the electrowetting force. As the frequency is increased, the electric field penetrates into the droplet, which reduces its strength, and therefore the extent of suppression. The threshold frequency is defined as the minimum frequency required to completely eliminate electrostatic suppression. Beyond the threshold frequency, the electric field exists in the entire droplet (which behaves as an insulator); this effectively stops suppression. The frequency of an AC waveform can thus counter the applied voltage.

The results of threshold frequency measurements for isopropanol droplets are shown in Figure 6.4 for 100 V AC and frequencies in the range 10-45 kHz. It is seen that RMS acoustic pressures decrease with increasing frequency. The threshold frequency corresponds to the plateauing of this curve and is measured to be 42.5 kHz. This is confirmed by visual absence of liquid fingering. These results again highlight the utility of acoustic techniques for objective characterization of suppression. It is noted that the ambient noise floor for AC experiments (0.9 mPa) is larger than DC experiments (0.5 mPa); this can be attributed to the acoustic noise produced by the AC function generator being louder than the DC equipment.

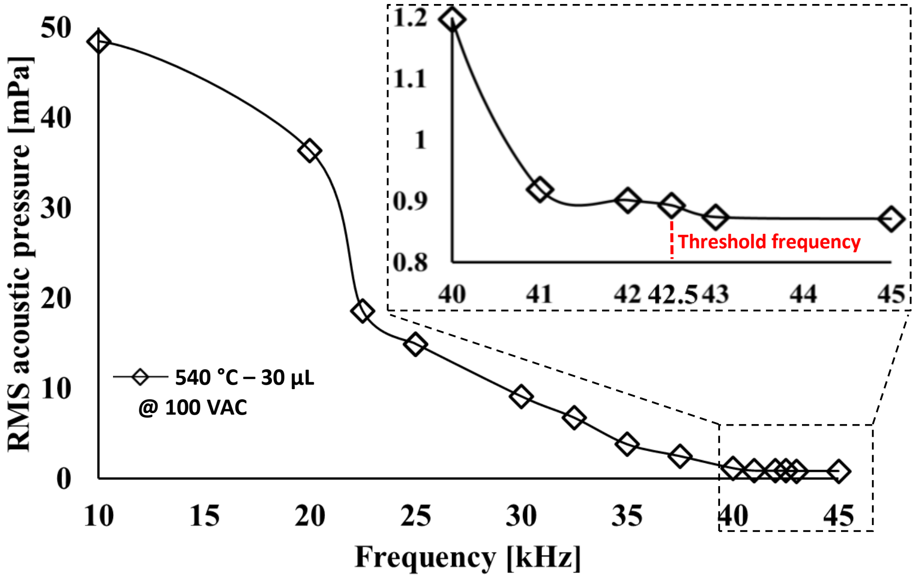

Figure 6.4. AC frequency-dependent RMS acoustic pressure associated with AC electric field-induced Leidenfrost state suppression. Inset shows a zoomed-in view of data between 40-45 kHz.

Insights obtained from acoustic measurements of Leidenfrost state suppression on liquid substrates are described next. In a recent study (Shahriari et al., 2017b), we highlighted several interesting aspects of suppression on heated silicone oil surfaces. Firstly, the Leidenfrost droplet deforms the substrate, (Figure 6.5a). Secondly, the electric field is distributed in the vapor gap and the silicone oil substrate. This fundamental difference in the electric field distribution (compared to conducting substrates) implies that the droplet sees a downward electrostatic force even after completely penetrating the substrate liquid. Indeed, the droplet completely sinks into the silicone oil substrate (Figure 6.5a). Interestingly, the threshold voltages are significantly lower (Shahriari et al., 2017b) on silicone oil, and range from 10-25 V, depending on the thickness of the silicone oil pool. The voltage difference across the vapor gap is even lower, since a majority of the applied voltage is expressed across the silicone oil layer. These differences suggest that a different mechanism is responsible for suppression, instead of interfacial instabilities, which explain suppression on solid surfaces. Also, direct visualization of instabilities in the vapor gap is not possible, due to the deformation of the substrate.

Acoustic signature tracking conveniently overcomes this limitation. Figure 6.5b shows the RMS acoustic pressure versus voltage for 10 µL isopropanol droplets on silicone oil at 150 °C. No acoustic signal is detected despite suppression, which is easily confirmed visually. This clearly suggests that sound-producing instabilities and fingering events do not occur. Understanding the specific mechanism underlying suppression is beyond the scope of this study. These experiments again show the value of acoustic detection, as the absence of instabilities would have been challenging to detect using other techniques.

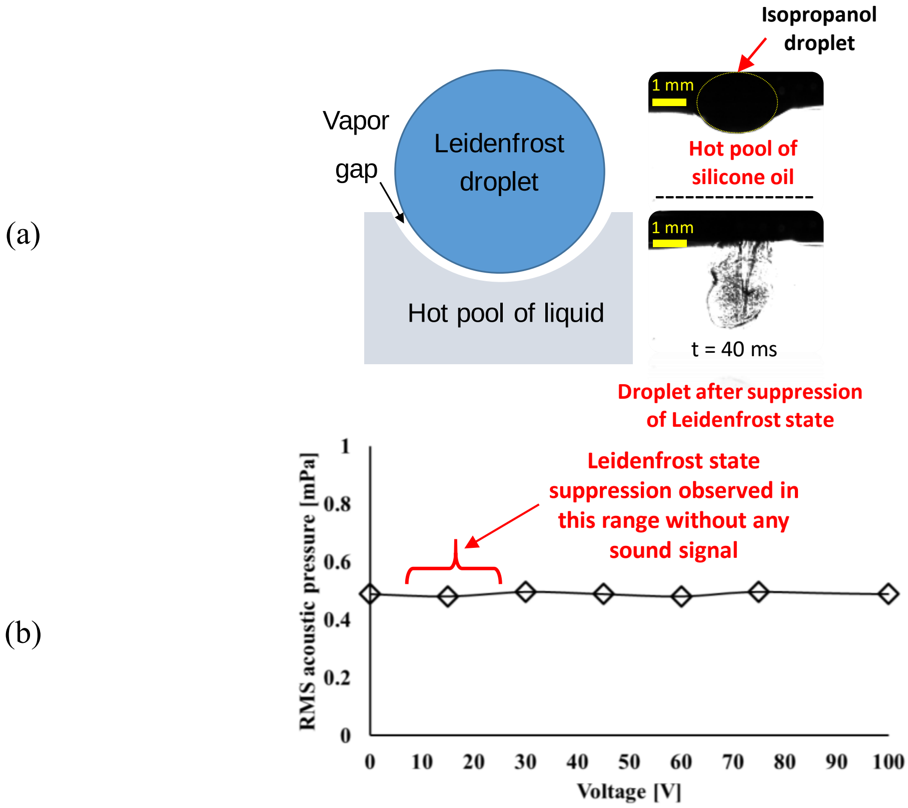

Figure 6.5. (a) Electrostatic suppression on a deformable liquid substrate and (b) RMS acoustic pressure versus voltage. Figure 6.5a reprinted with permission from Shahriari et al. Copyright 2017 American Chemical Society.

The present measurements can not only pinpoint the threshold voltage, but also yield more accurate estimates of heat transfer benefits of suppression. To first order, the heat dissipation capacity can be estimated by measuring the droplet evaporation rate (image processing). The heat dissipation capacity can be predicted using $q''=(m.hfg)/(A.tb)$, where m is droplet mass, hfg is latent heat of vaporization, tb is the droplet lifetime and A is the solid-liquid contact area. The previous estimate described in chapter 2 was based on the footprint area of the droplet on the surface; however, this is inaccurate since the droplet does not wet 100% of the footprint area. The actual liquid-solid contact area can be estimated by linearly scaling the area in proportion to the measured RMS acoustic pressure at a particular voltage. This hypothesis assumes that the number of solid-liquid contact events influence the contact area and the generated acoustic pressure in the same manner. Acoustic measurements also enable more accurate measurements of the droplet lifetime.

Figure 6.6 compares the presently-estimated heat dissipation capacity with previous estimates (Shahriari et al., 2014). It is seen that the heat dissipation capacity, when factoring in the actual solid-liquid contact area, is significantly higher than the apparent heat dissipation capacity. The actual heat dissipation capacity is up to 270% higher than previously estimated. This dissertation reports heat flux dissipation exceeding 400 W/cm^2 for evaporating droplets. This exercise again highlights the utility of acoustics as a tool for better understanding the thermo-fluidics of the Leidenfrost state.

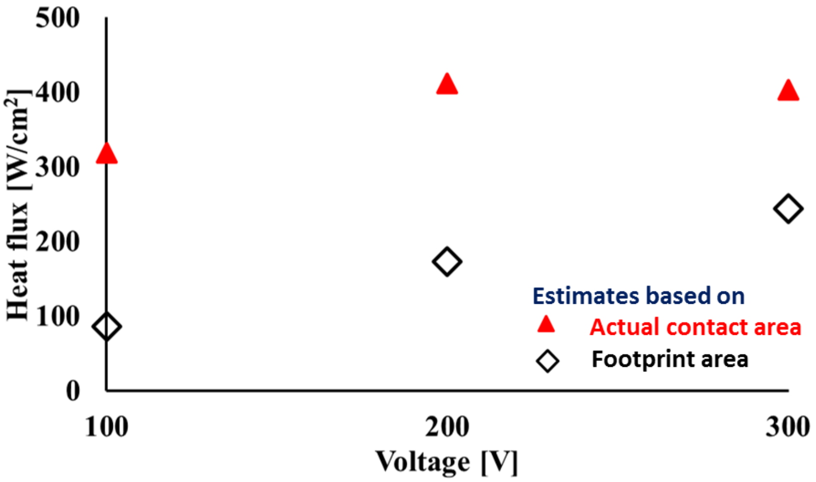

Figure 6.6. Estimated heat dissipation capacity associated with droplets where the Leidenfrost state is electrostatically suppressed.

The final set of experiments were about electrostatically-assisted quenching of metals. At very high temperatures, typical of quenching, a vapor film forms on the surface. This film can be electrostatically suppressed (Shahriari et al., 2016a), which significantly accelerates the cooling rate. In the experiments described in this chapter, heated 2.54-cm-diameter copper spheres were immersed in an isopropanol bath. The sphere had an ungrounded K-type thermocouple at the center. A wire biased the sphere and a potential difference across the vapor gap was established by a grounded electrode in the bath. The apparatus and procedure previously described was employed again, but the microphone was replaced with a hydrophone (Teledyne Reson TC4013) submerged in the liquid bath, 5 cm away from the sphere. The acoustic signature of the quenching process was recorded and hydrophone signals were converted into acoustic pressure signatures using factory calibration.

Images of the sphere in Figure 6.7 show various boiling stages during cooldown. Film boiling is immediately suppressed by the applied electric field; the resulting pattern can be termed as transition boiling, with any point on the surface alternating contacting vapor and liquid. At lower temperatures, the pattern changes to nucleate boiling (characterized by discrete bubbles), followed by natural convection. Figure 6.7 also shows the temperature-time curve and the RMS acoustic pressure-time curve in the absence and presence of an electric field. The fundamental switch from film boiling (no voltage) to transition boiling (applied voltage) in the initial phase drastically alters the cooling curve.

The RMS acoustic pressure curve in Figure 6.7 yields several important insights. Firstly, acoustic measurements clearly detect transitions to nucleate boiling (from film and transition boiling). Prior to these transitions, RMS acoustic pressures are larger for the electrowetted case (~ 3.2 Pa) compared to the non-electrowetted case (~ 2.6 Pa). Secondly, when the temperatures reach ~ 150 °C, the switch to nucleate boiling and resulting collapse of the vapor gap generates much higher acoustic pressures. The peak RMS acoustic pressure for the electrowetted case (66 Pa) is smaller than the non-electrowetted case (86 Pa), likely due to the smaller vapor gap resulting from the applied voltage. In the nucleate boiling region, the RMS acoustic pressures are 5.3 Pa and 4.1 Pa for the non-electrowetted and electrowetted cases, respectively. These amplitudes depend on various bubble-related phenomena, which also depend on the electric field. Finally, the acoustic signature of the natural convection region is almost identical for the two cases. This is expected since the influence of the electric field is no longer at play (due to the absence of the vapor gap). Together, all these results highlight the wealth of information that can be inferred from acoustic signature tracking of electrostatically-assisted quenching.

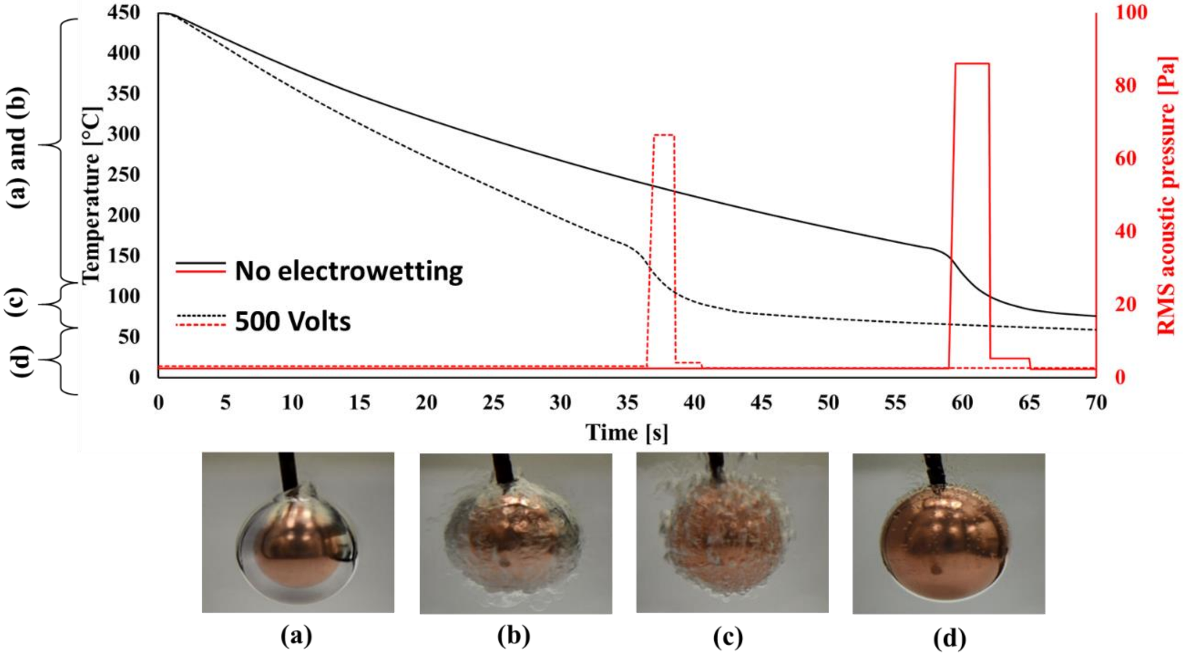

Fig. 7. Acoustic signature tracking of electrostatically-assisted quenching. Temperature and RMS acoustic pressure variation is shown along with various boiling patterns observed during cooldown: (a) Film boiling, (b) Transition boiling, (c) Nucleate boiling and (d) Natural convection.

6.3 CONCLUSIONS

In conclusion, acoustics is demonstrated as a powerful tool to analyze electrically enhanced boiling in droplet and pool boiling configurations. Threshold voltage/frequency and the transition between various boiling regimes can be objectively determined by tracking the acoustic signature. With appropriate calibration, this technique can also be used to estimate surface temperatures, heat flux and onset of dryout associated with electrically enhanced boiling.

Chapter 7: Conclusions and suggestions for future work

This chapter summarizes the key findings emerging from this dissertation and outlines future research directions in the field of boiling heat transfer enhancement.

7.1. MAJOR SCIENTIFIC FINDINGS AND CONTRIBUTIONS OF THIS DISSERTATION

This dissertation has resulted in valuable scientific contributions to the field of phase change heat transfer, and more specifically, to the field of boiling heat transfer enhancement. Overall, this work resulted in significant creation of fundamental knowledge, and the development of a new area of study in the field of boiling heat transfer. Utilization of electric fields can control and enhance film boiling heat transfer, and fundamentally change the shape of the boiling curve. This work has enabled a fundamental understanding of the influence of electric fields on the micro/mesoscale fluid-surface interactions in the film boiling regime. This research has been highly multidisciplinary in nature involving fluid mechanics, heat transfer, electrostatics and materials. Specific outcomes include measurements of electrically enhanced heat transfer, and an in depth understanding of the coupled thermal-fluid-electrical phenomena influencing film boiling heat transfer. Major scientific advancements emerging from this work are summarized below as:

7.1.1. Experimental study of electrostatic suppression of the Leidenfrost state

It was demonstrated that electrostatic liquid attraction can suppress film boiling and prevent surface dryout. The major scientific findings/contributions of this study include:

- Electrostatic suppression of the Leidenfrost state is successful even at ultrahigh temperatures, exceeding 500 °C.

- Elimination of the vapor layer increases heat dissipation capacity by more than 10X.
- Heat removal capacities exceeding 500 W/cm^2 are measured, which is five times the critical heat flux (CHF) of water on common engineering surfaces.
- Electrostatic suppression of film boiling can make the traditional CHF limit irrelevant, and enable electrically tunable boiling heat transfer enhancement.
- Leidenfrost state suppression can be achieved using both DC and AC electric fields.
- Higher voltages result in shorter droplet lifetimes and higher heat dissipation capacities.
- Higher frequencies reduce the strength of the electric field and extent of electrostatic suppression.

7.1.2. Analysis of Leidenfrost state suppression

Linear stability theory was employed to understand the instabilities at the threshold voltage for Leidenfrost state suppression. The major scientific findings/contributions of this study include:

- The interplay of the destabilizing electrostatic force and stabilizing capillary force and evaporation determines the minimum voltage requirements (threshold voltage) to suppress the Leidenfrost state.
- Linear stability theory accurately predicts threshold voltages for different size droplets and varying temperatures.

7.1.3. Leidenfrost state suppression on soft surfaces

Electrostatic suppression of the Leidenfrost state on soft surfaces was analyzed. The major scientific findings/contributions of this study include:

- The nature of suppression is strongly dependent on the electrical properties and deformability of the substrate.

- For non-conductive, deformable substrates, the Leidenfrost droplet can completely penetrate inside the substrate and lose its ‘droplet-like’ shape.
- For electrically conducting and low deformability liquid substrates, the nature of electrostatic suppression is similar to that on solid metal substrates.
- The voltage requirement for suppressing the Leidenfrost state is significantly lower for deformable liquid substrates.
- Thermally driven Marangoni flows enhance the drainage in the vapor layer, and significantly reduce the vapor layer thickness.

7.1.4. Experimental study of Leidenfrost state suppression during quenching

Electrically tunable quenching was demonstrated and analyzed. The major scientific findings/contributions of this study include:

- The change in the boiling patterns also alters the heat transfer rates.
- Electric fields enhance cooling by up to an order of magnitude and fundamentally alter the classical cooling curve.

7.1.5. Acoustic detection of electrostatic suppression of the Leidenfrost state

It was demonstrated that acoustic signal tracking enables objective measurements of the threshold voltage and frequency required for suppressing the Leidenfrost state. The major scientific findings/contributions of this study include:

- Visual detection of electrostatic suppression is subjective and depends on the quality and magnification of imaging.
- Acoustic emissions provide a more accurate measurement of threshold voltage and frequency requirements for Leidenfrost state suppression.

- With appropriate calibration, this technique can be used to estimate wetted area, surface temperatures, heat flux and onset of dryout associated with electrically enhanced boiling.

7.2. RECOMMENDATIONS FOR FUTURE WORK

The results of the present studies lay the foundation for future research on the topic of boiling heat transfer enhancement using electric fields. Three potential lines of inquiry are described ahead.

7.2.1. Nucleate boiling: Study of bubble growth under electric fields

Bubble growth is an important microfluidic phenomena influencing nucleate and transition boiling heat transfer. While bubble nucleation is primarily influenced by the nature and density of nucleation sites, bubble growth depends on the forces acting on the already nucleated bubble. The addition of an electric field affects the force distribution around the bubble and will influence bubble growth. Figure 7.1 depicts the electric field distribution around a growing bubble subjected to an electric field. It should be noted that there is no electric field within the fluid (the liquid stays equipotential since it is electrically conducting). However, there is a finite electric field inside the bubble which will influence further growth. It should be noted that the strength of the field will depend on the bubble shape and that the field will modify the bubble shape. As a first order estimate, it can be hypothesized that the electric field will flatten the bubble, thereby reducing the thermal resistance to heat transfer in the nucleate boiling regime.

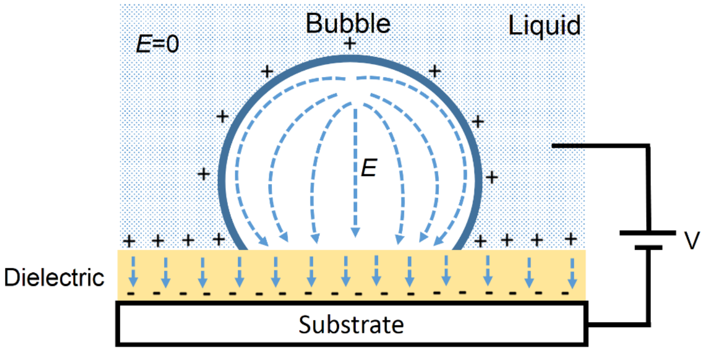

Figure 7.1. Electric field lines in a bubble under an applied voltage.

Future work can include modeling bubble growth equations with additional electrostatic force terms. The model can be validated by measuring bubble growth rates using high speed photography. Since nucleation is a stochastic process, multiple bubbles will be imaged.

7.2.2. Nucleate boiling: Electrical control of near-bubble convection and bubble detachment

The high heat transfer coefficients in nucleate boiling have been attributed to multiple effects. One of the enhancement mechanisms is near-bubble convection and the agitation and mixing provided by the departing bubbles. Electrowetting is a powerful tool to control near-bubble convection and mixing by controlling the kinetics of the 3 phase line (Figure 7.2a). Electrowetting can also control bubble detachment (Figure 7.2b) and promote rapid rewetting, thereby driving up heat transfer coefficients. It should be noted that bubble detachment also depends on other forces acting on the droplet including, buoyancy, surface tension, viscous forces and surface forces like contact line friction and hysteresis (which affect the motion of the 3 phase line).

Two methods of controlling near-bubble convection and bubble detachment are suggested. The first method relies on using a pulsed DC electric voltage instead of a continuous DC voltage. This time varying wettability will cause periodic oscillations of the contact line and provide additional energy to overcome the barrier to bubble detachment. The optimum pulsing frequency will be decided based on experimental measurements of boiling heat transfer coefficients.

A second method of controlling near-bubble convection and bubble detachment relies on the use of AC voltages instead of DC voltages. One key benefit of AC electrowetting is the reduction in contact line friction (Kumari et al., 2008) opposing fluid motion, and subsequent detachment. Replacing DC voltages with low frequency AC voltages is expected to favorably influence bubble detachment. Another benefit of AC electrowetting results from the oscillatory motion (Oh et al., 2008) of the contact line in response to a sinusoidal waveform. The resulting agitation and mixing is expected to enhance boiling heat transfer coefficients.

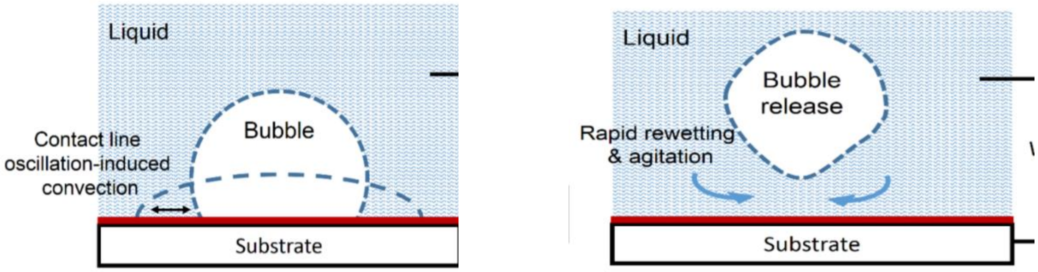

(a) (b)

Figure 7.2. Suggested mechanisms to (a) increase near-bubble convection and (b) influence bubble detachment.

Visualization experiments will be conducted to measure bubble detachment rates under pulsed DC as well as AC electrowetting conditions. Experiments will be conducted on smooth hydrophilic as well as smooth hydrophobic surfaces since surface parameters like contact line friction are very strong functions of the surface chemistry. Stochastically averaged data will be used to validate the bubble departure models.

7.2.3. Quenching of metals: Ultrafast cooling of metals by electric field-assisted pool boiling

A study of the influence of electric field-assisted quenching on mechanical properties of metals is an important suggestion for future work. Quenching experiments involve immersing hot bodies of metal in a liquid pool and applying an electric field across the vapor gap. The effect of AC frequency on the cooling rate of quenched objects will be investigated. Metal objects (cylinders or spheres) will be quenched in a pool of water or isopropanol and their center and surface temperatures will be recorded under different electrowetting voltages. This task will enable an understanding of the role of the applied voltage and AC frequency on the cooling rate during quenching. Specifically, the switch from ‘film-to-transition’ boiling, ‘transition-to-nucleate’ boiling, and ‘nucleate boiling to free convection’ will be analyzed under different voltages and frequencies.

Electric field-dependent cooling rates can also enable control of the metallurgy resulting from heat treatment of steels. The metallurgy and the resulting mechanical properties depend greatly on martensite formation in plain carbon steels. The martensite transformation in high alloy steels requires lower cooling rates as compared to low plain carbon steels, so it is not very challenging in terms of heat transfer. On the other hand, the martensite transformation window for low carbon plain steels is narrow, which necessitates ultra-fast cooling for a high percent martensite transformation. Quenching in a salt-water solution can increase the cooling rate, but it results in non-uniform cooling, increased distortion, cracking and soft spot formation. Flow boiling can provide high heat fluxes, but is still limited by CHF considerations. Flow boiling heat transfer can potentially be enhanced using electric fields. Ultra-high cooling rates resulting from electrowetting-assisted flow boiling can enable martensite transformation in low plain carbon steels. Including the electric field to enhance the heat flux can also increase the CHF. High heat removal rates during quenching can increase the hardness and tensile strength of steels after quenching significantly.

The hypothesis on the influence of electric fields on martensitic transformations and the resulting hardness is described here. Figure 7.3 shows the hardness of plain carbon steels versus carbon content, for various fractions of martensite content. The hardness of steel increases with the carbon content as well as with increasing martensitic fractions. However, the heat transfer challenge is the reduction in the martensite transformation window, as impurities in steel decrease.

A low cooling rate provided by natural convection in oil is sufficient for martensite transformation in high alloy steels. On the other hand, ultrafast cooling is necessary as the concentration of other elements in iron becomes smaller. For this reason, the cooling rate without electrostatic suppression could be enough for martensite transformation in high carbon steels (green curve in Figure 7.3). As the carbon content decreases, the martensite transformation window becomes smaller and the cooling rate for martensite transformation would not be adequate without enhancement. The red curve in Figure 7.3 shows the expected hardness of the quenched steel. It is expected that for moderate carbon content, there will be a higher percent of martensite transformation (and higher hardness) with electric fields. At very low carbon content, the martensite transformation window could be so small that even the electrically enhanced forced convection boiling may not be enough for a high percentage martensite structure after quenching. On the other side of the curve, the cooling rate without electric fields could be sufficient to result in high fraction martensite structures for a high carbon steel (or high alloy steel). Under such conditions electrical enhancement will likely not make much difference (right hand side of the graph). All such hypotheses could be validated with experiments.

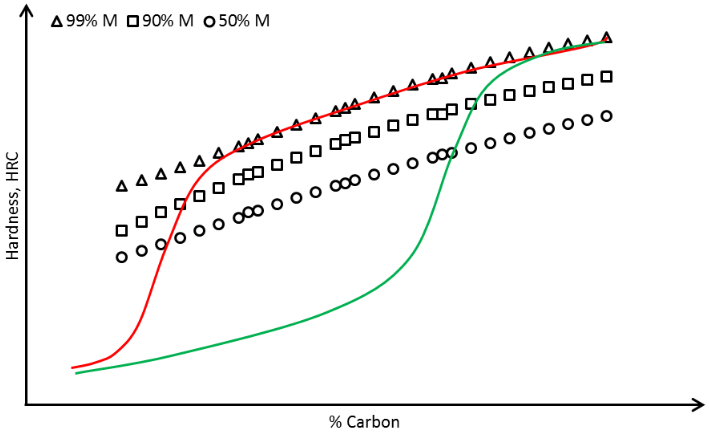

Figure 7.3. Hardness of steel versus carbon concentration for varying martensite compositions. Red curve represents the expected hardness of different plain carbon steels (10xx) after electric field-assisted quenching. Green curve represents the expected hardness after quenching without electric fields. The red and green curves are based on the hypothesis described in this section.

Appendix A: Derivation of the analytical model to predict the vapor layer thickness on solid surfaces

Appendix A describes derivation of equations for the forces acting on the droplet at Leidenfrost state, in order to conduct a 1D force balance to model the Leidenfrost phenomenon.

A.1. Upward vapor pressure force derivation

There are three forces acting on a hovering drop on a hot surface. These forces include gravity, buoyancy and vapor pressure force. As per the experimental observations, it is assumed that Leidenfrost droplet has a flattened bottom surface as shown in Figure A.1.

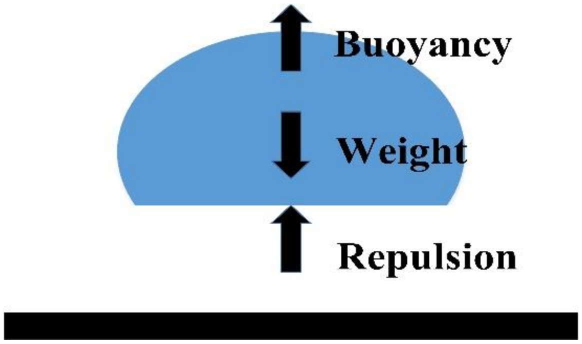

Figure A.1. One dimensional force balance on a Leidenfrost droplet.

- **Gravitational force:** Droplet weight acts downward and is calculated as:

$$F_{Weight} = \rho_{water} g \forall_{water} \tag{A.1}$$

- **Buoyancy force:** Buoyancy acts upwards and is calculated as:

$$F_{Buoyancy} = \rho_{air} g \forall_{water} \tag{A.2}$$

- **Upward force due to vapor evaporation:** Figure A.2 shows a schematic of Poiseuille vapor flow under a drop with a flattened base.

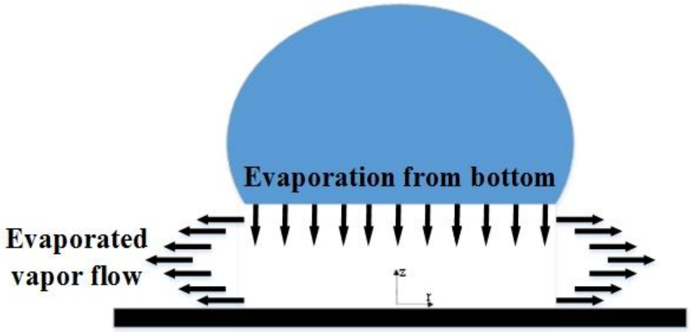

Figure A.2. Schematic model of vapor flow.

In order to proceed with force calculations, the following simplifying assumptions are considered:

- Uniform vaporization from the droplet base.
- Continuous water feed from top.
- Classical lubrication theory can be applied. Since $L_v << R_{drop}$, $\overline{u_{vap}} << u_{radial}$ and $\partial P / \partial r$ is independent of vertical position z.
- Steady state, laminar and axisymmetric flow, $u_r = u_r(r, z)$.
- Creeping flow (to neglect inertial terms in Navier-Stokes equations)

Derivation starts with solving Navier-Stokes equations for the Poiseuille vapor flow in the gap between water drop and surface.

- **Continuity equation:**

$$\cancel{\frac{\partial\rho}{\partial t}}+\frac{1}{r}\frac{\partial}{\partial r}(\rho r u_r)+\cancel{\frac{1}{r}\frac{\partial}{\partial\theta}(\rho u_\theta)}+\cancel{\frac{\partial}{\partial z}(\rho u_z)}=0 \tag{A.3a}$$

$$\frac{1}{r}\frac{\partial}{\partial r}(r u_r)=0\Rightarrow\boxed{r u_r=\Phi(z)} \tag{A.3b}$$

- **r-momentum equation:**

$$\begin{aligned}\rho\left(\cancel{\frac{\partial u_r}{\partial t}}+u_r\frac{\partial u_r}{\partial r}+\cancel{\frac{u_\theta}{r}\frac{\partial u_r}{\partial\theta}}+\cancel{u_z\frac{\partial u_r}{\partial z}}-\cancel{\frac{u_\theta^2}{r}}\right)=\\-\frac{\partial P}{\partial r}+\mu\left[\frac{\partial}{\partial r}\left(\frac{1}{r}\frac{\partial}{\partial r}(r u_r)\right)+\cancel{\frac{1}{r^2}\frac{\partial^2 u_r}{\partial r^2}}+\frac{\partial^2 u_z}{\partial z^2}-\cancel{\frac{2}{r^2}\frac{\partial u_\theta}{\partial\theta}}\right]\end{aligned} \tag{A.4a}$$

$$\rho u_r\frac{\partial u_r}{\partial r}=-\frac{\partial P}{\partial r}+\mu\left[\frac{\partial}{\partial r}\left(\frac{1}{r}\frac{\partial}{\partial r}(r u_r)\right)+\frac{\partial^2 u_z}{\partial z^2}\right] \tag{A.4b}$$

Plugging results from the continuity equation to the simplified r-momentum equation will result in:

$$\rho\frac{\Phi}{r}\frac{\partial}{\partial r}\left(\frac{\Phi}{r}\right)=-\frac{\partial P}{\partial r}+\mu\left[\cancel{\frac{\partial}{\partial r}\left(\frac{1}{r}\frac{\partial}{\partial r}(\Phi)\right)}+\frac{1}{r}\frac{\partial^2\Phi}{\partial z^2}\right] \tag{A.5a}$$

$$-\rho\frac{\Phi^2}{r^3}=-\frac{\partial P}{\partial r}+\frac{\mu}{r}\frac{\partial^2\Phi}{\partial z^2} \tag{A.5b}$$

Assumption of a creeping flow will let us neglect inertial terms and provide us with the following simplified expressions:

$$0=-\frac{\partial P}{\partial r}+\frac{\mu}{r}\frac{\partial^2\Phi}{\partial z^2} \tag{A.6a}$$

$$0=-\frac{\partial P}{\partial r}+\mu\frac{\partial^2 u_r}{\partial z^2} \tag{A.6b}$$

Solving the above equation will yield the velocity distribution as:

$$0=-\frac{\partial P}{\partial r}+\frac{\mu}{r}\frac{\partial^2\Phi}{\partial z^2} \tag{A.7a}$$

$$0=-\frac{\partial P}{\partial r}+\mu\frac{\partial^2 u_r}{\partial z^2} \tag{A.7b}$$

Applying the no slip boundary conditions at the bottom of vapor layer ($z=0$) and top of the vapor layer ($z=L_v$)will lead to:

$$u_r=\frac{1}{2\mu}\left(\frac{\partial P}{\partial r}\right)z\left(z-L_v\right) \tag{A.8}$$

- **Mass balance equation:**

Applying mass conservation law to the control volume shown in Figure A.3, will result in:

$$2\pi\left(r+dr\right)\int_0^{L_v}u_r\big|_{r+dr}\,dz-2\pi r\int_0^{L_v}u_r\big|_r\,dz=\overline{u_{vap}}\left(2\pi r\right)dr \tag{A.9}$$

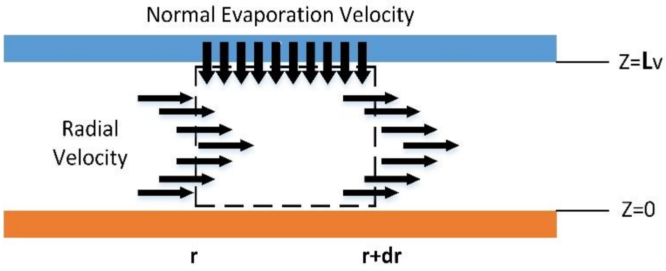

Figure A.3. Schematic for mass balance.

Inserting the radial velocity expression from equation A.8 into equation A.9 will lead to:

$$\left(r+dr\right)\int_0^H \frac{1}{2\mu}\left(\frac{\partial P}{\partial r}\right)\Bigg|_{r+dr} z\left(z-L_v\right)dz - r\int_0^H \frac{1}{2\mu}\left(\frac{\partial P}{\partial r}\right)\Bigg|_{r} z\left(z-L_v\right)dz = \overline{u_{vap}}rdr \tag{A.10a}$$

$$\left(r+dr\right)\left(\frac{1}{2\mu}\right)\left(\frac{\partial P}{\partial r}\right)\Bigg|_{r+dr}\left(-\frac{L_v{}^3}{6}\right)-\left(r\right)\left(\frac{1}{2\mu}\right)\left(\frac{\partial P}{\partial r}\right)\Bigg|_{r}\left(-\frac{L_v{}^3}{6}\right)=\overline{u_{vap}}rdr \tag{A.10b}$$

$$-\frac{L_v{}^3}{12\mu}\left[\left(r\frac{\partial P}{\partial r}\right)\Bigg|_{r+dr}-\left(r\frac{\partial P}{\partial r}\right)\Bigg|_{r}\right]=\overline{u_{vap}}rdr \tag{A.10c}$$

$$-\frac{L_v{}^3}{12\mu}\frac{1}{r}\frac{\partial}{\partial r}\left(r\frac{\partial P}{\partial r}\right)=\overline{u_{vap}} \tag{A.10d}$$

Assuming uniform vaporization from drop base ($\overline{u_{vap}} = const$) one can derive pressure distribution as follows:

$$\frac{\partial}{\partial r}\left(r\frac{\partial P}{\partial r}\right)=-\frac{12\mu\overline{u_{vap}}}{L_v{}^3}r \tag{A.11a}$$

$$r\frac{\partial P}{\partial r}=-\frac{6\mu\overline{u_{vap}}}{L_v{}^3}r^2+C_1 \tag{A.11b}$$

$$\frac{\partial P}{\partial r}=-\frac{6\mu\overline{u_{vap}}}{L_v{}^3}r+\frac{C_1}{r} \tag{A.11c}$$

$$P(r)=-\frac{3\mu\overline{u_{vap}}}{L_v{}^3}r^2+C_1\ln\left(r\right)+C_2 \tag{A.11d}$$

Applying the two boundary conditions ($P(r=0)=$ *finite* and $P(r=R_{base})=P_{atm}$) will result in:

$$P(r)-P_{atm}=\frac{3\mu R_{base}^2\overline{u_{vap}}}{L_v{}^3}\left[1-\left(\frac{r}{R_{base}}\right)^2\right] \tag{A.12}$$

Integrating the pressure distribution along the radial direction at the bottom of droplet will provide us with the upward vapor pressure force:

$$F_{up} = \int_0^{2\pi} \int_0^{R_{base}} \left(P(r) - P_{atm} \right) r dr d\theta \tag{A.13a}$$

$$F_{up} = \frac{6\pi\mu R_{base}^2 \overline{u_{vap}}}{L_v^{\ 3}} \int_0^{R_{base}} \left(1 - \left(\frac{r}{R_{base}} \right)^2 \right) r dr \tag{A.13b}$$

$$F_{up} = \frac{3\pi\mu_{vap} R_{base}^4 \overline{u_{vap}}}{2L_v^{\ 3}} \tag{A.13c}$$

A.2. Thermal transport in the Leidenfrost state

In this section, the velocity of vapor ejecting from the bottom meniscus of the droplet is calculated. In order to find the normal velocity ($\overline{u_{vap}}$), the thermal transport in the system is investigated as follows:

- **Conduction heat gain in the droplet from the vapor layer:** In order to estimate conduction heat transfer, the thermal resistance circuit between the hot surface and the droplet is considered. Conduction heat transfer rate is calculated as follows:

$$Q_{Conduction} = \frac{\Delta T}{\overline{\mathrm{R}}_{eq}} = \frac{T_{surface} - T_{sat}}{\overline{R}_{dielectric} + \overline{R}_{vapor}} = \frac{\Delta T_{Leiden-Frost}}{\overline{R}_{dielectric} + \overline{R}_{vapor}} = \frac{A_{base} \Delta T_{LF}}{\frac{L_d}{k_d} + \frac{L_v}{k_v}} \tag{A.14}$$

where L_v is vapor gap thickness, L_d is dielectric thickness, k_v is vapor thermal conductivity, k_d is dielectric thermal conductivity, ΔT_{LF} is the Leidenfrost superheat and A_{base} is the flattened bottom surface.

- **Radiation heat gain in the droplet from the vapor layer:** The radiation heat gain is calculated as follows:

$$Q_{Radiation-Down} = \frac{\sigma A_{base}\left(T_{surface}^4 - T_{drop}^4\right)}{\frac{1-\varepsilon_{surface}}{\varepsilon_{surface}} + \frac{1}{F_{sd}} + \frac{1-\varepsilon_{drop}}{\varepsilon_{drop}}} \tag{A.15a}$$

where σ is Stephen-Boltzmann constant, $T_{surface}$ and T_{drop} are surface and droplet temperatures, $\varepsilon_{surface}$ and ε_{drop} are emissivity's of surface and droplet and F_{sd} is the view factor. The effective radiation heat transfer coefficient as:

$$h_{r-down} = \frac{\sigma\left(T_{surface} + T_{drop}\right)\left(T_{surface}^2 + T_{drop}^2\right)}{\frac{1-\varepsilon_{surface}}{\varepsilon_{surface}} + \frac{1}{F_{sd}} + \frac{1-\varepsilon_{drop}}{\varepsilon_{drop}}} \tag{A.15b}$$

Equation A.15a can be rearranged as:

$$Q_{Radiation-Down} = h_{r-down} A_{base} (T_{surface} - T_{drop}) = h_{r-down} A_{base} \Delta T_{LF} \tag{A.15c}$$

- **Radiation losses from curved surface of the droplet:** Radiation heat transfer loss from the top surface can be modeled as:

$$Q_{Radiation-Top} = \frac{\sigma A_{Top}\left(T_{drop}^4 - T_{surr}^4\right)}{\frac{1-\varepsilon_{drop}}{\varepsilon_{drop}} + \frac{1}{F_{ds}} + \frac{1-\varepsilon_{surr}}{\varepsilon_{surr}}} \tag{A.16a}$$

Similar to equation A.15b, the effective radiation heat transfer coefficient:

$$h_{r-top} = \frac{\sigma\left(T_{drop} + T_{surr}\right)\left(T_{drop}^2 + T_{surr}^2\right)}{\frac{1-\varepsilon_{drop}}{\varepsilon_{drop}} + \frac{1}{F_{ds}} + \frac{1-\varepsilon_{surr}}{\varepsilon_{surr}}} \tag{A.16b}$$

Equation A.16a can be rearranged as:

$$Q_{Radiation-Top} = h_{r-top} A_{top} (T_{drop} - T_{surr}) = h_{r-top} A_{top} \overline{\Delta T} \tag{A.16c}$$

- **Convection losses from curved surface of the droplet:** Convection heat transfer losses from the top surface can be modeled as:

$$Q_{Convection} = h_c A_{top} (T_{drop} - T_{surr}) = h_c A_{top} \overline{\Delta T} \tag{A.17a}$$

In order to estimate h_c, it is assumed that the droplet is acting like a sphere in a stationary ambient ($\mathrm{Re}_D = 0$). For such a situation, the Nusselt number (Nu) is:

$$Nu\big|_{\mathrm{Re}_D=0} = 2 = \frac{h_{air} L_{characteritic}}{k_{air}} \tag{A.17b}$$

where h_{air} is convective heat transfer coefficient of atmosphere, $L_{characteritic}$ is the characteristic length of the droplet and k_{air} is thermal conductivity of the air around the droplet.

- **Heat absorbed by droplet evaporation:** Heat required for droplet evaporation is calculated as:

$$Q_{Evaporation} = \dot{m}_{drop}\, h_{fg} = \rho_{vap} A_{total} \overline{u_{vap}} h_{fg} \tag{A.18}$$

where h_{fg} is the latent heat of evaporation. An energy balance accounting for the above five heat transfer rates provides us with the normal velocity of vapor ejecting from bottom surface of the droplet:

$$Q_{Conduction} + Q_{Radiation-Down} - Q_{Radiation-Top} - Q_{Convection} = Q_{Evaporation} \tag{A.19a}$$

$$\frac{A_{base}\Delta T_{LF}}{\dfrac{L_d}{k_d} + \dfrac{L_v}{k_v}} + h_{r-down} A_{base} \Delta T_{LF} - h_{r-top} A_{top} \overline{\Delta T} - h_c A_{top} \overline{\Delta T} = \rho_{vap} A_{total} \overline{u_{vap}} h_{fg} \tag{A.19b}$$

Re-arranging equation A.19b will yield the vapor velocity as:

$$\overline{u_{vap}} = f_1 \times \frac{\Delta T_{LF}}{\rho_{vap} h_{fg}} \left\{ \frac{1}{\left(\dfrac{L_d}{k_d} + \dfrac{L_v}{k_v} \right)} + h_{r-down} \right\} - f_2 \times \frac{(h_{r-top} + h_c)\overline{\Delta T}}{\rho_{vap} h_{fg}} \tag{A.19c}$$

where $f_1 = \dfrac{A_{base}}{A_{total}}$ and $f_2 = \dfrac{A_{top}}{A_{total}}$. Combining equations A.19c and A.13c will result in the final expression for the upward vapor pressure force:

$$F_{up} = \frac{3}{2}\frac{\pi\mu_{vap}R_{base}^4}{L_v^{\ 3}}\left\{ f_1 \times \frac{\Delta T_{LF}}{\rho_{vap}h_{fg}}\left\{\frac{1}{\left(\frac{L_d}{k_d}+\frac{L_v}{k_v}\right)}+h_{r-down}\right\} - f_2 \times \frac{(h_{r-top}+h_c)\overline{\Delta T}}{\rho_{vap}h_{fg}}\right\} \tag{A.20}$$

A.3. Electrostatic attraction force

The magnitude of the electrostatic force attracting the droplet can be estimated by first estimating the electrostatic energy stored in the interfacial capacitance as:

$$E = \frac{1}{2}C_{eq}V^2 \tag{A.21}$$

where C_{eq} is the equivalent capacitance of the system and V is applied external voltage. The magnitude of the attractive electrostatic force on the droplet is then estimated as:

$$F_{attraction} = \frac{dE}{dz} = \frac{1}{2}V^2\frac{d}{dz}\left(C_{eq}\right) \tag{A.22a}$$

The equivalent capacitance of the vapor layer and dielectric layer is calculated as:

$$C_{eq} = \frac{C_1C_2}{C_1+C_2} = \frac{\left(\varepsilon_0\varepsilon_d\frac{A}{L_d}\right)\left(\varepsilon_0\varepsilon_{vap}\frac{A}{L_v}\right)}{\varepsilon_0\varepsilon_d\frac{A}{L_d}+\varepsilon_0\varepsilon_{vap}\frac{A}{L_v}} = \frac{\left(\frac{\varepsilon_0\varepsilon_d\varepsilon_{vap}A}{L_d}\right)}{\frac{\varepsilon_d}{L_d}L_v+\varepsilon_{vap}} = \frac{\varepsilon_0\varepsilon_{vap}A}{L_v+\frac{L_d\varepsilon_{vap}}{\varepsilon_d}} \tag{A.22b}$$

where ε_0 is vacuum permittivity, ε_{vap} is the permittivity of the vapor and ε_d is the permittivity of the dielectric layer. The electrostatic force is thus estimated as:

$$F_{attraction}=\frac{dE}{dz}=\frac{\varepsilon_0\varepsilon_{vap}A}{2}V^2\frac{d}{dz}\left(\frac{1}{z+\frac{L_d\varepsilon_{vap}}{\varepsilon_d}}\right)=\frac{\varepsilon_0\varepsilon_{vap}A}{2}V^2\left(\frac{-1}{\left(z+\frac{L_d\varepsilon_{vap}}{\varepsilon_d}\right)^2}\right) \tag{A.22c}$$

Replacing z with L_v will lead to:

$$F_{attraction}=-\frac{1}{2}\frac{\varepsilon_0\varepsilon_{vap}AV^2}{\left(L_v+\frac{\varepsilon_{vap}}{\varepsilon_d}L_d\right)^2} \tag{A.22d}$$

With a knowledge of all the forces acting on the droplet, the threshold voltage to suppress the Leidenfrost state can be obtained as described in chapter 2.

A.4. Calculation of heat pickup capacity

The physical properties for the calculations of the heat pickup fluxes in this study are provided in table below for one specific case in Figure 2.5.

Droplet size [*μL*]	5	Applied voltage [*V*]	1350
Density [*kg/μL*]	7.85×10^{-7}	Droplet lifetime [*s*]	0.8
Droplet mass [*kg*]	3.9×10^{-6}	Average heat transfer area [cm^2]	6.3×10^{-3}
Evaporation latent heat [*J/kg*]	6.66×10^{5}	Heat flux [W/cm^2]	514

Table A.1. Physical properties for calculation of heat pickup capacity.

A.5. Information about inputs for Leidenfrost state suppression model

Details of the property and geometry used to predict Leidenfrost state suppression of a 5 µL water droplet on a 360 °C surface (Figure 2.8 in chapter 2) is provided in the table below:

ε_0	$[F/m]$	8.85×10^{-12}	R_{base}	$[\mu m]$	490
ε_{vap}	[-]	1.006	A	$[\mu m^2]$	7.5×10^{5}
μ_{vap}	$[Pa.s]$	1.22×10^{-5}	f_1	[-]	0.053
ρ_{vap}	$[kg/m^3]$	0.59	f_2	[-]	0.95
k_v	$[W/mK]$	0.016	L_d	$[\mu m]$	1
ρ_{drop}	$[kg/m^3]$	958	k_d	$[W/mK]$	0.12
m_{drop}	$[kg]$	4.8×10^{-6}	h_{r-top}	$[W/\ m^2K]$	8.6
$\forall$	$[\mu L]$	5	h_{r-down}	$[W/\ m^2K]$	5.5
h_{fg}	[J/kg]	2.27×10^{6}	h_c	$[W/\ m^2K]$	140
ΔT_{LF}	$[K]$	260	$\overline{\Delta T}$	$[K]$	75

Table A.2. Parameters used for solution of differential equation to predict Leidenfrost state suppression for a 5 µL water drop (Figure 2.8).

Liquid	**Electrical conductivity at 20 °C [pS/M]**
Isopropanol	6×10^{6}
Silicone oil	0.1
Pure water	5.5×10^{6}
Drinking water	5×10^{8} - 5×10^{10}
Sea water	4.8×10^{12}

Table A.3. Electrical properties of some fluids.

Appendix B: Derivation of the analytical model to predict the vapor layer thickness on deformable surfaces

B.1. Derivation of analytical model to estimate the vapor layer thickness without considering the effects of Marangoni flows

Similar to the discussions in Appendix A, there are three forces acting on a hovering droplet on a hot deformable liquid surface. These forces include gravity, buoyancy and vapor pressure force. As per discussions in chapter 4, a spherical droplet shape is assumed, as depicted in Figure B.1.

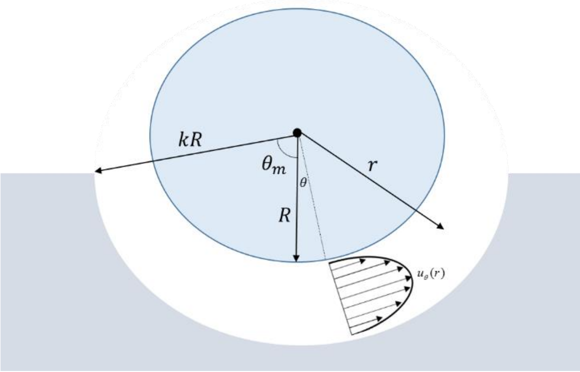

Figure B.1. Geometry used in the analytical model of the Leidenfrost state on deformable liquid substrates.

It is assumed that the substrate surface will conform to the curvature of the spherical droplet and that the variation in vapor gap is negligible. The droplet radius is assumed to be R, vapor gap thickness is h and the radius corresponding to the substrate is kR where k=1+h/R. Vapor flow is responsible for pressure build-up in the vapor layer, which supports the droplet in the Leidenfrost state. Since the vapor layer thickness is significantly lower than droplet radius ($h << R$), classical lubrication theory can be used to estimate the pressure distribution in the layer. With the assumptions of steady state, incompressible, creeping flow and axisymmetric flow, Navier-Stokes equations are simplified to estimate the Poiseuille vapor flow in the spherical shell between the liquid droplet and the pool interface as:

$$0 = -\frac{1}{r}\frac{\partial P}{\partial \theta} + \mu_{vapor}\left[\frac{1}{r^2}\frac{\partial}{\partial r}\left(r^2\frac{\partial u_\theta}{\partial r}\right)\right] \tag{B.1}$$

Next, equation above is integrated and solved for u_θ as follows:

$$u_\theta = \frac{1}{2\mu_{vapor}}\frac{\partial P}{\partial \theta}r - \frac{C_1}{r} + C_2 \tag{B.2}$$

Applying the no slip boundary conditions will result in:

$$u_\theta = \frac{1}{2\mu_{vapor}}\frac{\partial P}{\partial \theta}\left[r + \frac{kR^2}{r} - (k+1)R\right] \tag{B.3}$$

The pressure distribution is estimated by applying mass conservation to a control volume in spherical coordinates (Figure B.2):

$$2\pi R(\theta + d\theta)\int_R^{kR} u_\theta\big|_{\theta+d\theta}\,dr - 2\pi R\theta\int_R^{kR} u_\theta\big|_\theta\,dr = \overline{u_{vap}}\,(2\pi R\theta)(Rd\theta) \tag{B.4}$$

Combining equations B.3 and B.4 results in the differential equation for pressure distribution as:

$$\frac{1}{\theta}\frac{\partial}{\partial\theta}\left(\theta\frac{\partial P}{\partial\theta}\right)=\frac{4\mu_{vapor}}{R}\frac{1}{2k\ln(k)-\left(k^2-1\right)}\overline{u_{vap}} \tag{B.5}$$

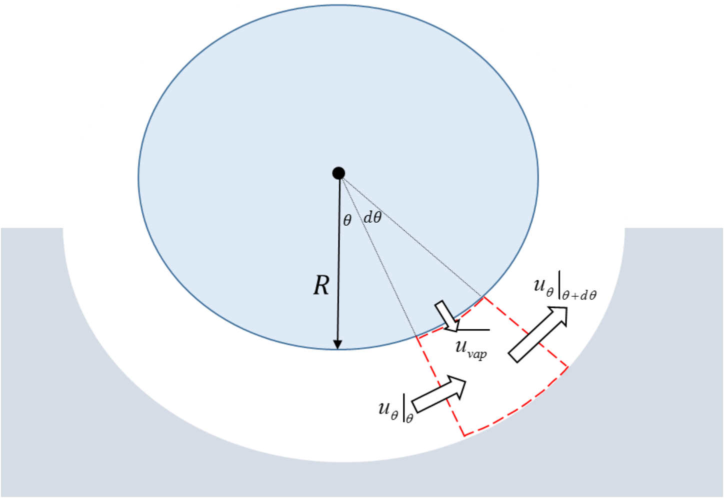

Figure B.2. Control volume for mass balance calculations.

Assuming uniform vaporization from the droplet along θ direction, the pressure distribution can be estimated as:

$$P(\theta)-P_{atm}=\frac{\mu_{vapor}}{R}\frac{\overline{u_{vap}}\theta_m^2}{2k\ln(k)-\left(k^2-1\right)}\left(1-\left(\frac{\theta}{\theta_m}\right)^2\right) \tag{B.6}$$

Integrating the vertical component of the pressure over the effective area (θ_m), provides the total upward force on the droplet as:

$$F_{vapor}=\int_{\varphi=0}^{\varphi=2\pi}\int_{\theta=0}^{\theta=\theta_m}\underbrace{\left(P(\theta)-P_{atm}\right)}_{pressure\ difference}\underbrace{\left(R^2\sin\theta d\theta d\varphi\right)}_{element\ of\ area}\underbrace{\left(\cos\theta\right)}_{Vertical\ component} \tag{B.7}$$

For the case of $\theta_m = \frac{\pi}{3}$, F_{vapor} is calculated as:

$$F_{vapor} = 1.476 \frac{R\mu_{vapor}\overline{u_{vap}}}{2k\ln(k) - \left(k^2 - 1\right)} \tag{B.8}$$

In order to calculate the vaporization velocity ($\overline{u_{vap}}$), 1D conduction heat transfer from the liquid substrate is considered. Using a similar approach as described in Appendix A, and assuming uniform vaporization, the vaporization rate can be estimated as:

$$\overline{u_{vap}} = \frac{k}{4R\left(k-1\right)} \frac{k_{vapor}\Delta T_{LF}}{\rho_{vapor}h_{fg}} \tag{B.9}$$

Combining equations (S8) and (S9) will result in the upward force as:

$$F_{vapor} = 0.37\left(\frac{k}{\left(k-1\right)\left(2k\ln(k) - \left(k^2-1\right)\right)}\right)\left(\frac{\mu_{vapor}k_{vapor}\Delta T_{LF}}{\rho_{vapor}h_{fg}}\right) \tag{B.10}$$

Vapor layer thickness can be estimated by force balance ($F_{weight} - F_{buoyancy} = F_{vapor}$). Since there is no liquid-liquid contact or triple line, surface energy terms are not included.

$$\frac{\left(k-1\right)\left(2k\ln(k) - \left(k^2-1\right)\right)}{k} = \left(\frac{0.088}{R^3}\right)\left(\frac{1}{\left(\rho_{droplet} - \rho_{air}\right)g}\right)\left(\frac{\mu_{vapor}k_{vapor}\Delta T_{LF}}{\rho_{vapor}h_{fg}}\right) \tag{B.11}$$

The above equation can be written in terms of vapor gap thickness ($k = 1 + h/R$) as:

$$\frac{\left(\frac{h}{R}\right)^3}{1+\frac{h}{R}}=\left(\frac{0.088}{R^3}\right)\left(\frac{1}{\left(\rho_{droplet}-\rho_{air}\right)g}\right)\left(\frac{\mu_{vapor}k_{vapor}\Delta T_{LF}}{\rho_{vapor}h_{fg}}\right) \tag{B.12}$$

B.2. Derivation of analytical model to estimate the vapor layer thickness, with Marangoni effects considered

As described in chapter 4, the Marangoni flows on the liquid surfaces will result in a different velocity profile in the vapor and subsequently a different vapor pressure buildup. The generic velocity profile is similar to equation B.2, however applying the slip boundary conditions will result in a different velocity distribution:

$$\mu r\frac{d}{dr}\left(\frac{u_\theta}{r}\right)=\frac{1}{r}\frac{d\sigma}{d\theta}\quad @r=kR \tag{B.12a}$$

$$\mu r\frac{d}{dr}\left(\frac{u_\theta}{r}\right)=\frac{1}{r}\frac{d\sigma}{d\theta}\quad @r=R \tag{B.12b}$$

$$u_\theta=\frac{1}{2\mu}\frac{\partial P}{\partial\theta}r-\frac{1}{\mu}\frac{d\sigma}{d\theta} \tag{B.12c}$$

Inserting the new velocity profile (equation B.12c) into the mass conservation equation B.5, will result in the differential equation for pressure distribution:

$$\frac{\partial}{\partial\theta}\left(\theta\frac{\partial P}{\partial\theta}\right)=\frac{4\mu\overline{u_{vap}}}{R\left(k^2-1\right)}\theta+\frac{4}{R\left(k+1\right)}\frac{\partial}{\partial\theta}\left(\theta\frac{\partial\sigma}{\partial\theta}\right) \tag{B.13}$$

As described earlier, the influence of Marangoni actuated flows is inherent as a surface tension gradient term. This gradient can be related to the temperature gradient on the bottom surface of the droplet as:

$$\left.\begin{array}{l}\sigma(T)=-aT+b\\ T(r)=T_c-mr\end{array}\right\}\Rightarrow\frac{d\sigma}{dr}=\frac{d\sigma}{dT}\frac{dT}{dr}=am>0 \tag{B.14}$$

Assuming uniform vaporization from the droplet along θ direction, the pressure distribution can be estimated as:

$$P_{(\theta)}-P_{atm}=\frac{\mu\overline{u_{vap}}\theta_m^2}{R\left(k^2-1\right)}\left(1-\frac{\theta^2}{\theta_m^2}\right)-\frac{4am\theta_{\mathrm{m}}}{R\left(k+1\right)}\left(1-\frac{\theta}{\theta_{\mathrm{m}}}\right) \tag{B.15}$$

Integrating the vertical component of the pressure over the effective area (θ_m), provides the total upward force on the droplet (equation B.7). Using equation B.15 and for the case of $\theta_m=\frac{\pi}{3}$, F_{vapor} is calculated as:

$$F_{vapor}=\frac{\left(1.48\right)R\mu\overline{u_{vap}}}{\left(k^2-1\right)}-\frac{\left(3.83\right)Ram}{\left(k+1\right)} \tag{B.16}$$

B.4. Estimate of electrostatic energy stored in the vapor gap

The electrostatic attraction force on the droplet can be estimated from the total electrostatic energy stored in the vapor layer (for the case of both liquid and solid substrates). Assuming that the same force is required for suppression allows a comparison of the voltage requirements of the two cases as:

$$\frac{1}{2}C_{liquid-liquid}V_{liquid-liquid}^2=\frac{1}{2}C_{liquid-solid}V_{liquid-solid}^2 \tag{B.17}$$

Capacitance of the vapor layer in the liquid-solid case is estimated as:

$$C_{liquid-solid} \sim \varepsilon_0 \frac{\pi R_{droplet}^2}{h_{liquid-solid}} \tag{B.18}$$

Capacitance of the vapor layer in the liquid-liquid case is estimated as:

$$C_{liquid-liquid} \sim \frac{\pi \varepsilon_0 R_{droplet}^2}{h_{liquid-liquid}} \left(\frac{h_{liquid-liquid}}{R_{droplet}} + 1 \right) \tag{B.19}$$

B.5. Analysis of deformation of substrates

The biggest difference between the Leidenfrost state on liquid substrates and liquid metal/solid substrates is the extent of substrate deformation. On silicone oil, the liquid substrate is substantially deformed as evident in Figures 4.2a and 4.3e. On the other hand, there is very low substrate deformation for Wood's metal, similar to the case of a solid substrate. Substrate deformation can be estimated by using equations provided in previous studies (Ding et al., 2016; Shabani et al., 2013).

Ding et al. studied deformation of liquid metal and solid substrates for different Bond numbers. Using their results, the angular location θ_m corresponding to undeformed substrate (Figure 4.6 in chapter 4) can be expressed as:

$$\theta_m = \arcsin\left(\frac{0.4Bo^{0.9}}{R} \right) \tag{B.20}$$

θ_m values for Wood's metal and aluminum substrates are 0.73° and 0.5°, respectively. θ_m is a measure of substrate deformation, with the deformation increasing at larger values of θ_m. Substrate deformation can therefore be related to this parameter.

Shabani et al. developed a fundamentals-based model to predict deformation of the interface between two liquids as a function of the density ratio and Bond number. Based on their results, θ_m for silicone oil substrate is ~ 60°. For Wood's metal and aluminum substrate, the predicted deformation is very close to zero.

B.6. Electrical properties of liquids

Electrical properties of the liquids used in the experiments (isopropanol and silicone oil) are listed below.

Liquid	**Electrical conductivity at 20 °C [pS/M]**	**Dielectric constant at 20 °C [-]**
Isopropanol	6×10^6	18.6
Silicone oil	0.1	2.5

Table B.1. Electrical properties of isopropanol and silicone oil.

Appendix C: Derivation of analytical model to predict radial temperature distribution and heat dissipation in quenching experiments

C.1. Analytical model to estimate surface temperature from measured center temperature

In the quenching experiments with stainless steel, the sphere is not isothermal and there are temperature gradients within the sphere. An analytical model is developed to estimate the surface temperature from the measured center temperature, which can then be used to estimate convective heat transfer. This model is based on a solution of the unsteady heat conduction equation with convective heat transfer boundary conditions:

$$\frac{1}{r}\frac{\partial^2 (rT)}{\partial r^2} = \frac{1}{\alpha}\frac{\partial T}{\partial t} \tag{C.1}$$

where T is temperature at radial location r, α is the thermal diffusivity and t is time. The initial and boundary conditions are:

$$T|_{r,t=0} = T_i \tag{C.2}$$

$$\left.\frac{\partial T}{\partial r}\right|_{r=0} = 0 \tag{C.3}$$

$$-k\left.\frac{\partial T}{\partial r}\right|_{r=r_0} = h\left(T_{r_0} - T_\infty\right) \tag{C.4}$$

where k is the thermal conductivity of the sphere and h is the heat transfer coefficient. Equation C.1 can be non-dimensionalized as follows:

$$\frac{1}{r^*}\frac{\partial^2 (r^*\theta^*)}{\partial r^{*2}} = \frac{\partial \theta^*}{\partial Fo} \tag{C.5}$$

where $\theta^* = \frac{T-T_\infty}{T_i-T_\infty}$ is dimensionless temperature, $r^* = \frac{r}{r_0}$ is dimensionless radial position and $Fo = \frac{\alpha t}{L_c}$ is the Fourier number, which is a measure of dimensionless time. T is the temperature at any radial position r^*, T_∞ is the liquid bath temperature, T_i is the initial temperature of the sphere, and L_c is the characteristic length of the sphere (r_0). The initial and boundary conditions then become:

$$\theta^*|_{r^*,Fo=0} = 1 \tag{C.6}$$

$$\left.\frac{\partial\theta^*}{\partial r^*}\right|_{r^*=0} = 0 \tag{C.7}$$

$$\left.\frac{\partial\theta^*}{\partial r^*}\right|_{r^*=1} = Bi\theta^* \tag{C.8}$$

where Bi is the Biot number defined as $Bi = \frac{hr_0}{k}$. Bi is the ratio of the temperature gradient within the sphere as compared to the temperature gradient at the surface.

Equation C.5 can be solved analytically using a separation of variable approach (Faghri et al., 2010). The transient temperature of the sphere at the center can be estimated as:

$$\theta_0^* = C_1 \exp(-\xi_1^2 Fo) \tag{C.9}$$

In the above equation, ξ_1 and C_1 are known constants (Bergman et al., 2011). These constants are estimated from a knowledge of the measured temperature at the center. These constants then determine (Bergman et al., 2011) the Biot number which can be used to predict the heat transfer coefficient. It is noted that the heat transfer coefficient is not constant throughout the cooling process. Furthermore, the temperature at any radial location can be estimated as (Bergman et al., 2011):

$$\theta^{*} = \theta_{0}^{*}\frac{1}{\xi_{1}r^{*}}\sin(\xi_{1}r^{*}) \tag{C.10}$$

The surface temperature is estimated by substituting $r^{*} = 1$ in the above equation. The surface temperature can then be used to estimate convective heat transfer and develop the boiling curve. It is noted that equations C.9 and C.10 are valid (Bergman et al., 2011) only for Fo numbers (measure of dimensionless time) greater than 0.2.

C.2. Analytical model to estimate surface heat dissipation

Following the derivation in section C.1., equation C.10 is rearranged to obtain T_{s}:

$$T_{s} \ = T_{\infty} + (T_{0} - T_{\infty})\frac{1}{\xi_{1}r^{*}}\sin(\xi_{1}r^{*}) \tag{C.11}$$

An estimate of the transient heat flux requires knowledge of $\frac{\partial T}{\partial r}$ at the surface where $r = r_{0}$ $(r^{*} = 1)$:

$$\frac{\partial T_{s}}{\partial r}_{@\, r=r_{0}} = \frac{(T_{0} - T_{\infty})}{\xi_{1}r_{0}}(\xi_{1}\, cos(\xi_{1}) - sin(\xi_{1})) \tag{C.12}$$

The surface heat dissipation can be estimated using:

$$q''_{(@\, r=R)} = -k\frac{\partial T}{\partial r}_{(@\, r=r_{0})} = \frac{(T_{0} - T_{\infty})}{\xi_{1}r_{0}}(\xi_{1}\, cos(\xi_{1}) - \sin(\xi_{1})) \tag{C.13}$$

It is noted that the present model uses quasi-steady approximation-based estimates of the surface temperature. Despite the significant assumptions, the model is a good and elegant tool for a first order understanding of the interfacial phenomena at play.

C.3. Additional experiments

Additional quenching experiments were conducted at temperatures exceeding 400 °C. These experiments successfully demonstrate that the proposed concept of electrical suppression works well at temperatures much higher than those analyzed in chapter 5 (400 °C). Figure C.1 shows the cooling curves for a 7/8" diameter stainless steel sphere, which is heated to 800 °C and then quenched in a liquid bath (isopropanol) with and without an EW voltage.

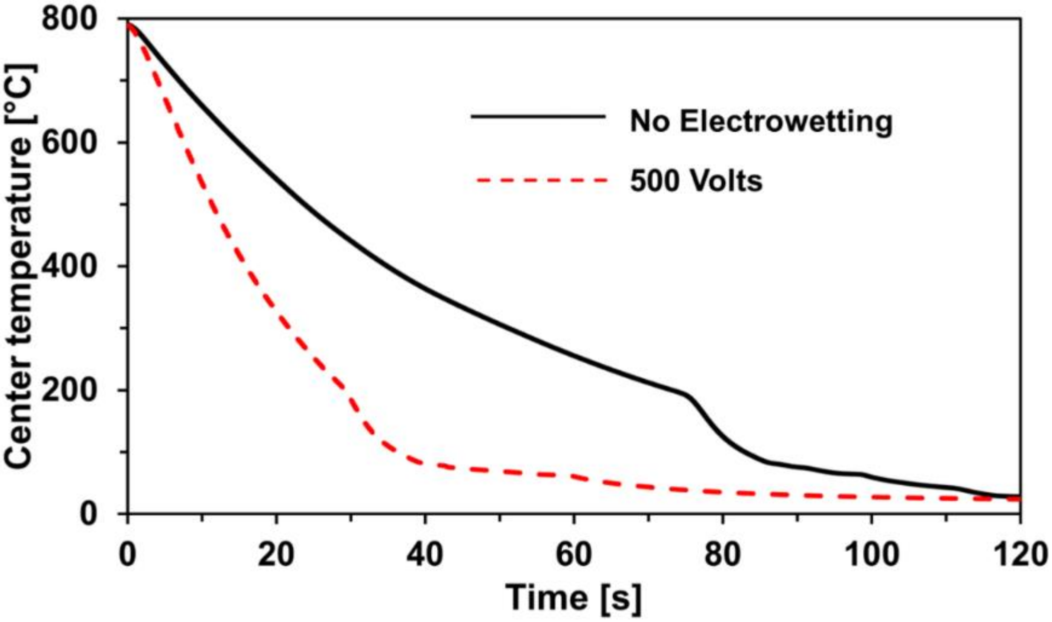

Figure C.1. Electrically tunable cooling curve showing voltage dependent cooling of a stainless steel sphere quenched in an isopropanol bath from 800 °C.

C.4. Uncertainty analysis

Uncertainty analysis was conducted for the temperature-time data in Figure 5.4 in chapter 5. The curves in Figure 4 represent the average of 3 experiments. Because the sample size of each temperature-time data point is less than 30, error bars were calculated using the standard deviation and the t-value distribution for a 95% confidence interval:

$$S_x = \left[\frac{\sum_{i=1}^{N}(x_i - \bar{x})^2}{N-1}\right]^{\frac{1}{2}} \tag{C.14}$$

where S_x is the standard deviation of N samples and $\bar{x}$ is the mean average of N samples. Using the standard deviation in the following equation yields the statistically significant error as:

$$95\%\ Confidence\ Error = \pm t_{95,\nu} \times \frac{S_x}{\sqrt{N}} \tag{C.15}$$

Where $t_{95,\nu}$ is the 95% confidence interval, N is the number of samples, S_x is the standard deviation of the N samples, and ν is the degrees of freedom, which is $N-1$. Figure C.2 shows the results of adding error bars to the temperature-time plots of Figure 5.4 in chapter 5.

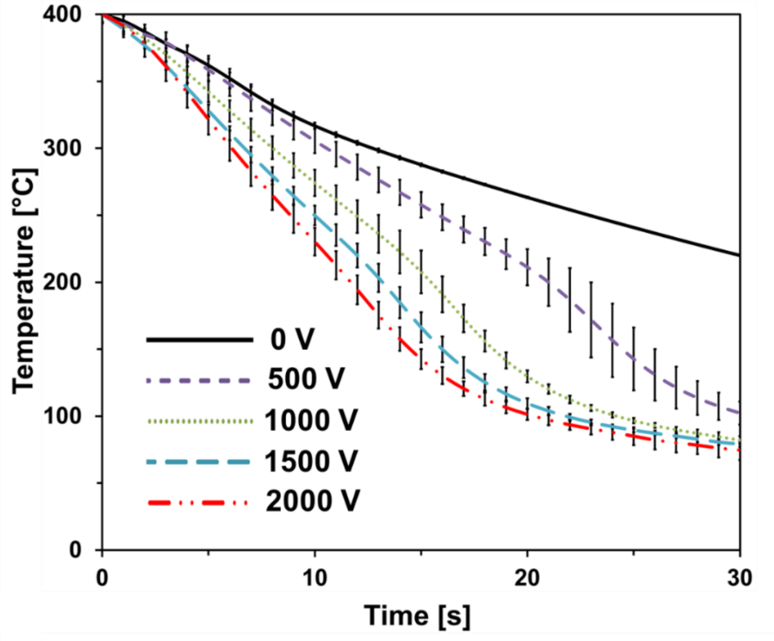

Figure C.2. Electrically tunable cooling curves showing voltage dependent cooling rates.

The average percentage error of the measurements is presented in Table C.1.

0V	500V	1000V	1500V	2000V
0.51%	6.30%	3.52%	2.88%	5.60%

Table C.1. Average percentage error in center temperature measurement.

The error data from Figure C.2 can be used to estimate the uncertainty in surface temperatures (equation C.11) using standard error propagation analysis:

$$dT_{s_{T\infty}} = \frac{\partial}{\partial T_\infty}\left[T_\infty + (T_0 - T_\infty)\frac{1}{\xi_1 r^*}\sin(\xi_1 r^*)\right] * dT_\infty \tag{C.16}$$

$$dT_{s_{T_0}} = \frac{\partial}{\partial T_0}\left[T_\infty + (T_0 - T_\infty)\frac{1}{\xi_1 r^*}\sin(\xi_1 r^*)\right] * dT_0 \tag{C.17}$$

$$dT_s = \sqrt{{dT_{s_{T_\infty}}}^2 + {dT_{s_{T_0}}}^2} \tag{C.18}$$

where dT_∞ is the uncertainty in the bath temperature, dT_0 is the precision uncertainty in the measured sphere temperature, and dT_{sT_∞} and $dT_{s_{T_0}}$ are the components of the propagated error. The average percentage error in the estimated surface temperature is detailed in Table C.2.

0V	**500V**	**1000V**	**1500V**	**2000V**
1.8%	7.6%	4.3%	3.2%	6.2%

Table C.2. Average percentage error in surface temperature estimates.

Appendix D: Metal foam-based ultrafast electronucleation of hydrates at low voltages [8]

The induction time for the nucleation of hydrates can be significantly reduced by electronucleation, which consists of applying an electrical potential across the hydrate precursor solution. This study reveals that open-cell aluminum foam-based electrodes can reduce the electronucleation induction time by as much as 150 times, when compared to non-foam electrodes. Experiments with tetrahydrofuran hydrates show that aluminum foam electrodes trigger near-instantaneous nucleation (in only 10's of seconds) at very low voltages. Furthermore, this study uncovers two distinct interfacial mechanisms underlying electronucleation, namely electrolytic bubble generation, and the formation of metal ion complex-based coordination compounds. These mechanisms (which depend on electrode material and polarity), affect the induction time to vastly different extents. This work uncovers the benefits of using foams to promote electronucleation, and shows that foams lead to more deterministic (as opposed to stochastic) nucleation when compared with non-foam electrodes.

D.1. INTRODUCTION

Clathrate hydrates (Eslamimanesh et al., 2012; Veluswamy et al., 2014) are water-based crystalline solids consisting of a guest molecule (methane, carbon dioxide, tetrahydrofuran, cyclopentane, etc.) trapped in a lattice of water molecules. Hydrate

---

[8] The contents of this Appendix is published in the following journal article: **Shahriari A**, Acharya P, Carpenter K, Bahadur V. (2017) Metal foam-based ultrafast electronucleation of hydrates at low voltages. Langmuir, 33 (23), 5652-5656. This work is included, since it is related to the general topical area of the dissertation.

formation in laboratory conditions can be challenging due to the high pressure and low temperature environment required for synthesis. Another significant challenge underlying hydrate formation is the significant induction time, before hydrates nucleate. Induction times can range from hours to days, especially in quiescent systems (Sloan et al., 2008). This poses challenges for the development of applications (Sum et al., 2009; Chatti et al., 2004), which require rapid formation of hydrates (*e.g.* desalination by forming a hydrate). The use of surfactants and mechanical agitation of the hydrate precursor solution are two common techniques to promote the nucleation of hydrates (Zhong et al., 2000; Zhang et al., 2007; Ganji et al., 2007; Ando et al., 2012).

Recently, the concept of electronucleation for rapid and controlled nucleation of hydrates was demonstrated (Carpenter et al., 2016). Experiments with tetrahydrofuran hydrate formation demonstrated significant reduction in induction times by applying electrical potentials via cylindrical stainless steel electrodes across the precursor solution. The enhancement in the nucleation time was attributed to the formation of bubbles at the electrode due to the underlying chemical reactions which was further validated by subsequent visualization experiments. The voltage-dependent induction time was reduced to a few minutes at high voltages (100 V).

This study reveals that the use of open-cell aluminum foam as the electronucleation electrode can reduce the induction time by more than 150X, when compared to non-foam (bare stainless steel) electrodes. The augmentation in the performance due to the use of such Aluminum foams could be attributed to two distinct interfacial mechanisms (electrolytic bubble generation and the hitherto unreported metal-ion complex formation for hydrates) underlying electronucleation, which depend on the polarity and electrode material. It is to be noted that a comparative study based on the efficiency of the aforementioned electrochemical mechanisms in enhancing nucleation for hydrates hasn't been reported till date. A key finding is that aluminum foam-based electrodes can trigger near-instantaneous nucleation at low voltages when used as the anode. Induction times of O (10) seconds were observed at voltages as low as 20 V, which is a significant advancement from previous findings (Carpenter et al., 2016) (induction times of a few minutes at much higher voltages of 100 V). Interestingly, the use of foams also leads to a decrease in the scatter of the otherwise widespread nucleation time measurements thus leading to a more deterministic nucleation process when compared to non-foam-based electronucleation. Furthermore, the high thermal conductivity of foams enables rapid removal of the heat of hydrate formation, which will speed up the hydrate formation process (Yang et al., 2011; Fan et al., 2012). Overall, this study identifies the electrochemistry-based mechanisms and uncovers the benefits of foam-based electronucleation.

D.2. EXPERIMENTAL METHODS

Electronucleation of tetrahydrofuran (THF) hydrates was studied in this work. It is noted that THF hydrates are commonly used as a model for methane hydrates (Wilson et al., 2005; Zhang et al., 2008; Lie et al., 2015; Wilson et al., 2010; Tombari et al., 2006), which are challenging to study since they require high-pressure conditions (> 75 atmospheres) to form. THF (C_4H_8O) forms structure II hydrates, from a THF-water mixture (stoichiometric molar ratio of THF: water is 1:17) at atmospheric pressure, and below 4.4 °C. In this work, there was an excess of THF to prevent ice formation, and the ratio of THF to water was selected as 1:15.

Figures D.1a and D.1b show a schematic depiction of the experimental setup. All experiments were conducted in a water/glycol-based cold bath. THF electronucleation was studied in glass tubes (inner diameter: 14 mm, length: 95 mm) fitted with a rubber stopper. The stopper also held the two electrodes and a thermocouple (Figure D.1b). A T-type ungrounded thermocouple was used to detect electronucleation; the use of this type of thermocouple prevents the applied voltage from influencing temperature measurements.

Open-cell aluminum foams with a porosity of 92% and a surface area-to-volume of 1720 m^2/m^3 were used in this study. A 6 mm x 8 mm x 50 mm sized foam plug was used as one of the electrodes as shown in Figure D.1b. A stainless steel electrode (diameter: 1.6 mm) was used as the other electrode. The spacing between the electrodes and the thermocouple was approximately 5 mm. The electrodes were connected to a DC power supply. Additionally, baseline electronucleation experiments were conducted with two stainless steel electrodes, *i.e.* without any foam electrode (similar configuration described in a recent study (Carpenter et al., 2016)).

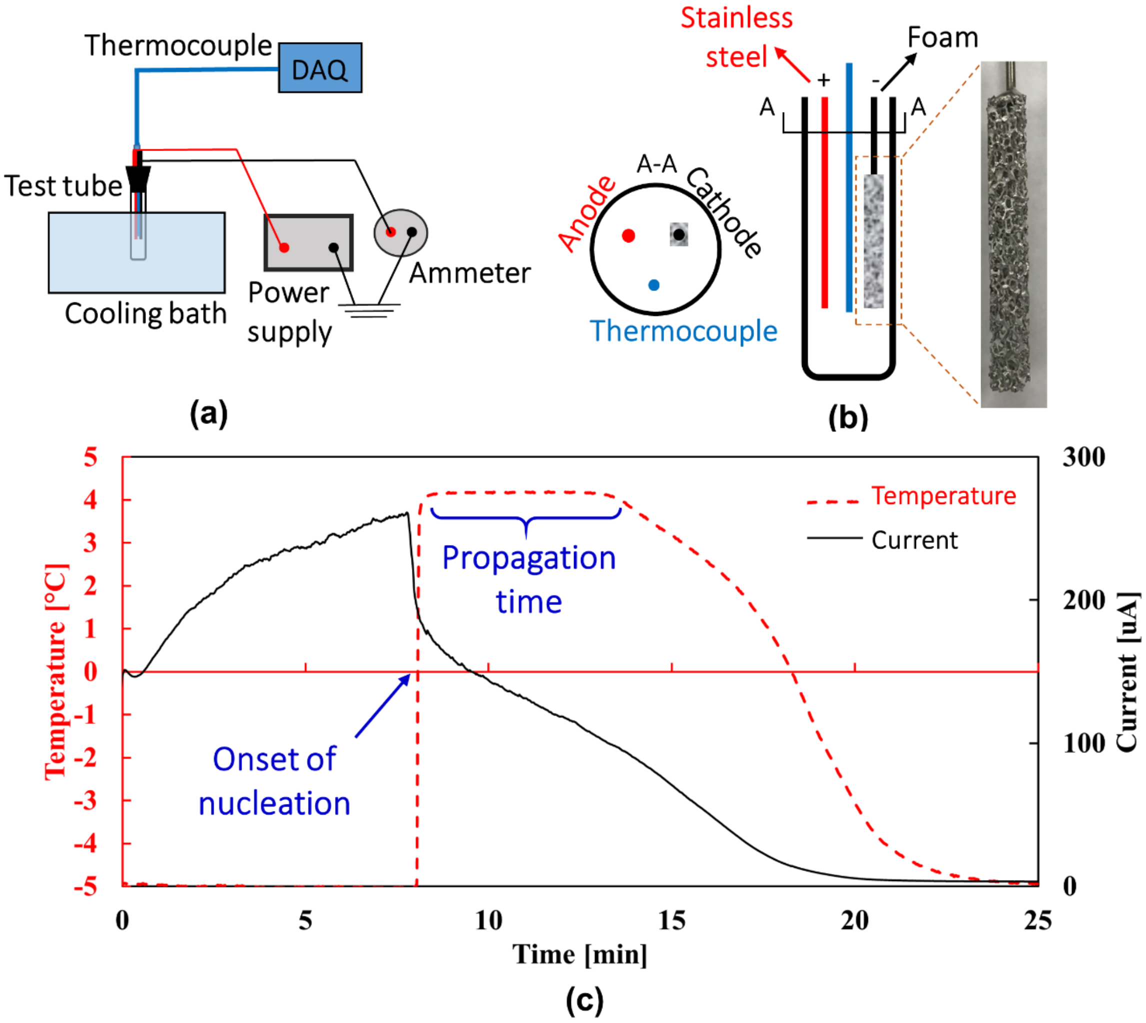

Figure D.1. (a) Experimental setup, (b) Stainless steel and aluminum foam electrodes inside the tube (right image shows the foam electrode), and c) detection of nucleation by tracking the thermal signature and current flow in the hydrate precursor solution. Figure D.1 reprinted with permission from Shahriari et al. Copyright 2017 American Chemical Society.

A single tube was used in every experimental run to avoid the possibility of nucleation in one tube influencing any other surrounding tubes in the cooling bath. Details of the cleaning steps, prior to the experiments are provided in the Supporting Information.

The tube contained 8.77 ml of THF hydrate precursor solution (water-THF mixture), which was agitated (to ensure complete mixing) and degassed to remove air bubbles (which can act as potential nucleation sites). The tube was then immersed in the cooling bath set at 5 °C. After the tube reached 5 °C, the bath temperature was lowered to -5 °C. Once the water-THF mixture supercooled to a steady temperature of -5 °C, an electrical voltage (5, 10 or 20 V DC) was applied. The induction time was measured starting from this point onwards to the time when hydrate nucleation was detected.

Electronucleation was detected by tracking the thermal signature of the solution, as detailed in a recent study (Carpenter et al., 2016). The heat released at the onset of nucleation (recalescence) instantaneously raises the temperature of the entire solution to ~ 4 °C (Figure D.1c). This also confirms that a THF hydrate is being formed and not ice, which would have otherwise led to a temperature spike to 0 °C. The second indicator10 of hydrate nucleation is a sudden decrease in the electrical conductivity of the solution (Figure D.1c). It is noted that these methods have also been used by other researchers to infer the nucleation of THF hydrates (Dai et al., 2014) and ice (Bauerecker et al., 2008; Alizadeh et al., 2012; Carpenter et al., 2015). Importantly, the magnitude of Joule heating is very low, and its influence is neglected. The maximum current in all these experiments was 86 μA, 211 μA and 803 μA at 5, 10 and 20V, respectively; this translates to less than 16 milliwatts (at 20 V) of heat generation.

D.3. RESULTS

Figure D.2 shows the measured induction times as a function of the voltage for the baseline (non-foam) case and the cases with the aluminum foam electrode acting as the cathode and anode. Each data point is the average of more than five measurements. The baseline case (with stainless steel electrodes), shows voltage dependent reduction in the induction time, in line with a recent study (Carpenter et al., 2016). The use of aluminum foam as the cathode (negative polarity electrode) significantly reduces the induction time, as evident from the 10X decrease at 20 V. This clearly highlights the benefits of foams, with the high surface area associated with the porous foams clearly aiding nucleation. In this work, the porosity of the aluminum foam resulted in a 40X enhancement in the surface area, compared to the bare electrode.

The induction time is further reduced dramatically, by switching the polarity to make the foam electrode as the anode (positive polarity electrode). Figure D.2 shows that the induction time is reduced by ~40X (at 5V) when compared to the same foam used as the cathode. The average induction times at 10 V and 20 V, with the foam anode were only 43 seconds and 20 seconds, respectively which reflects a substantial improvement in the nucleation time as well as the efficiency of the consumed electrical power when compared to a previous work (Carpenter et al., 2016) (nucleation time of the order of 7 minutes at 100 V). This is very close to instantaneous nucleation, which can enable the realization of applications which need ‘hydrates on demand’. It is noted that no nucleation was observed in any experiment at 0 V even after twelve hours. Overall, these results suggest that foams with the appropriate polarity can enable a two order of magnitude reduction in induction time as compared to non-foam electrodes. As an illustration, the induction time decreases by 150X at 5 V, when a non-foam electrode is replaced with a foam electrode as the anode.

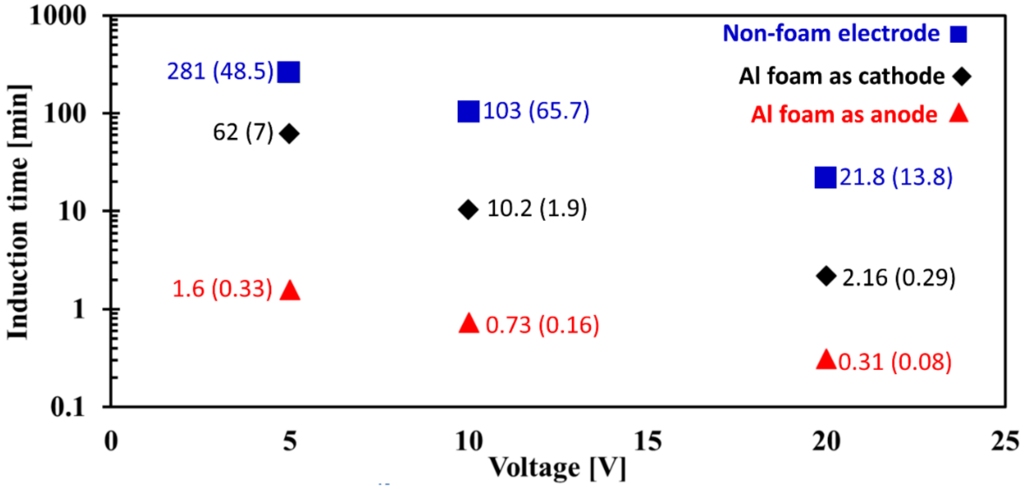

Figure D.2. Voltage-dependent electronucleation induction times for the baseline (non-foam) case, and the cases where the aluminum foam was the cathode and anode. The numbers next to the data points indicate the average and standard deviation (in parenthesis) in the measurements. Figure D.2 reprinted with permission from Shahriari et al. Copyright 2017 American Chemical Society.

An interesting observation from Figure D.2 is that the spread in the measurements is significantly reduced in the foam experiments, especially at higher voltages. The standard deviations in the induction time measurements for the non-foam experiments is ~ 60% of the mean value, for experiments at 10 and 20 V. The corresponding standard deviations with the use of foam electrodes (either as cathode and anode), are reduced to 13-25% of the mean value. This suggests that the use of foams can suppress the inherent stochastic nature of nucleation and transform nucleation to a more deterministic phenomenon.

The influence of polarity is very remarkable, with the induction time reduced by factors of 40, 14, and 7 at 5, 10, and 20V respectively, by switching the foam polarity from negative to positive. This also suggests that multiple physical phenomena are likely at play. One electronucleation mechanism briefly mentioned in a recent study (Carpenter et al.,

2016) was bubble generation at the electrodes, resulting from hydrolysis reactions. These bubbles can act as nucleation sites. Furthermore, the convection associated with bubble growth and detachment can assist in triggering nucleation. Bubble generation on the foam electrode was indeed observed as detailed below. However, this mechanism alone cannot explain the polarity-dependent induction time.

This study identifies another mechanism, which affects nucleation more profoundly than bubble-related effects, and is polarity dependent. This mechanism can be understood by examining the results of Hozumi & that of Shichiri and Nagata (Hozumi et al., 2003; Shichiri et al., 1981) who conducted experimental studies to determine the influence of electrode material on the electric field-induced freezing of pure water. Freezing was enhanced (Hozumi et al., 2003) with aluminum electrodes, as compared to more inert materials (platinum, gold). This enhancement was attributed to the formation of aluminum-based coordination compounds at the electrodes, the structure of which resembles the crystal structure of ice (Hozumi et al., 2003). Other studies (Orlowska et al., 2009; Wei et al., 2008), have also discussed the role of such metal-ion complexes in accelerating nucleation. A similar mechanism is postulated in this work to explain the accelerated hydrate formation with aluminum foam as the anode.

Both the above mechanisms can be further explained by considering the chemical reactions taking place at the electrodes. For the case of the foam electrode as the cathode, water is reduced to hydroxyl ions and hydrogen gas is generated (Figure D.3a), which accounts for the bubbles ($4H_2O + 4e^- \rightarrow 4OH^- + 2H_2 \uparrow$) observed at the cathode. The high surface area of the foam, and the presence of surface irregularities, provides a large number of nucleation sites for gas bubble generation, which explains the faster electronucleation as compared to the non-foam electrode. At the anode (stainless steel) the hydroxyl ions are oxidized to generate oxygen ($4OH^- \rightarrow O_2 \uparrow + 2H_2O + 4e^-$). Furthermore, stoichiometric calculations indicate that less than 0.001% of the water is electrolyzed; this will not change the composition of the hydrate-forming mixture.

Polarity-dependent nucleation can be explained by a different reaction occurring at the foam, when it is the anode. In this case, the oxidation of aluminum is favored (Hozumi et al., 2003) over the oxidation of hydroxyl ions, due to the high ionization tendency of aluminum ($Al \rightarrow Al^{3+} + 3e^-$). Al^{3+} ions therefore enter the solution and are surrounded by water molecules to form a coordination compound $[Al\,(H_2O)_6]^{3+}$. Furthermore, OH^- ions form bridges between the coordination compounds leading to the synthesis of an octahedral polynuclear complex (Hozumi et al., 2003) (Figure D.3b). The resemblance of this structure to the lattice structure of the hydrate promotes hydrate nucleation. While direct measurement of coordination compounds is challenging, the formation of such polynuclear complexes is a very likely mechanism for the accelerated nucleation of hydrates.

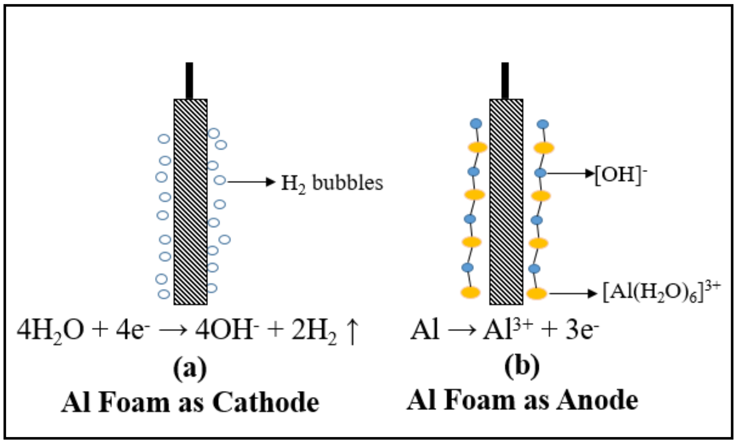

Figure D.3. Schematic depiction of mechanisms underlying electronucleation (a) Bubble-related effects when aluminum foam is the cathode (b) Coordination compound formation-based nucleation when aluminum foam is the anode. Figure D.3 reprinted with permission from Shahriari et al. Copyright 2017 American Chemical Society.

These hypotheses were validated by high magnification visualization of bubble activity in the foam electrode during electronucleation. Figure D.4 shows the aluminum foam electrode as the cathode and the anode in separate experiments. When the foam is the cathode (Figure D.4a), significant bubble generation and departures are seen on the foam surface, as depicted in Figure D.3a. In contrast, there is a trivial amount of bubble generation observed when the foam is the anode. This indicates that an alternative electrochemical reaction (oxidation of aluminum to form coordination compounds) occurs at the foam anode, which is responsible for nucleation promotion. Aluminum-based coordination compound formation thus offers a logical alternative explanation for the different (accelerated) nucleation kinetics in the absence of bubbles. Furthermore, induction time measurements indicate that the coordination compound formation mechanism influences nucleation more strongly than bubble-related effects.

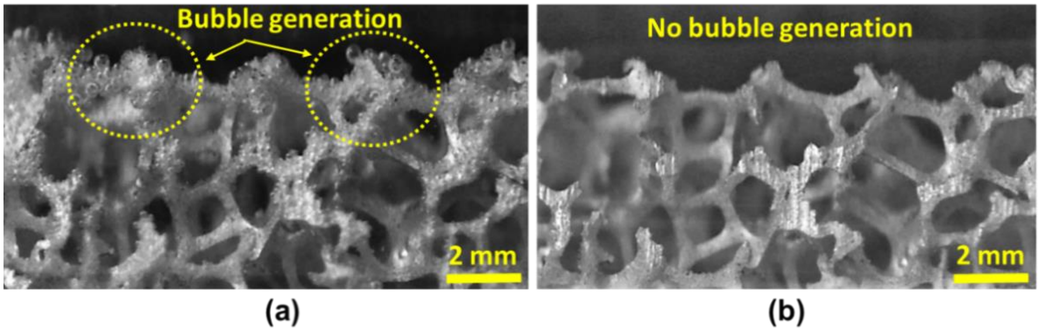

Figure D.4. Aluminum foams acting as the (a) cathode, with leads to significant bubble generation, and (b) anode, where no bubble activity is observed. Figure D.4 reprinted with permission from Shahriari et al. Copyright 2017 American Chemical Society.

D.4. DISCUSSIONS

It is important to note that metal foams also accelerate the rate at which the hydrate formation front progresses, in addition to promoting electronucleation. This can be attributed to the higher thermal conductivity of the aluminum foam-precursor solution network (11 W/mK), as opposed to the conductivity of the precursor solution alone (0.6 W/mK). Higher thermal conductivity aids removal of the heat generated during hydrate formation. In this work, the decreased time for hydrate formation was quantified by measuring the phase change propagation time, which is the time taken since the onset of nucleation to convert the entire tube to a hydrate plug. This time can be inferred from the temperature-time curve in Figure D.1c, and is summarized for various cases in Table D.1. Firstly, it is seen that the propagation time for the -5°C experiments is reduced from 7.5 minutes in the absence of foams (non-foam electrodes used) to 5.1 minutes with the foam (average of 5 experiments each with the foam as the cathode and anode). Importantly, it was seen that the foam polarity and the magnitude of the applied voltage did not measurably influence the propagation time. Repeating the experiments at -10°C shows that the propagation time is reduced from 4.8 minutes to 1.9 minutes upon using foams. The -10°C experiment was carried out in the absence of voltages, since the additional supercooling ensures nucleation with low induction times. It is noted that that hydrate formation rates are determined by all the pathways available to reject the generated heat, and the present results apply only to this particular geometry. Nevertheless, it is clear that the heat transfer benefits and the electronucleation promotion associated with foams will assist in the synthesis of hydrates.

Bath temperature	With foam electrode	Without foam electrode
-5°C	5.1	7.5
-10°C	1.9	4.8

Table D.1. Time taken for hydrates to form in the entire tube (minutes).

D.5. CONCLUSIONS

In conclusion, this study reveals that positively biased aluminum foams can enable near-instantaneous low voltage electronucleation. This study has shown upto a 150X decrease in induction time with foams, as compared to non-foam electrode electronucleation. Bubble-based mechanistic effects and electrochemistry-based mechanisms influence the nucleation kinetics. While this study utilized THF hydrates, similar benefits can be expected for other hydrate systems such as cyclopentane (hydrates form from two immiscible liquids), and methane (hydrates form from a water-gas mixture). This study suggests that foam-based electronucleation can promote rapid hydrate formation without requiring excessive supercooling, which has energy consumption reduction benefits.

Appendix E: Flow regime mapping of high inertial gas-liquid droplet microflows in flow focusing geometries [9]

Confined gas-liquid droplet microflows present a lot of new perspectives for microfluidic systems that require the presence of a gaseous phase. In addition to the benefits associated with the discretization of reactive and sensing processes, the highly inertial droplets generated in these systems can enable fast efficient mixing by pair collisions as well as high system throughput due to the short convective timescales involved in the droplet transport. Presented herein is mapping of the geometry-specific droplet generation from a binary gas-liquid flow for different flow focusing configurations. The dynamic interactions of inertia, shear stress, viscous and surface tension forces create three unique regimes in the gas-liquid flow rate space, providing adaptable flow configuration to specific applications. Analytical investigation and numerical analyses involving governing forces are also introduced to predict the effective droplet diameter versus gas flow rates. It is demonstrated found that the experimental results are well matched to the analytical predictions within 10% of uncertainty.

E.1. INTRODUCTION

Droplet-based microfluidics have become ubiquitous and of great importance for applications in biological and chemical fields, including drug delivery (Atencia et al., 2004; Yang et al., 2015, Aryafar et al., 2006; Xu et al., 2009; Marine et al., 2009; Seemann et al.,

---

[9] The contents of this appendix is published in the following journal article: **Shahriari A**, Kim M, Zamani S, Phillip N, Nasouri B, Hidrovo C. (2016) Flow regime mapping of high inertial gas-liquid droplet microflows generated in flow focusing geometries. J. Microfluid. Nanofluid. 20, 1-13. This work is included, since it involves relevant research under supervision of Prof. Carlos Hidrovo (former advisor).

2012; Li et al., 2008). This is due in part to the discrete nature, precision, and programmable controllability that droplets provide (Fair 2007; Link et al., 2006). Droplet flows allow systematic delivery of chemicals or reagents at the nanoliter scale (Sun et al., 2013; Song et al., 2006).

Over the past few decades, existing studies in droplet microfluidics have focused on oil-water systems at very low Reynolds (Re) numbers (Bolognesi et al., 2015; van Dijke et al., 2010; Hu et al., 2011; Tan et al., 2006; Utada 2005; Yobas et al., 2006). The formation and break-up of droplets in these low Re oil-water systems have been explored for various injection geometries including T-junction (Xu et al., 2008; Bedram et al., 2011; Priest et al., 2006; Thorsen et al., 2001) and flow focusing (Roberts et al., 2012; Mulligan et al., 2012; Anna et al., 2003; Zhou et al., 2006). Furthermore, precise controllability of the oil-water droplet flows due to their laminar nature have seen these systems adopted on a wide range of applications such as droplet emulsions (Lorenceau et al., 2005; Hayward et al., 2006), droplet fusion (Liu et al., 2007; Chen et al., 2012) and droplet sorting (Tan et al., 2008; Choi et al., 2005; Jung et al., 2013). While extensive analysis of oil-water droplet flows has assisted in developing a broad understanding of digital microfluidics for wet biochemistry applications, they are not suitable for chemical processes that require the introduction of a gas phase such as oxidation, hydrogenation, carbonylation, and chlorination (Wada et al., 2006; Gong et al., 2012). Other gaseous based applications include the detection of airborne particles (Piorek et al., 2007), purification of organic substances (Wheeler et al., 2006), aerosol drug delivery (Dolovich et al., 2011), point-of-care diagnostics (Ahn et al., 2004) and simulating a lung pathway (Song et al., 2011). Furthermore, the low Re nature of these flows limits the throughput of fluid transport and efficient mixing through droplet collisions in these systems.

Unlike liquid-liquid systems, gas-liquid schemes make it possible to create digital droplet microfluidics systems in applications that require the presence or involvement of a gaseous phase. One research area in gas-liquid systems that has attracted a great deal of attention is formation of monodisperse gas bubbles in liquid flow (Garstecki et al., 2004). Garsteki demonstrated a method which allows simultaneous and independent control of the size of the individual bubbles and volume fraction of the dispersed phase. Another recent study applies an ultrasonic transducer for acousticfluidic control of bubble size in microfluidic flow-focusing configuration (Chong et al., 2015). Generation of CO_2 bubbles and hydrodynamics of the two-phase flow were demonstrated in another study (Buie et al., 2009). Also encapsulation of individual gas bubbles in aqueous droplets with high gas volume fractions has been studied (Wan et al., 2012).

Similarly, liquid droplets in a gaseous environment have been another area of interest in gas-liquid systems (Carroll et al., 2013; Carroll et al., 2012; Carroll et al., 2012; Gopinath et al., 2001; Bach et al., 2004; Ben-Tzvi et al., 2010). Currently, most of these applications rely on the use of electrowetting on dielectric (EWOD) for droplet transport and control (Shabani et al., 2013; Yasuda et al., 2009). However, these are complicated and cumbersome systems that normally require involved multistep fabrication processes and have limited operation range. In contrast, pneumatic based liquid droplet systems are simpler to implement and can provide more flexibility in terms of droplet generation and range of operation. These systems are also characterized by high Re due to the high speed nature of the gas flows employed (Carroll et al., 2013; Carroll et al., 2012a). These high inertial effects can also be leveraged to achieve microsecond processing times and tens of μL/min throughputs. Despite its significance and potential, the difficulties associated with proper gas-liquid flow control has limited the extent of experimental work conducted on these microfluidic devices. The majority of studies are therefore theoretical and numerical in nature (Gopinath et al., 2001; Bach et al., 2001). Only a few experimental works are available in atmospheric phenomena, spray formation, and combustion applications (Carroll et al., 2013; Marmottant et al., 2004; Post et al., 2002). An understanding of high inertial droplet generation characteristics in gas-liquid systems at the micro scale is essential to make gaseous digital droplet microfluidics systems a reality, achieving high throughputs and fast processing times that can lead to the development of next generation Lab-on-a-Chip and micro-Total Analysis Systems. Similar to liquid-liquid droplet microfluidic applications, such as digital droplet PCR (dd-PCR) (Hindson et al., 2011) the large scale discretization of the liquid phase on the gaseous environment could open the door for the digitization of these processes. In addition, the high speed nature of these droplet flows can be exploited to enhance mixing through inertial droplet pair collisions (Carroll et al., 2012a; Carroll et al., 2012b). Note that, in addition to the pneumatic-based droplet generation, there have been extensive approaches to generate liquid droplets using active manipulations such as acoustic wave (Elrod et al., 1989), electrical signal (Gong et al., 2008), heat (Tan et al., 2008) and magnetic field (Zhang et al., 2009).

Although previous studies (Carroll et al., 2013; Gopinath et al., 2001) have provided some insights about the dynamics of liquid droplet generation (discrete phase) in a gaseous flow (continuous phase) there are few studies that investigate the fundamental relationship between the discrete and continuous flows phases and the droplet generation regime and size.

In this work, droplet formation in various flow focusing geometries that produce high Re (~450) discrete gas-liquid flows in microfluidic devices is demonstrated. Different combinations of air and water flow rates create a map of flow regimes. The relationship between droplet diameters and gas flow rate was experimentally obtained in 60° flow focusing geometry. Numerical simulations that predict this relationship have been performed and compared with the experimental results. The insight and possible applications of the high inertial droplet flows are also discussed.

E.2. EXPERIMENTAL METHODS

The experimental setup, shown in Figure E.1a, enables time resolved bright field microscopy using a high speed camera (up to 1.3 million frames/second) controlled by a customized LabVIEW program. Precise droplet generation was controlled by regulating the upstream pressure of the gas and liquid inlet lines separately (Figure E.1a). For the gas stream, the air flow rate was controlled by a pressure regulator (Proportion Air) and needle valve (Swagelok) positioned upstream of the microfluidic chip. The resolution of the pressure control with LabVIEW was 0.02 psi and the maximum line pressure in all experiments was 16 psi. A volumetric flow meter (Sierra Instruments) installed before the needle valve monitored the air flow rate (Q_a). This single line of air flow was split into two separate flows right after the flow meter by a high pressure fitting connected to the two air inlet ports in the microfluidic chip. Another pressure regulated air-line was connected into a custom aluminum chamber containing the water reservoir. Gradual pressurization of the chamber was used to control the water flow with values as low as 0.2 μL through a 1/16 inch tubing into the water inlet port in the chip. The water flow rate (Q_w) was measured by a liquid flow meter (Sensirion) just before the inlet port of the chip. An inverted microscope (Nikon) was used to image liquid droplets forming at the intersection of the gas-liquid outlets illuminated by a bright field light source (Prior Scientific) through a 10X magnification microscope objective. A CMOS high speed camera (Photron Fastcam SA5) was employed to collect sequential droplet images at the rate of 7000 frames per second.

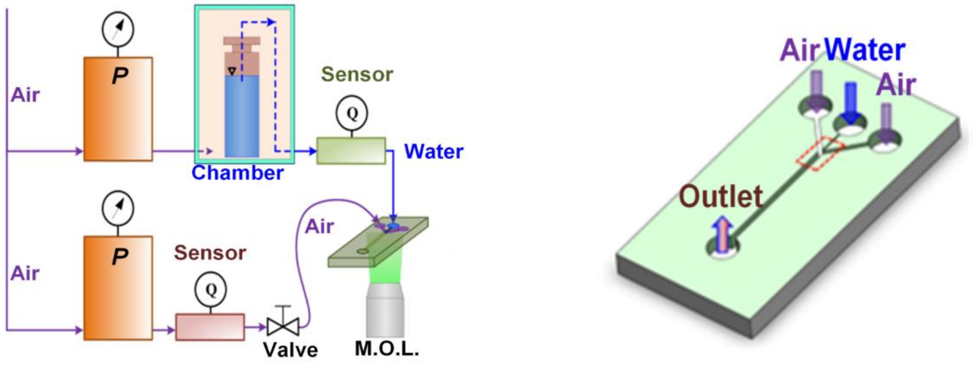

(a) (b)

Figure E.1. Schematic of experimental setup and channel configuration. (a) Experimental setup includes pressure transducers (P), flow meters (Q), microscope objective lens (M.O.L), needle valve, and pressurized chamber. (b) Channel configuration in the PDMS micro-fluidic chip. The PDMS microchannels are molded by Softlithography techniques and include two inlets for air flow, one inlet for water flow and one outlet for two phase flow. Figure E.1 reprinted with permission from Shahriari et al., Copyright 2016 Springer Nature.

Microfluidic chips used in this study were fabricated by Softlithography with PDMS (Polydimethylsiloxane). Most microfluidic devices composed of PDMS and glass are commonly assembled by a plasma treatment. Despite plasma treated PDMS surfaces becoming hydrophilic, which leads to water droplets wetting and attachment to the microchannel walls, they can be made hydrophobic by treating them with hydrophobic or fluorophilic chemicals (Tan et al., 2010). More importantly, though, plasma treated chips have a relatively weak bonding strength (Eddings et al., 2008) not capable of handling the pressures required for operation of the device. Although a previous study showed that plasma-bonded PDMS chips can withstand pressures as high as 30 psi (Thiele et al., 2011), Rupture of this particular design at the higher end of the pressures (16 psi) is observed. For these reasons, plasma-treated chips for water droplet generation were not used. Instead, PDMS-PDMS bonding for both top and bottom pieces was employed. Si wafers containing the channel configurations were fabricated by standard photolithography using a negative SU-8 photoresist (Microchem 2075). PDMS microchannels were then molded by soft lithography involving four main steps. First, the PDMS mixture, which served as the top, main section piece, was prepared by mixing a silicon elastomer base and a curing agent at a 5:1 ratio. Then, the mixture was cured at 65 °C for 75 min on a hot plate. Second, a separate mixture of the elastomer base and the curing agent was mixed at a 10:1 ratio and served as the bottom piece. This 10:1 mixture was spin coated on the glass slide using a customized fan at 500 rpm with a maximum thickness of 0.32 mm. The different mixing ratios between the top and bottom pieces promote diffusion of the cross-linkers, resulting in a permanent bond that is 50% stronger than most other PDMS bonding techniques (Eddings et al., 2008). Third, after partially curing the bottom piece at 70 °C for 25 min, the two pieces were brought into a conformal contact applying uniform pressure. Fourth, the assembled piece was cured on the hotplate at 65 °C for 24 hours for strong bonding. Using this method, more than 16 psi was sustained in the microfluidic chips. It is worth mentioning here that in recent work it was shown that the Young's modulus of 5:1 PDMS is 20% higher than that of 10:1 PDMS (Kim et al., 2013). Since the top, main section piece of the sample is made of the 5:1 PDMS (intrinsically stiffer) but the 10:1 bottom piece is substantially thinner (0.32 mm-thick) and attached to the glass, there is minimal degree of channel asymmetry due to mechanical deformation and therefore no preferential wetting of these surfaces is observed. Similarly, the permeability of PDMS in air is known to be 3.6×10-2 μm2/Pa s at 35 °C (Suh et al., 2004). The highest operation pressure in this study was 16 psi. At this pressure, the penetration depth of the air into the outer surfaces from the air channel is estimated to be around 20 μm. Although the room temperature was slightly lower than 35 °C, taking into consideration that there is little dependence of the permeability on temperature and 5 mm of PDMS thickness, the amount of air leakage due to permeation into the PDMS material is negligible at the pressure conditions tested. The experimental assessment of air flow leakage also indicated that overall air leakage rate associated with the PDMS chips is around 1-2%, within the accuracy of the flow meters employed, and therefore negligible for all effects and purposes. Figure E.2 shows SEM images of representative 60° and 30° flow focusing geometry microchannels.

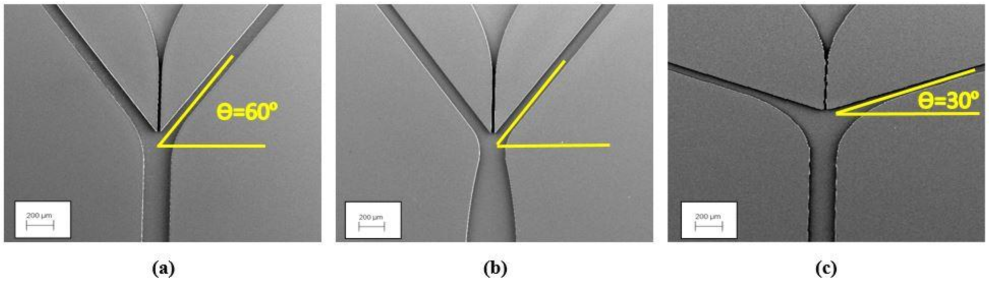

Figure E.2. Magnified view of the air-water junction showing detailed dimensional parameters. (a) 60° converging flow focusing junction, (b) 60° converging-diverging flow focusing junction, and (c) 30° converging flow focusing junction. Notice that the widths of the microchannels downstream of the flow focusing junctions remain constant. 60° and 30° are complementary angles between air and water channels. All channels have a rectangular cross section (Aspect Ratio=0.4~4) and are ~43 µm in depth. The widths of the inlet air and water channels are 100 µm and 20 µm, respectively. The main exit channel of the converging flow focusing junction configuration is 200 µm in width while the throat of the converging-diverging flow focusing junction configuration is also 200 µm and the exit channel width is 400 µm. Figure E.2 reprinted with permission from Shahriari et al., Copyright 2016 Springer Nature.

Hydrophobicity of PDMS surfaces plays an important role to successful generation of water droplets in confided microchannels. Although the intrinsic contact angle of cured PDMS is known to be 105° (Haubert et al., 2006) which is hydrophobic, due to the contact angle hysteresis of water on the PDMS surfaces, water droplets and streams tend to stick to the wall and leave liquid residue and satellite droplets behind. Therefore, the cured PDMS surfaces of the microchannels were further treated with various techniques aimed at further increasing the hydrophobicity and reducing the hysteresis, including using very soft sandpaper (grit number 240) during the microfabrication process (mild sanding of the Silicon SU-8 molds and coated glass slides) to enhance roughness (average surface roughness of 15 μm), post thermal treatment of cured PDMS, Aquapel treatment of cured PDMS surfaces, and fluorosilane deposition into the cured surfaces. Among them, it was found that fluorosilane treatment was the most efficient technique to increase the hydrophobicity of the PDMS surfaces. In detail, one of the outlets of the cured PDMS chip was connected to one side of a peristaltic pump (Parker Corp.) through a 1/16 inch tubing while the other side of the pump remains opened. A 50 μL fluorosilane was dropped on a glass slide next to the chip. The assembly of the chip-pump-glass slide was placed inside a vacuum chamber. Starting with the vacuum pump, the peristaltic pump was also powered to circulate fluorosilane molecules evaporated inside the chamber. After 2 hours the fluorosilane-coated PDMS chip was taken out from the vacuum chamber and used for experiments. Experimental contact angle measurement of original and fluorosilane treated PDMS surfaces are summarized in Table E.1.

	Original PDMS		**Fluorosilane treated PDMS**	
Mixing Ratio	10:1	5:1	10:1	5:1
Contact Angle	111.6	113.3	113	118

Table E.1. Experimental contact angle measurements of original and fluorosilane treated PDMS surfaces.

E.3. RESULTS

Three (3) types of PDMS chips with different flow focusing geometries were tested: (a) 60° converging flow focusing junction, (b) 60° converging-diverging flow focusing junction, and (c) 30° converging flow focusing junction. The rationale behind the choice of these designs was to explore (1) the effect that flow-focusing angle had on droplet formation, given that the air flow is a primary factor in the detachment process, and (2) the effect that a converging-diverging geometry, akin to "soft necking" section for liquid-liquid systems, would have on the process. The PDMS chips with different flow focusing configurations described above were used to map the various flow regimes and transitions of the air-water flows. The flow regimes found were generally divided into three categories: Dripping (droplet formation at the junction), Jetting (liquid thread with tip streaming droplet generation), and Fully Stratified flow (stable co-flowing liquid and gas streams). The maps are plotted in terms of flow rates as per traditional convention when dealing with multiphase flows.

The flow regime mapping procedure consisted of setting a starting air flow rate (Q_a) while changing water flow rate (Q_w) in increments of 2~5 μL/min. As Q_w changes, the flow regimes were recorded and identified. The same procedure was carried out for various starting values of Q_a. Collecting data points in the reverse direction (setting Q_w first and then changing Q_a) was not possible since the microchannels would get flooded/filled with water and the air flow would not be able to overcome and remove it completely to establish a droplet generating regime. So only a stratified regime is possible with this type of operation. Figure E.3 shows the different flow regimes in the converging flow focusing configuration with junction angle of 60°. At a given starting Q_a, as Q_w increases, three different flow regimes were identified: Dripping, Jetting and Stratified Flow. Each data point represents the average of three (3) experimental runs and all the transition lines for each experiment have been included in this figure to provide a sense of the transition region uncertainty. No droplet flow is observed until Q_w reaches a certain threshold, which is the transition point to start the Dripping regime. The transition values of Q_w decrease as Q_a increases because the higher inertial air flow imposes a larger dynamic force to pinch-off the water droplets forming at the junction. By further increasing Q_w, beyond the transition, consistent droplet formation was observed. At a larger Q_w value, a thin liquid thread grows from the junction and the Dripping regime transitions to Jetting, however droplets are formed at end of the thread. As Q_w is further increased, the tip of the stream keeps moving forward until it reaches the outlet port. Once the stream tip meets the outlet and a stable co-flow of gas and liquid streams is established, the flow is considered fully Stratified. The initial thickness of the stream depends on the ratio $Q^*=Q_w/Q_a$. Experimental observations revealed that by increasing Q*, the thickness increases until the liquid flow fills the entire outlet channel. Multiple tests were performed for different microchannel samples for the same junction angle for repeatability. Although the air supply pressure is set to a constant value, Q_a changes from its initial value as Q_w is increased. As first, Q_a decreases in the No Flow and Dripping regime regions as the water and droplets present a large obstruction to the air flow. Once a liquid stream is formed in the Jetting and Stratified regime regions, the water obstruction is reduced and the air flow rates increase once again. These phenomena can be addressed and quantified by doing an order of magnitude calculation of the flow resistance changes under the presence of water droplets and streams. The hydrodynamic resistance of the flow channel is defined as $R_h = \Delta P/Q$ where ΔP is the applied pressure drop through the channel and Q is the flow rate. For a rectangular channel, the flow resistance can be approximated as $R_h = 12\mu La/h^4(1-0.63a)$ where, μ is the dynamic viscosity of the fluid, L is the channel length and a is the ratio of channel height to channel width (h/w) (Tanyeri et al., 2011). From this equation it is apparent that the flow resistance is very sensitive to h and w when the fluid and channel length remain constant. Tanyeri et al., showed that the flow resistance increases significantly when there exists a channel constriction within the outlet channel. Therefore, when the water flow rates increases and a larger number of droplets are present in the channel, the effective height and width for the air flow will be significantly decreased, resulting in a large increase of the flow resistance for the air flow. This explains the decrease of air flow rate as the water flow rate increases even if the input pressure of the air flow remains constant. An order of magnitude comparison between the No Flow region and Dripping region shows a 24% increase of hydraulic resistance with average droplet size of 150 µm and 5 droplets present in the microchannel at any given time. Experimental results suggest a 20% increase which agrees with the current order of magnitude analysis. The increase in hydraulic resistance for the Stratified Flow region is 13% based on the order of magnitude analysis and 14.5% experimentally, again showing good agreement between the basic theory and data.

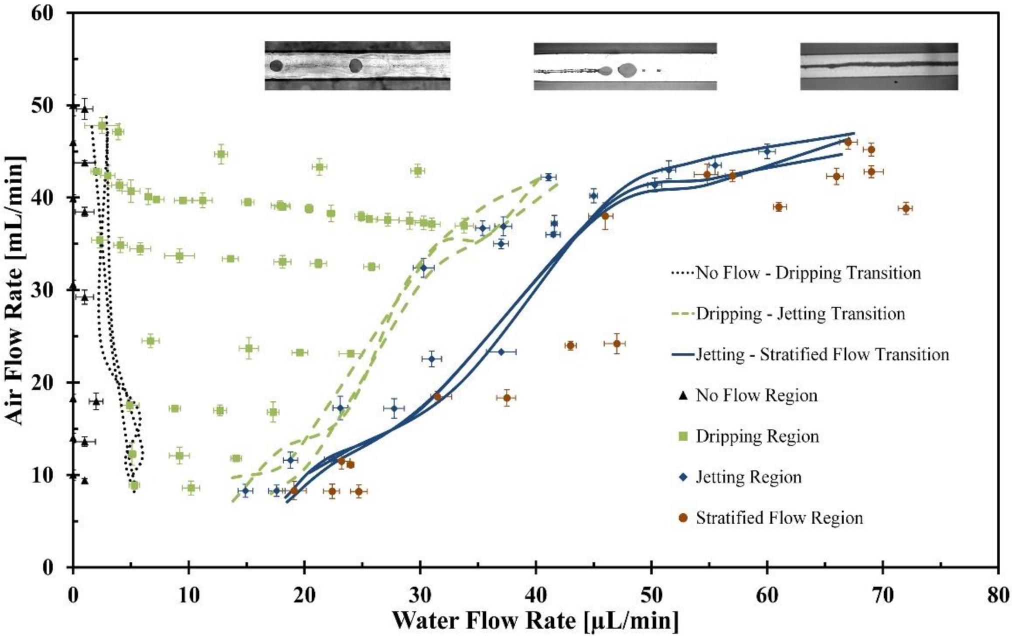

Figure E.3. Flow regime map for 60° converging configuration. Four different regimes were observed: No Flow region characterized by no droplet flow, Dripping region defined as droplet flows at certain frequencies pinched off at the junction, Jetting region described as droplet flows formed at the end of a thin liquid thread grown from the junction, Stratified region specified as a stable co-flow of gas and liquid. Figure E.3 reprinted with permission from Shahriari et al., Copyright 2016 Springer Nature.

In addition, dimensionless numbers for liquid and gas phases have been investigated in the flow regime map. Table E.2 shows Capillary number (Ca=$\frac{\mu V}{\sigma}$) and Weber number ($We = \frac{\rho V^2 l}{\sigma}$) for water at transition boundaries distinguished by air flow Reynolds number (Re=$\frac{\rho U L}{\mu}$).

	Transition to Jetting		Transition to Stratified Flow	
	Re~75	Re~380	Re~75	Re~420
Ca number	3.86×10-3	1.16×10-2	5.15×10-3	1.79×10-2
We number	1.66×10-1	1.49	2.94×10-1	3.57

Table E.2. Capillary and Weber dimensionless numbers for liquid phase at transition boundaries.

Although several factors affect the droplet detachment process, it is primarily related to the air flow conditions and occurs due to a balance between (1) the net air momentum flux (air inertial force), (2) the viscous pressure drop arising from the flow of air through the constriction created by the droplet and the channel, (3) the pressure difference between the liquid and air streams, and (4) the surface tension of the droplet (see Analytical modeling of droplet size and flow rate correlation section). On the other hand, transition from the Dripping regime into the liquid film displaying regimes (Jetting/Stratified) occurs when liquid inertia overcomes surface tension forces, disrupting the liquid containment effect provided by the droplet surface tension and leading to the formation of the film. This is evidenced in Table E.2 where it can be seen that transition into liquid film displaying regimes occurs when We ~ 0.1-1, indicating that the inertia of the liquid flow is large enough to overcome the droplet surface tension forces at the junction location. It is also evident that the larger the gas flow Re number, the larger the liquid flow We number required for these transitions is. This can be explained by the fact that the larger gas flow rates, associated with larger Re numbers, lead to larger viscous pressure drops along the length of the droplets, which is the dominating force in detaching them from the injection point. The smaller the droplets formed at the injection point are, the larger the liquid inertia needed to “break up or disrupt the droplet” and transition the liquid flow from a droplet to a film regime, as dictated by the We number. Thus, at higher air-flow rates, larger water flow rates are required to overcome the surface tension forces at the injection point and to lead the system to exhibit a Jetting regime.

Figure E.4 compares flow regime maps for junction angles of 30°and 60°. Rather than including all the different transitions lines for the different experiments as done in Figure E.3, only the “mean” transition line is presented with a thickness representative of the region uncertainty for the given transition. Similarly, the mean data points from 3 different experiments are being presented but without the error bars as in Figure E.3 for clarity of comparison between the two different geometries trends. It is apparent that the general patterns of the map for the 30° configuration are similar to those of the 60°. However, the flow regime transitions of the 30° configuration are shifted to the right, i.e. the transitions between No Droplet-Dripping, Dripping-Jetting and Jetting-Stratified Flow start at the higher Q_w compared to those at 60°. Specifically, along the No Droplet-Dripping transition line, a higher Q_w is required to form the droplets at the same Q_a. Air momentum flux perpendicular to the liquid flow (lateral inertial force), prevents lateral growth of the droplet or pinches the liquid stream, depending on which regime the flow is in. At smaller junction angles this lateral component of air momentum flux increases and therefore a higher water flow rate is required to overcome surface tension and form a droplet. Same reasoning is valid for pinching the liquid stream at the Jetting-Stratified flow transition.

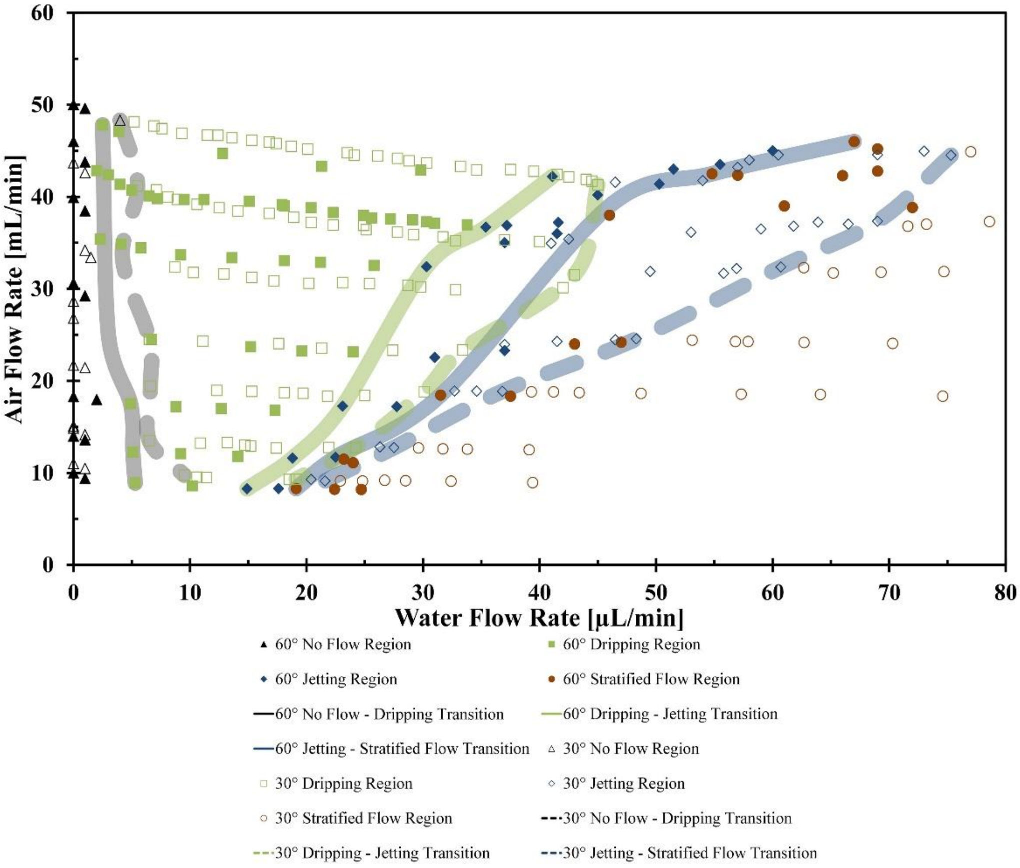

Figure E.4. Comparison of flow regime maps at 60° and 30° converging configurations. At 30° junction angle, a higher liquid flow rate is required to generate droplets since the gas momentum, which prevents lateral growth of droplet, increases. The same interpretation can be applied to the Dripping-Jetting transition. Figure E.4 reprinted with permission from Shahriari et al., Copyright 2016 Springer Nature.

Geometrical parameters play a major role in the droplet formation and detachment processes. Hence, optimization of droplet growth and pinch-off mechanics can be achieved through manipulation of the geometry and configuration at the injection section. In addition to varying the injection angles of the feeding channels, experiments were conducted with the introduction of a converging-diverging section at the injection junction that joins with the main channel section. This section allows for a smoother transition of the gas flow over the droplet and also increases the pressure difference that contributes to droplet detachment. Although the air slowdowns in the diverging portion of the converging-diverging geometry, detached droplets move out of the formation zone (throat section) before the next one is generated. In other words, droplets are being advected downstream faster than they are being generated. Figure E.5 compares the flow regimes maps for a converging-diverging section with that of a converging section for 60° injection configuration. As depicted in the map, the converging-diverging configuration provides a wider region for droplet generation, especially in the Jetting regime. It also provides much larger throughputs in the Jetting regime compared to the converging configuration. Using the converging-diverging geometry essentially provides a pressure gradient in the channel, which is believed to facilitate detachment mechanism of droplets, separating them from the stream. In the normal geometry, the flow is forced to become a stream after a threshold value, which depends on various parameters (as obtained and shown in graphs), however, using the converging-diverging geometry, the threshold value is extended farther, due to the introduction of the pressure gradient. The pressure gradient enables the flow to reach higher flow-rate, at the same time provides the condition in which droplets could be formed and detached.

If the water flow rate is large enough it overcomes the viscous pressure drop responsible for the droplet formation and transitions the flow into the Stratified regime. In the converging-diverging geometry the viscous pressure drop is higher and therefore a larger water flow rate is required for the transition to happen. This will result in a larger Jetting region. The same reasoning is valid for the Dripping region.

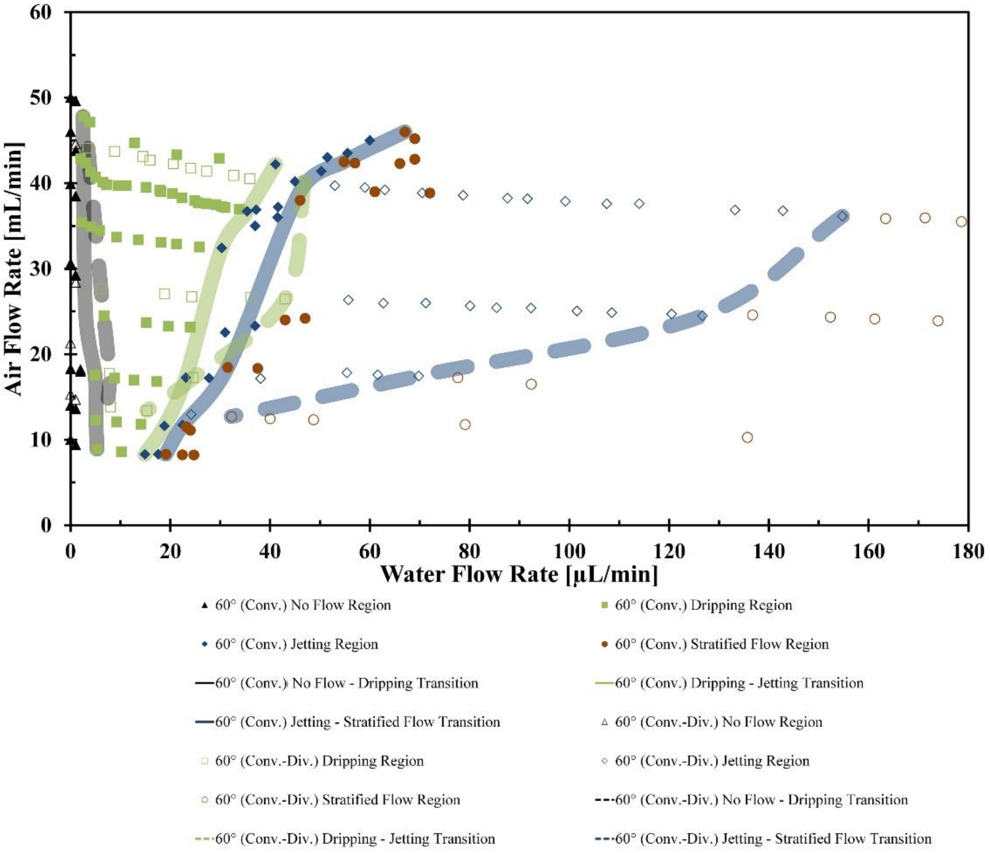

Figure E.5. Comparison of flow regime maps at 60° converging and converging-diverging configurations. The converging-diverging configuration provides a wider region for droplet generation and much larger throughputs in the jetting regime compared to the converging configuration. Figure E.5 reprinted with permission from Shahriari et al., Copyright 2016 Springer Nature.

Before finishing this section, it is important to make a note regarding the nomenclature used for the film-bearing droplet generating regime, namely the Jetting regime. The experimental documentation presented here strongly suggest that this flow patterns is more akin to a rivulet (i.e., a small stream attached to the upper and lower channels walls) that emits droplets rather than a true jet. It is important to note that if in indeed the Jetting regime is a rivulet, pneumatic control of droplet generation in this regime might not be as effective given the interactions with the walls of both the film and the droplet themselves. As such, gas flow control is more effective in the Dripping regime.

E.4. DISCUSSIONS

Understanding the governing physics behind droplet detachment is a vital step in designing optimal geometries for generating spherical liquid droplets in a gas environment at specific frequencies and sizes. In addition to flow regime mapping, the correlation of flow rate and droplet size under different flow conditions was investigated. In this section analytical investigations of droplet detachment mechanism are introduced and compared with experimental results.

In conventional oil-liquid systems, it has been known that the interactions of inertia, shear stress, viscous and surface tension forces create unique liquid droplets in T-junction (Garstecki et al., 2006) or flow focusing geometries (Christopher et al., 2007). A recent study has summarized and compared the main observations and physical understanding of dripping and jetting regimes in different microfluidics geometries (Nunes et al., 2013). In order to analyze the forces acting on the liquid droplet in a gas environment, two control volumes were defined, as shown in Figure E.6. In figure E.6a, the control volume (A) is considered stationary everywhere except at surface A3, where the front is expanding at the droplet growing velocity. Then, the general form of the momentum equation was used to find the net force acting in x-direction. Three inertial terms were considered, including momentum flux of water and air entering the C.V. at A1 and A2, and air momentum exiting the C.V. at surface A3. Due to the water/PDMS interfaces at the water inlet channel as well as the top and bottom surfaces, surface tension forces were accounted accordingly. A forward pressure force due to the pressure difference between the upstream and downstream sides of the control volume was also considered.

The same procedures were repeated for the control volume (B) in Figure E.6b to determine the lateral growth of the liquid droplet in the y-direction. The control volume (B) extends from the lower wall to just inside the droplet. The corresponding inertial terms and the pressure difference forces between the downstream and upstream locations were considered accordingly. In addition, the pressure force acting on the droplet in the y-direction due to the pressure difference between the inside and outside of the droplet should be accounted for. To find this force, the pressure difference between the inside and outside was assessed based on the mean droplet curvature and the Young-Laplace equation. The mean curvature can be measured by averaging the two principal curvatures of the droplet, namely the elliptical curvature in x-y plane and also the droplet curvature due to the hydrophobicity of PDMS to water in z-x plane using the results reported in Table E.1. Then, by plugging the obtained mean curvature in the Young-Laplace equation, the corresponding pressure force was calculated.

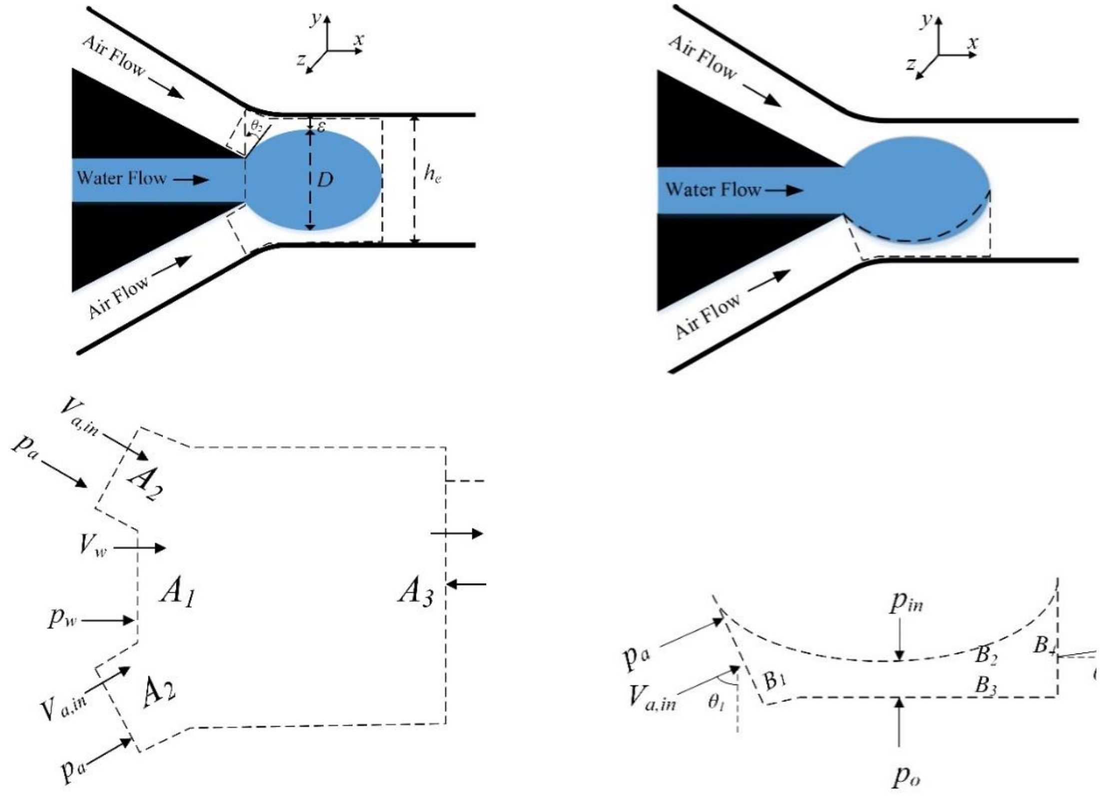

(a) (b)

Figure E.6. Control volumes for the momentum analysis in (a) x-direction and (b) y-direction. Figure E.6 reprinted with permission from Shahriari et al., Copyright 2016 Springer Nature.

In order to make this analytical problem mathematically traceable, It is assumed that: (1) The droplet is perfectly elliptical in x-y plane. (2) Velocity of the air exiting the control volume (Figure E.6a) is much higher than the growth rate of the droplet front. (3) The air flow within the gap between the droplet and channel is laminar and fully developed. (4) Due to the low Mach number (<0.3) of the air flow in the gap, this flow was considered to be incompressible. (5) Due to low Capillary number of the system, shear forces were neglected in this analysis. By employing these assumptions, the general momentum conservation on the droplet CV can be stated as:

$$\left[\text{Net momentum flux out}\right] = \sum F = \left[\text{Pressure forces}\right] + \left[\text{Surface tension forces}\right] \quad \text{(E.1)}$$

The momentum flux terms include both the air and water flows. The contribution of the water momentum flux, however, shall be neglected as the Weber number for water is as small as ~ 0.01. Thus, the governing equations finally become:

$$\begin{aligned} &\left[\frac{\rho_a {Q^2}_a}{h_a w}\left(\frac{h_a}{h_e} - 2\sin\theta_1\right)\right] = \\ &\sum F_x = \left[(p_w - p_a)h_w w + \left(\frac{Po\mu_a L_{ch} Q_a}{w\varepsilon^3}\right)h_e w\right] - \left[\sigma\left(2w\sin\theta_2 + h_w + D\right)\right] \end{aligned} \quad \text{(E.2)}$$

$$\rho_a V_{a,in}^2 B_1 \cos\theta_1 = \sum F_y = \left[\sigma\left(\frac{2}{D} + \frac{1}{R_{hp}}\right)B_3 + P_a B_1 \cos\theta_1\right] - \left[\sigma D\right] \quad \text{(E.3)}$$

Detailed description of the characters used in these equations are provided in Table E.3.

Symbol	Description	Symbol	Description
Q_a	Flow rate of air in inlet channel	w	Depth of the system (in z-direction)
ρ_a	Density of air	P_w	Water pressure at inlet channel
μ_a	Viscosity of air	ε	Distance between droplet and sidewalls of the channel
Po	Poiseuille number	L_{ch}	Characteristic length of the droplet
D	Lateral dimension of droplet	h_a, h_w, h_e	Width of air inlet channel, water inlet channel and exit channel
$V_{a,in}$	Air velocity at air inlet channel	σ	Surface tension of water in air
P_a	Air pressure at air inlet channel	R_{hp}	Curvature radius due to hydrophobicity
θ_1	Shown in Figure E.6B	θ_2	Shown in Figure E.6A
$A_i\,(i=1:4)$	Surfaces of control volume as shown in Figure E.6A	$B_j\,(\mathrm{j}=1:4)$	Surfaces of control volume as shown in Figure E.6B

Table E.3. Symbol nomenclatures used in equations E.1 and E.2.

As shown in equations E.1 and E.2, net forces in both x-direction and y-direction are the summation of terms representing pressure forces and forces due to surface tension which must balance the net momentum flux out of the CV, which is given by the outlet and inlet flow conditions of the air. Based on the experimental observations, the diameter of the droplet continues to grow laterally until it stops at its maximum diameter and stays stationary. Since this lack of droplet growth represents a steady state condition, one can conclude that the final diameter can be found using equation E.3. Also, it was experimentally observed that the growing rate of the droplet in x-direction is almost nonexistent at the moment of detachment, therefore, steady state conditions is valid and equation E.2 equally applies.

In equations E.2 and E.3, the lateral dimension of the droplet (D) and the characteristic length (L_{ch}) are the unknown parameters. Thus, at a given air flow rate and pressure difference (P_w-P_a), the final diameter of the droplet (D_{eff}) can be simply calculated. The Newton-Raphson method was then implemented in MATLAB to solve the system of equations, iteratively. The system of equations was evaluated within the pressure range in which dripping was observed. To obtain the final diameter of the droplet, it was assumed that the droplet forms a perfect spherical shape after the detachment. Thus, the effective diameter is defined as $D_{eff} = (\frac{3}{2} \times D \times L_{ch} \times w)^{1/3}$ where D is the lateral dimension calculated earlier. Figure E.7 shows experimental and analytical results of the effective droplet diameter as functions of air flow rate. In the experiments, effective droplet diameters decrease with increasing air flow rate. The higher air flow rates induce higher momentum flux changes and pressure differences across the droplets, leading to smaller effective droplet diameters. The upper and lower bounds for the expected effective droplet diameters in the numerical analysis can be found by solving equations E.1 and E.2. These bounds are computed using the maximum and minimum pressure differences employed to generate the flow regime map. It must be noted that for a given nominal flow rate, different pressure differences could be in play because there could be multiple water input pressures that would correspond to the same air flow rate, due to the unstable nature of the two phase flow.

As illustrated in Figure E.7, the analytical model bounds the experimental results well by fitting all the experimental data points within the predicted range. The implemented analytical model predicted the effective droplet diameter with the uncertainty of ~10% at a given air flow rate. It should be noted that the droplet diameter has a weak dependence on Q_w as detachment is more directly related to air flow rate.

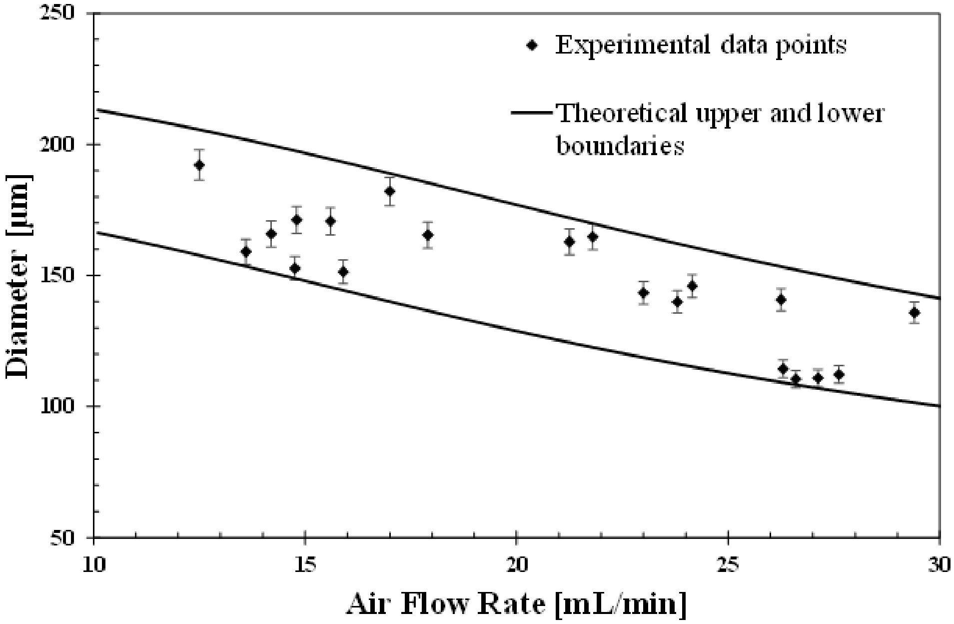

Figure E.7. Analytical and experimental results for droplet diameter versus air flow rate. Figure E.7 reprinted with permission from Shahriari et al., Copyright 2016 Springer Nature.

By taking a closer look at equation E.2, it is apparent that the net detachment force is highly dependent on the geometrical dimensions of the detachment section. Hence, adjustment of these dimensions has a significant effect on the droplet formation and growth. As illustrated in Figure E.8, in a converging-diverging channel the location of minimum width is closer to the droplet generation zone (the 200 µm width) and this will result in a smaller gap between droplet and walls (smaller ε in equation E.2). Hence, the air-flow is squeezed through a narrower path resulting in a larger viscous pressure gradient and corresponding pressure drop along the length of the droplet, leading to a larger net droplet detachment force.

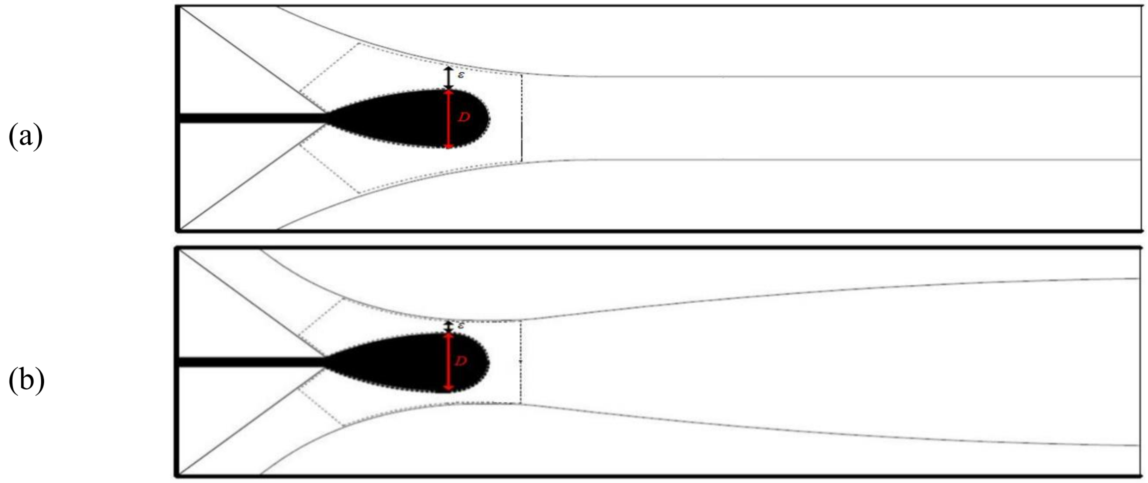

Figure E.8. (a) Converging Channel (b) Converging-Diverging Channel. The converging-diverging geometry results in a much smaller gap between channels walls and the droplet, resulting in larger viscous pressure gradient and corresponding pressure drop along the length of the droplet, leading to a larger net droplet detachment force. Figure E.8 reprinted with permission from Shahriari et al., Copyright 2016 Springer Nature.

The droplet detachment analysis can be further used to better understand the transition trends of the system from the No Flow to Dripping regime and similarly from the Dripping to Jetting regime. From equations E.2 and E.3, one can simply determine the effective diameter of the droplet at a given air flow rate. Moreover, as described earlier, the transition from No Flow to Dripping and also Dripping to Jetting occurs at a specific range of Capillary and Weber numbers. Thus, using the reported values for We number in Table E.2, one can find the water flow rate in which the regime of the flow changes by using as characteristic length scale for We the droplet diameter for a given air flow rate.

This provides a rough order of magnitude analysis in terms of the water flow rate inertia required to overcome surface tension forces and (1) create a droplet in the transition from No Flow to Dripping, and (2) shift from a droplet to a jet in the transition from Dripping to Jetting. In Figure E.9, the analytical transition lines are illustrated and compared to those of experimentally obtained, for two different geometries of 30º and 60º junction. As was observed experimentally, the water flow rate does not have a substantial effect on the droplet detachment. This effect is well captured in the analytical transition line for the case of No Flow-Dripping. However, at higher flow rates of air, shear stress between the air and the droplet becomes large enough to exert a considerable force in the direction of the water flow, therefore, lower values of water inertia are needed to form a droplet. Neglecting the effect of this force causes the model to over-predict the required water flow rate for the No Flow-Dripping regime transition, especially at higher air flow rates. On the other hand, the transition from Dripping to Jetting occurs at higher values of water flow rate than the transition analysis would predict. This is the result of neglecting the water momentum flux (water flow inertia) in the droplet detachment forces model (equation E.2), which leads to over-prediction of the droplet detachment diameter at larger water flow rates. A larger droplet detachment diameter corresponds to a lower water flow rate needed for transition, as postulated by the We number. Hence, the Dripping-Jetting transition analysis under-predicts the water flow rate needed for this transition to happen and as such this discrepancy with the experimental results grows as the water flow rate increases.

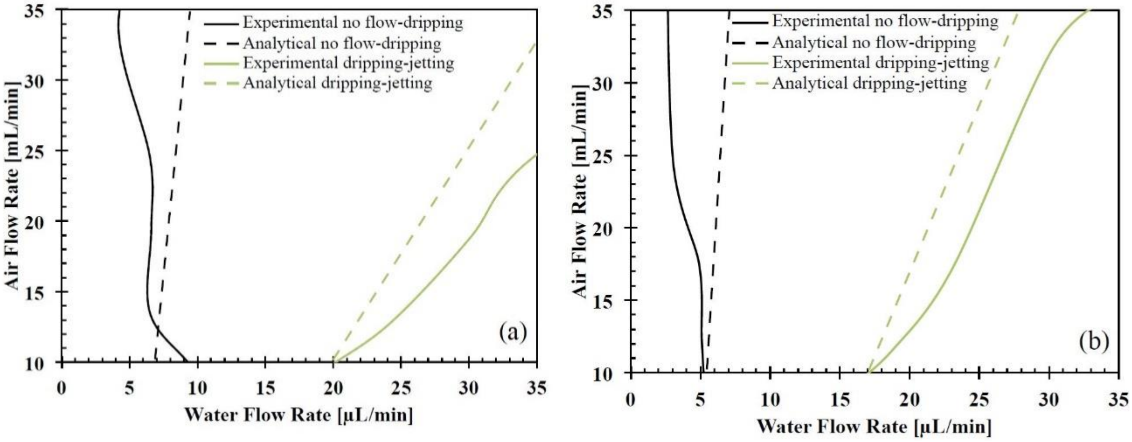

Figure E.9. Comparison of experimental and analytical transition lines of no flow-dripping and dripping-jetting for two different geometries of (a) 30° and (b) 60°. Figure E.9 reprinted with permission from Shahriari et al., Copyright 2016 Springer Nature.

E.5. CONCLUSIONS

Controlled and repeatable gas-liquid droplet generation and transport through pneumatic actuation present many possibilities for microfluidic applications requiring the presence of a gaseous phase, such as detection of airborne particles. Similar to liquid-liquid droplet microfluidic applications, such as digital droplet PCR (dd-PCR) the large scale discretization of the liquid phase on the gaseous environment could open the door for the digitization of these processes. In addition, the high speed nature of these droplet flows can be exploited to enhance mixing through inertial droplet pair collisions.

In this study different flow regimes for gas-liquid droplet generation under highly inertial conditions (Re~450) were mapped for different flow focusing configurations. The flow regimes found were divided into three categories: dripping (droplet formation at the junction), jetting (liquid thread with tip streaming droplet generation), and fully stratified flow (stable co-flowing liquid and gas streams). It was also observed that configurations with a higher junction angles initiate stable droplet generation sooner than those with lower angles. In addition, the converging-diverging junction configuration is also beneficial in terms of providing a larger map space for stable droplet generation. It encourages clean detachment of the droplets and ensures for a smoother transition into the main microchannel section. A larger water flow rate (Q_w) is required to achieve the same type of flow with the converging-diverging configurations than with converging channels. In converging-diverging geometries, Q_w in the dripping regime ranged from 2-50 μL/min with accompanying Q_a ranging from 8-50 mL/min (Fig E.4). In summary, it was seen that a converging-diverging geometry at a high junction angle is the most favorable in terms of generating stable droplets, and larger operating regions for both Dripping and Jetting. In addition to flow regime mapping, an analytic approach was taken to better understand governing physics underlying detachment process. The correlation of flow rate and droplet size under different flow conditions were analyzed.

It is important to note here that although a holistic approach to the practical implementation of gas based droplet microfluidic systems in LOC applications would also involve droplet manipulation and collection, the focus of this work has been on the specific task of droplet generation. As such, the droplets generated in the devices used in this study simple coalesce and merge at the exit of the device.

The contributions presented in this work provide new insights into the emerging field of high speed gas-liquid droplet microfluidics. It sets the foundations for further studies in this field, which can lead to the development of next generation droplet microfluidic devices for gas-liquid applications that can benefit from digitization of its associated biochemical processes.

References

Adda-Bedia, M., Kumar, S., Lechenault, F., Moulinet, S., Schillaci, M., Vella, D. (2016) Inverse Leidenfrost Effect: Levitating Drops on Liquid Nitrogen. Langmuir, 32, 4179-4188.

Adera, A., Raj, R., Enright, R. and Wang E.N. (2013) Non-wetting droplets in hot superhydrophilic surfaces. Nature Communications, 4, p. 2518.

Ahn, C.H., Choi, J., Beaucage, G., Nevin, J.H., Lee, J., Puntambekar, A., Lee, J.Y. (2004) Disposable Smart Lab on a Chip for Point-of-Care Clinical Diagnostics. IEEE 92:154-173

Al-Ahmadi, H. M., Yao, S. C. (2008) Spray cooling of high temperature metals using high mass flux industrial nozzles. Experimental Heat Transfer, 21(1), 38-54.

Alhashan, T., Elforjani, M., Addali, A., Teixeira, J. (2016) Monitoring of Bubble Formation during the Boiling Process Using Acoustic Emission Signals. Int. J. Eng. Res. Sci, 2, 66-72.

Alizadeh, A., Yamada, M., Li, R., Shang, W., Otta, S., Zhong, S., Ge, L., Dhinojwala, A., Conway, K. R., Bahadur, V. (2012) Dynamics of Ice Nucleation on Water Repellent Surfaces. Langmuir, 28, 3180−3186.

Ando, N., Kuwabara, Y., Mori, Y.H. (2012) Surfactant Effects on Hydrate Formation in an Unstirred Gas/liquid System: An Experimental Study Using Methane and Micelle-Forming Surfactants. Chem. Eng. Sci., 73, 79−85.

Anna, S.L., Bontoux, N., Stone, H.A. (2003) Formation of dispersions using flow focusing in microchannels. Appl. Phys. Lett. 82:364–366.

Arik, M., Bar-Cohen, A. (2003) Effusivity-based correlation of surface property effects in pool boiling CHF of dielectric liquids. International Journal of Heat and Mass Transfer, 46: 3755–3764.

Arik, M., Kosar, A., Bostanci, H. and Bar-Cohen, A. (2011) Pool Boiling Critical Heat Flux in Dielectric Liquids and Nanofluids. Advances in Heat Transfer, 43, p. 1-76.

Aryafar, H., Kavehpour, H.P. (2006) Droplet coalescence through planar surfaces. Phys. Fluids 18:072105.

Atencia, J., Beebe, J. (2004) Controlled microfluidic interfaces. Nature 437:648-655.

Aussillous, P., Quere, D. (2001) Liquid Marbles. Nature, 411, 924-927.

Babu, K. and T. S. Prasanna Kumar, T.S., J. (2011) Heat Transfer 133, 071501-1.

Bach, G.A., Koch, D.L., Gopinath, A. (2004) Coalescence and bouncing of small aerosol droplets. J. Fluid Mech. 518:157–185.

Bahadur, V., Garimella S.V. (2008) Electrowetting-based control of droplet transitions and morphology on artificially microstructured surfaces. Langmuir, 24, 8338-8345.

Bahadur, V., Garimella S.V. (2008) Energy minimization-based analysis of electrowetting for microelectronics cooling applications. Microelectronics Journal, 39, 957-965.

Bahadur, V., Garimella S.V. (2006) An energy-based model for electrowetting-induced droplet motion. Journal of Micromechanics and Microengineering, 16, 1494-1503.

Bahadur, V., Garimella, S.V. (2007) Electrowetting-based control of static droplet states on rough surfaces. Langmuir, 23, 4918-4924.

Bar-Cohen, A., Celata, G.P., Klausner, J., Fujita, Y. (2000) Boiling 2000: Phenomena and emerging applications, Vol 1&2, (Proceedings UEF Conference, Anchorage, Alaska, May 2000), Begell House, NY.

Basu, N., Warrier, G.R., Dhir, V.K. (2002) Onset of Nucleate Boiling and Active Nucleation Site Density During Subcooled Flow Boiling. Journal of Heat Transfer, 124: p. 717-728.

Bauerecker, S., Ulbig, P., Buch, V., Vrbka, L., Jungwirth, P. (2008) Monitoring Ice Nucleation in Pure and Salty Water via High-Speed Imaging and Computer Simulations. J. Phys. Chem. C, 167, 7631−7636.

Bedram, A., Moosavi, A. (2011) Droplet breakup in an asymmetric microfluidic T Junction. Eur. Phys. J. E Soft Matter 34:1-8.

Ben-Tzvi, P., Rone, W. (2010) Microdroplet generation in gaseous and liquid environments. Microsyst. Technol. 16:333-356

Bergman, T., Lavine, A. S., Incropera, F. P., Dewitt, D. P. (2011) Fundamentals of Heat and Mass Transfer, 7th edition, John Wiley & Sons.

Bernardin, J. D., Mudawar, I. (1999) The Leidenfrost point: Experimental study and assessment of existing models. J. Heat Transfer 121, 894–903.

Bernardin, J. D., Mudawar, I. (1996) An experimental investigation into the relationship between temperature-time history and surface roughness in the spray quenching of aluminum parts. Journal of engineering materials and technology, 118(1), 127-134.

Biance, A.L., Clanet, C., Quere, D. (2003) Leidenfrost drops. Phys. Fluids 15, 1632–1637.

Bigham, S., Moghaddam, S. (2011) Microscale study of mechanisms of heat transfer during flow boiling in a microchannel. International Journal of Heat and Mass Transfer, 88: p. 111–121.

Bologa, M.K., Kozhevnikov, I.V., Mardarskii, O. I., Polikarpov, A.A. (2012) Boiling heat transfer in the field of electric forces. Surf. Eng. Appl. Elect., 48, 329-331.

Bolognesi, G., Hargreaves, A., Ward, A.D., Kirby, A.K., Bain, C.D., Ces, O. (2015) Microfluidic generation of monodisperse ultra-low interfacial tension oil droplets in water. RSC Adv. 5:8114-8121.

Buie, C.R., Santiago, J.G. (2009) Two-phase hydrodynamics in a miniature direct methanol fuel cell. Int. J. Heat Mass Transfer 52:5158-5166

Burton, J. C., Sharpe, A. L., van der Veen, R. C. A., Franco, A., Nagel, S. R. (2012) Geometry of vapor layer under a leidenfrost droplet. Phys. Rev. Lett., 109, 074301.

Carey, V. (2007) Liquid Vapor Phase Change Phenomena, 2nd edition, Washington, D.C.: Taylor and Francis.

Carmi, R., Bussiba, A., Widenfeld, G., Aharon, Y., Alon, I., Hochbaum, I. (2011) Detection of transient zones during water boiling by acoustic emission. J. Acoustic Emission, 29, 89-97.

Carpenter, K., Bahadur, V., (2016) Electronucleation for rapid and controlled formation of hydrates. J. Phys. Chem. Lett., 7(13), 2465-2469

Carpenter, K., Bahadur, V. (2015) Electrofreezing of Water Droplets under Electrowetting Fields. Langmuir, 31, 2243–2248.

Carrica, P., Di Marco, P. and Grassi, W. (1997) Nucleate pool boiling in the presence of and electric field: effect of subcooling and heat-up rate. Experimental Thermal and Fluid Science, 15: p. 213–220.

Carroll, B., Hidrovo, C.H. (2012) Droplet collision mixing diagnostics using single fluorophore LIF. Exp. Fluids 53:1301–1316.

Carroll, B., Hidrovo, C.H. (2012) Experimental Investigation of Inertial Mixing in Colliding Droplets. Heat Trans. Eng. 34:1–12.

Carroll, B., Hidrovo, C.H. (2013) Droplet Detachment Mechanism in a High-Speed Gaseous Microflow. J. Fluid Eng. 135:071206.

Celestini, F., Kirstetter, G. (2012) Effect of an electric field on a Leidenfrost droplet. Soft Matter 8, 5992.

Chatti, I., Delahaye, A., Fournaison, L., Petitet, J. P. (2004) Benefits and Drawbacks of Clathrate Hydrates: A Review of Their Areas of Interest. Energy Convers. Manag., 46, 1333–134.

Chen, Y.T., Chang, W.C., Fang, W.F., Ting, S.C., Yao, D.J., Yang, J.T. (2012) Fission and fusion of droplets in a 3-D crossing microstructure. Microfluid. Nanofluid. 13:239-247.

Chen, F., Liu, D. and Song, Y. (2012) Visualization of a single boiling bubble in a DC electric field. Proceedings of the ASME 2012 Fluids Engineering Summer Meeting FEDSM2012.

Chen, L., Bonaccurso, E. (2014) Electrowetting-from statics to dynamics. Adv. Colloid Interface Sci., 210, 2.

Chen, R., Lu, M-C., Srinivasan, V., Wang, Z., Cho, H., Majumdar, A. (2009) Nanowires for enhanced boiling heat transfer. Nano Lett., 9(2), 548-553.

Cho, H.J., Mizerak, J.P. and Wang, E.N. (2015) Turning bubbles on and off during boiling using charged surfactants. Nature Communications, 6: 8599.

Choi, S., Park, J.K. (2005) Microfluidic system for dielectrophoretic separation based on a trapezoidal electrode array. Lab Chip. 5:1161–1167.

Chong, Z.Z., Tor, S.B., Loh, N.H., Wong, T.N., Gñáan-Calvo, A.M., Tan, S.H., Nguyen, N.T. (2015) Acoustofluidic control of bubble size in microfluidic flow-focusing configuration. Lab Chip. 15:996-999.

Christopher, G.F., Anna, S.L. (2007) Microfluidic methods for generating continuous droplet streams. J. Phys. D: Appl. Phys. 40: R319-R336.

Chu, K-H., Enright, R., Wang, E. N. (2012) Structured surfaces for enhanced pool boiling heat transfer. Appl. Phys. Lett., 100, 241603.

Chu, K-H., Joung, Y. S., Enright, R., Buie, C. R., Wang, E. N. (2013) Hierarchically structured surfaces for boiling critical heat flux enhancement. Appl. Phys. Lett., 102, 151602.

Cipriani, M., Di Marco, P., Grassi, W. (2004) Effect of an externally applied electric field on pool film boiling of FC-72. Heat Transfer Eng., 25(6), 3-13.

Cooke, D., Kandlikar, S. G. (2012) Effect of open microchannel geometry on pool boiling enhancement. Int. J. Heat Mass Transfer, 55 (4), 1004-1013.

Couder, Y., Fort, E., Gautier, C. H., Boudaoud, A. (2005) From bouncing to floating: Noncoalescence of drops on a fluid bath. Phys. Rev. Lett., 94, 177801.

Cudina, M. (2003) Detection of cavitation phenomenon in a centrifugal pump using audible sound. Mechanical systems and signal processing, 17, 1335-1347.

Dai, S., Lee, J. Y., Santamarina, J. C. (2014) Hydrate Nucleation in Quiescent and Dynamic Conditions. Fluid Phase Equilib., 378, 107−112.

Davanlou, A., Kumar, R. (2015) Counter-current motion of a droplet levitated on a liquid film undergoing Marangoni convection. International Journal of Heat and Mass Transfer, 89, pp.345-352.

Davanlou, A. (2016) The role of liquid properties on lifetime of levitated droplets. Langmuir, 32, 9736-9742.

Dhillon, N.S., Buongiorno, J. and Varanasi, K.K. (2015) Critical heat flux maxima during boiling crisis on textured surfaces. Nature Communications, 6: 8247.

Dhir, V. (1998) Boiling heat transfer. Annu. Rev. Fluid Mech., 30, 365-401.

Dhir, V.K., Warrier, G.R. and Aktinol, E. (2013) Numerical Simulation of Pool Boiling: A Review. Journal of Heat Transfer, 135: p. 061502-1-061502-17.

Di Marco, P., Grassi, W. (2011) Effects of external electric field on pool boiling: Comparison of terrestrial and microgravity data in the ARIEL experiment. Experimental Thermal and Fluid Science, 35: p. 780–787.

Di Marco, P., Grassi, W., Memoli, G., Takamasa, T., Tomiyama, A. and Hosokawa, S. (2003) Influence of electric field on single gas-bubble growth and detachment in microgravity. International Journal of Multiphase Flow, 29: p. 559–578.

Di Marco, P., Raj, R., Kim, J. (2011) Boiling in variable gravity under the action of electric field: results of parabolic flight experiments. J. Phys.: Conf. Ser., 327, 012039.

Ding, Y., Liu, J. (2016) Dynamic interactions of Leidenfrost droplets on liquid metal surface. Appl. Phys, Lett., 109, 121904.

Dolovich, M.B., Dhand, R. (2011) Aerosol drug delivery: developments in device design and clinical use. Lancet 377:1032-45.

Eddings, M.A., Johnson, M.A., Gale, B.K. (2008) Determining the optimal PDMS-PDMS bonding technique for microfluidic devices. J. Micromech. Microeng. 18:067001.

Elele, E. O., Shen Y., Pettit, D. R., Khusid, B. (2015) Detection of a dynamic cone-shaped meniscus on the surface of fluids in electric fields, Phys. Rev. Lett. 114, 054501.

Elrod, S.A., Hadimioglu, B., Khuri-Yakub, B.T., Rawson, E.G., Richley, E., Quate, C.F., Mansour, N.N., Lundgren, T.S. (1989) Nozzleless droplet formation with focused acoustic beams. J. Appl. Phys. 65:3441-3447.

Eslamimanesh, A., Mohammadi, A. H., Richon, D., Naidoo, P., Ramjugernath, D. (2012) Application of Gas Hydrate Formation in Separation Processes: A Review of Experimental Studies. J. Chem. Thermodyn., 46, 62−71.

Faghri, A., Zhang, Y., Howell, J.R. (2010) Advanced Heat and Mass Transfer. Global Digital Press, P. 247.

Fair, R.B. (2007) Digital microfluidics: is a true lab-on-a-chip possible?, Microfluid. Nanofluid. 3:245–281.

Fan, S., Yang, L., Lang, X., Wang, Y., and Xie, D. (2012) Kinetics and thermal analysis of methane hydrate formation in aluminum foam. Chem. Eng. Sci., 82, pp. 185–193.

Fang, X., Chen, Y., Zhang, H., Chen, W., Dong, A. and Wang, R. (2016) Heat transfer and critical heat flux of nanofluid boiling: A comprehensive review. Renewable and Sustainable Energy Reviews, 62: p. 924–940.

Farokhnia, N., Sajadi, S. M., Irajizad, P., Ghasemi, H. (2017) Decoupled Hierarchical Structures for Suppression of Leidenfrost Phenomenon. Langmuir, 33 (10), 2541-2550.

Gambhire, P., Thaokar, R. M. (2011) Linear stability analysis of electrohydrodynamic instabilities at fluid interfaces in the "small feature" limit, Eur. Phys. J. E. 34:84.

Ganji, H., Manteghian, M., Sadaghiani zadeh, K., Omidkhah, M. R., Rahimi Mofrad, H. (2007) Effect of Different Surfactants on Methane Hydrate Formation Rate, Stability and Storage Capacity. Fuel, 86, 434−441.

Garstecki, P., Fuerstman, M.J., Stone, H.A., Whitesides, G.M. (2006) Formation of droplets and bubbles in T-junction –Scaling and mechanism of breakup. Lab Chip. 6:437-446.

Garstecki, P., Gitlin, I., DiLuizio, W., Whitesides, G.M., Kumacheva, E., Stone, H.A. (2004) Formation of monodisperse bubbles in a microfluidic flow focusing device. Appl. Phys. Lett. 85:2649-2651.

Geisler, K.J.L., Bar-Cohen, A. (2009) Confinement effects on nucleate boiling and critical heat flux in buoyancy-driven microchannels. International Journal of Heat and Mass Transfer, 52: p. 2427–2436.

Gong, J., Kim, C.J. (2008) All-electronic droplet generation on-chip with real-time feedback control for EWOD digital microfluidics. Lab Chip 8:898-906.

Gong, X., Miller, P.W., Gee, A.D., Long, N.J., de Mello, A.J., Vilar, R. (2012) Gas–liquid segmented flow microfluidics for screening Pd-Catalyzed carbonylation reactions. Chem. Eur. J. 18:2768–2772.

Gopinath, A., Koch, D.L. (2001) Dynamics of droplet rebound from a weakly deformable gas-liquid interface. Physics Fluid 13:3526-3532.

Gottfried, B. S., Lee, C. J., Bell, K. L. (1966) The leidenfrost phenomenon: film boiling of liquid droplets on a flat plate, Int. J. Heat Mass Transfer, 9, 1167-1187.

Grassi, W., Testi, D. (2006) Heat Transfer Enhancement by Electric Fields in Several Heat Exchange Regimes. Annals of the New York Academy of Sciences, 1077: p. 527–569.

Grounds, A., Still, R., Takashina K. (2012) Enhanced droplet control by transition boiling. Scientific Reports, 2, 720.

Haubert, K., Dryer, T., Beebe, D. (2006) PDMS bonding by means of a portable, low-cost corona system. Lab Chip. 6:1548-1549.

Hayward, R.C., Utada, A.S., Dan, N., Weitz, D.A. (2006) Dewetting instability during the formation of polymersomes from block-copolymer-stabilized double emulsions. Langmuir 22:4457–4461.

Hickman, K. C. D. (1967) Floating drops and liquid boules - A further look. Industrial & Engineering Chemistry, 59 (10), 18-41.

Hickman, K. C. D. (1964) Floating drops and liquid boules. Industrial & Engineering Chemistry, 56 (6), 18-31.

Hindson, B.J., Ness, K.D., Masquelier, D.A., Belgrader, P., Heredia, N.J., Makarewicz, A.J., Bright, I.J., Lucero, M.Y., Hidessen, A.L., Legler, T.C., Kitano, T.K., Hodel, M.R., Petersen, J.F., Wyatt, P.W., Steenblock, E.R., Shah, P.H., Bousse, K.J., Troup, C.B., Mellen, J.C., Wittmann, D.K., Erndt, N.G., Cauley, T.H., Koehler, R.T., So, A.P., Dube, S., Rose, K.A., Montesclaros, L., Wang, S., Stumbo, D.P., Hodges, S.P., Romine, S., Milanovich, F.P., White, H.E., Regan, J.F., Karlin-Neumann, G.A., Hindson, C.M., Saxonov, S., Colston, B.W. (2011) High-Throughput Droplet Digital PCR System for Absolute Quantitation of DNA Copy Number. Anal. Chem. 83 (22):8604-8610.

Hozumi, T., Saito, A., Okawa, S., Watanabe, K. (2003) Effects of electrode materials on freezing of supercooled water in electric freeze control. Int. J. Refrig., 26, 537-542.

Hu, W., Ohta, A.T. (2011) Aqueous droplet manipulation by optically induced Marangoni circulation. Microfluid. Nanofluid. 11:307-316.

Huang, C-K., Carey, V. P. (2007) The effects of dissolved salts on Leidenfrost transition Conditions. Int. J. Heat Mass Transfer, 50, 269-282.

Janssens, S. D., Koizumi, S., Fried, E. (2017) Behavior of self-propelled acetone droplets in a Leidenfrost state on liquid substrates. Physics of Fluids, 29, 032103.

Jones, T.B. (2001) Liquid Dielectrophoresis on the Microscale. Journal of Electrostatics, 51: p. 290-299.

Jones, T. B., Wang, K. L. (2004) Frequency dependent electromechanics of aqueous liquids: electrowetting and dielectrophoresis. Langmuir 20, 2813–8.

Jones, T. B. (2002) On the relationship of dielectrophoresis and electrowetting. Langmuir 18, 4437–43.

Jones, T. B., Fowler, J. D., Chang, Y. S., Kim, C. J. (2003) Frequency-based relationship of electrowetting and dielectrophoretic liquid microactuation. Langmuir 19, 7646–51.

Jung, J.H., Lee, K.H., Lee, K.S., Ha, B.H., Oh, Y.S., Sung, H.J. (2013) Optical separation of droplets on a microfluidic platform. Microfluid. Nanofluid. 16:635-644.

Kim, M., Moon, B.U., Hidrovo, C.H. (2013) Enhancement of the thermo-mechanical properties of PDMS molds for the hot embossing of PMMA microfluidic devices. J Micromech Microeng. 23:095024.

Kim, B.J., Lee, J.H. and Kim, K.D. (2016) Improvements of critical heat flux models for pool boiling on horizontal surfaces using interfacial instabilities of viscous potential flows. International Journal of Heat and Mass Transfer, 93: p. 200-206.

Kim, B.J., Lee, J.H. and Kim, K.D. (2015) Rayleigh–Taylor instability for thin viscous gas films: Application to critical heat flux and minimum film boiling. International Journal of Heat and Mass Transfer, 80: p. 150-158.

Kim, D.E., Yu, D.I., Jerng, D.W., Kim, M.H. and Ahn, H.S. (2015) Review of boiling heat transfer enhancement on micro/nanostructured Surfaces. Experimental Thermal and Fluid Science, 66: p. 173–196.

Kim, H., Truong, B., Buongiorno, J., Hu, L. W. (2011) On the effect of surface roughness height, wettability, and nanoporosity on Leidenfrost phenomena. Applied Physics Letters, 98(8), 083121.

Kim, H. (2006) Floating Phenomenon of a Water Drop on the Surface of Liquid Nitrogen. J. Korean Phys. Soc., 49, L1335-L1338.

Kim, J. (2009) Review of nucleate pool boiling bubble heat transfer mechanisms. International Journal of Multiphase Flow, 35: 1067–1076.

Kim, S., Kim, H. D., Kim, H., Ahn, H. S., Jo, H., Kim, J., Kim, M. J. (2010) Effects of nano-fluid and surfaces with nano structure on the increase of CHF. Exp. Therm. Fluid Sci., 34, 487-495.

Kivisalu, M.T., Gorgitrattanagul, P., Narain, A. (2014) Results for high heat-flux flow realizations in innovative operations of milli-meter scale condensers and boilers. International Journal of Heat and Mass Transfer, 75: p. 381–398.

Konishi, C., Mudawar, I. (2015) Review of flow boiling and critical heat flux in microgravity. International Journal of Heat and Mass Transfer, 80: p. 469–493.

Korolev, A.V., Litvin, A.N. (2002) Investigation of noises in boiling on an electrically heated wire. Journal of Engineering Physics and Thermophysics, 75, 1033-1036.

Kumari, N., Bahadur, V., Garimella, S. V. (2008) Electrical actuation of electrically conducting and insulating droplets using AC and DC voltages. Journal of Micromechanics and Microengineering, 18, 105015.

Kwark, S. M., Kumar, R., Moreno, G., You, S. M. (2012) Transient characteristics of pool boiling heat transfer in nanofluids. J. Heat Transfer, 134, 051015.

Kwatny, H.G., Fink, L.H. (1975) Acoustics, stability, and compensation in boiling water reactor pressure control systems. IEEE transactions on automatic control, 20, 727-739.

Kweon, Y. C., Kim, M. H. (2000) Experimental study on nucleate boiling enhancement and bubble dynamic behavior in saturated pool boiling using a nonuniform dc electric. Int. J. Multiphase Flow, 26, 1351-1368.

Kwon, H. M., Bird, J. C., Varanasi, K. K. (2013) Increasing leidenfrost point using micro-nano hierarchical surface structures. Appl. Phys. Lett., 103, 201601.

Lee, J. Y., Kim M-H., Kaviany, M., Son, S. Y. (2011) Bubble nucleation in microchannel flow boiling using single artificial cavity. Int. J. Heat Mass Transfe, 54, 5139-5148.

Lee, P-S., Garimella, S.V., Liu, D. (2005) Investigation of heat transfer in rectangular microchannels. International Journal of Heat Mass Transfer, 48: p. 1688-1704.

Leidenfrost, J. G. (1966) On the fixation of water in diverse fire. Int. J. Heat Mass Transf. 9, 1153–66.

Li, W., Pham, H.H., Nie, Z., Macdonald, B., Guenther, A., Kumacheva, E. (2008) Multi-step microfludic polymerization reactions conducted in droplets: The internal trigger approach. Am. Chem. Soc. 130:9935–9941.

Li, C., Peterson, G. P. (2007) Parametric study of pool boiling on horizontal highly conductive microporous coated surfaces. J. Heat Transfer, 129, 1465-1475.

Li, D., Wu, G. S., Wang, W., Wang, Y. D., Liu, D., Zhang, D. C., Chen, Y. F., Peterson, G. P., Yang, R. (2012) Enhancing flow boiling heat transfer in microchannels for thermal management with monolithically-integrated silicon nanowires. Nano Lett., 12, 3385-3390.

Link, D.R., Grasland-Mongrain, E., Duri, A., Sarrazin, F., Cheng, Z.D., Cristobal, G., Marquez, M., Weitz, D.A. (2006) Electric Control of Droplets in Microfluidic Devices. Angew. Chem., Int. Ed. 45:2556–2560.

Lippmann, G. (1875) Relations entre les phénomènes électriques et capillaires. Ann. Chim. Phys., 5, 494.

Liu, K., Ding, H., Chen, Y., Zhao, X.Z. (2007) Droplet-based synthetic method using microflow focusing and droplet fusion. Microfluid. Nanofluid. 3:239-243.

Liu, D., Lee, P. S., Garimella, S. V. (2005) Nucleate boiling in microchannels. J. Heat Transfer, 127(8), 803.

Liu, D., Lee, P-S., Garimella, S. (2005) Prediction of the onset of nucleate boiling in microchannel flow. Int. J. Heat Mass Transfer, 48, 5134-5149.

Liu, W., Wang, S., Yang, M., Song, Y., Wang, S., Zhao, J. (2015) Investigation of the Induction Time for THF Hydrate Formation in Porous Media. J. Nat. Gas Sci. Eng., 24, 357–364.

Liu, Z., Herman, C. and Mewes, D. (2006) Visualization of bubble detachment and coalescence under the influence of a nonuniform electric field. Experimental Thermal and Fluid Science, 31: p. 151–163.

Lolla, T., Cola, G., Narayanan, B., Alexandrov, B., Babu, S. S. (2011) Development of rapid heating and cooling (flash processing) process to produce advanced high strength steel microstructures. Materials Science and Technology, 27(5), 863-875.

Lorenceau, E., Utada, A.S., Link, D.R., Cristobal, G., Joanicot, M., Weitz, D.A. (2005) Generations of polymerosomes from double-emulsions. Langmuir, 21:9183–9186.

Lykof, E.V., Sinetskaya, A.G. (2005) Transient process and thermoacoustic effects in surface boiling of a liquid. Journal of Engineering Physics and Thermophysics, 78, 646-650.

Mahadevan, L., Pomeau, Y. (1999) Rolling droplets. Phys. Fluids, 11(9), 2449-2453.

Mahmoudi, R., Adamiak, K., Castle, G. S. P. (2014) Flattening of boiling curves at post-CHF regime in the presence of localized electrostatic fields. Int. J. Heat Mass Transfer, 68, 203-210.

Mahmoudi, R., Adamiak, K., Castle, G. S. P. (2013) Two-phase cooling characteristics of mono-dispersed droplets impacted on an upward-facing heated disk. Exp. Therm. Fluid Sci., 44, 312-322.

Maquet, L., Sobac, B., Darbois-Texier, B., Duchesne, A., Brandenbourger, M., Rednikov, A., Colinet, P., Dorbolo, S. (2016) Leidenfrost drops on a heated liquid pool. Physical Review Fluids, 1, 053902.

Marine, N.A., Klein, S.A., Posner, J.D. (2009) Partition coefficient measurements in picoliter drops using a segmented flow microfluidic device. Anal. Chem. 81:1471–1476.

Markels, M., Durfee, R.L. (1964) The effect of applied voltage on boiling heat transfer. AIChE Journal, 10(1), 106-110.

Markels, M., Durfee, R. L. (1965) Studies of boiling heat transfer with electrical fields: Part I. Effect of applied AC voltage on boiling heat transfer to water in forced circulation. AIChE Journal, 11(4), 716-719.

Markels, M., Durfee, R. L. (1965) Studies of boiling heat transfer with electrical fields: Part II. Mechanistic Interpretations of Voltage Effects on Boiling Heat Transfer. AIChE Journal, 11(4), 720-723.

Marmottant, P., Villermaux, E. (2004) On spray formation. J. Fluid Mech. 498:73–111.

Maryott, A. A., Smith, E. R. (1951) Table of dielectric constants of pure liquids. Natl. Bur. Stand. Circular 5.

McGranaghan, G. J., Robinson, A. J. (2014) The mechanisms of heat transfer during convective boiling under the influence of AC electric fields. Int. J. Heat Mass Transfer, 73, 376-388.

Merrer. M. L., Clanet, C., Quere, D., Raphael, E., Chevy, F. (2011) Wave drag on floating bodies. Proc. Natl. Acad. Sci. U.S.A., 108, 15064–15068.

Migliaccio, C.P., Garimella, S. (2013) Evaporative heat transfer from an electrowetted liquid ribbon on a heated substrate. International Journal of Heat and Mass Transfer, 57: p. 73–81.

Miljkovic, N., Preston, D. J., Enright, R., Wang, E. N. (2013) Electrostatic charging of jumping droplets. Nat. Commun., 4, 2517.

Mitra, S., Saha, S. K., Chakraborty, S., Das, S. (2012) Study on boiling heat transfer of water–TiO2 and water–MWCNT nanofluids based laminar jet impingement on heated steel surface. Applied Thermal Engineering, 37, 353-359.

Mohapatra, S. S., Ravikumar, S. V., Pal, S. K., Chakraborty, S. (2013) Ultrafast cooling of a hot steel plate by using high mass flux air atomized spray. steel research international, 84(3), 229-236.

Mojškerc, B., Kek, T. Grum, J. (2018) Feasibility study of monitoring the steel quenching process using acoustic emission technology. Applied Acoustics, 129, 335-345.

Mondal, K., Bandyopadhyay, D. (2014) Electro-capillary instabilities of thin leaky elastic-viscous bilayers, Physics of Fluids 26, 122006.

Mugele, F., Baret, J-C. (2005) Electrowetting: from basics to applications. J. Phys.: Condens. Matter, 17, R705-R774.

Mulligan, M.K., Rothstein, J.P. (2012) Scale-up and control of droplet production in coupled microfluidic flow-focusing geometries. Microfluid. Nanofluid. 13(1): 65-73.

Naphon, P. (2015) Effect of Magnetic Fields on the Boiling Heat Transfer Characteristics of Nanofluids. International Journal of Thermophysics, 2015. 36: p. 2810–2819.

Neil, G.D., Reuben, R.L., Sandford, P.M., Brown, E.R., Steel, J.A. (1997) Detection of incipient cavitation in pumps using acoustic emission. Proceedings of the Institution of Mechanical Engineers, Part E: Journal of process mechanical engineering, 211, 267-277.

Ng, B.T, Hung, Y. M., Tan, M. K. (2016) Acoustically- controlled Leidenfrost droplets. J. Colloid Interface Sci., 465, 26-32.

Nukiyama, S. (1966) The maximum and minimum values of the heat transmitted from metal to boiling water under atmospheric pressure. Int. J. Heat Mass Transf. 9, 1419–1433.

Nunes, J.K., Tsai, S.S.H., Wan, J., Stone, H.A. (2013) Dripping and jetting in microfluidic multiphase flows applied to particle and fibre synthesis. J. Phys. D: Appl. Phys. 46:114002.

O'Hanley, H., Coyle, C., Buongiorno, J., McKrell, T., Hu, L-W., Rubner, M., Cohen, R. (2013) Separate effects of surface roughness, wettability, and porosity on the boiling critical heat flux. Appl. Phys. Lett., 103, 024102.

Oguz, H.N., Prosperetti, A. (1990) Bubble entrainment by the impact of drops on liquid surfaces. Journal of Fluid Mechanics, 219, 143-179.

Orlowska, M., Havet, M., Le-Bail, A. (2009) Controlled ice nucleation under high voltage DC Electrostatic field conditions. FoodRes. Int., 42(7), 879-884.

Oron, A., Davis, S.H., Bankoff, S.G. (1997) Nonlinear theory of film rupture, Rev. Mod. Phys. 69 931-980.

Orzechowski, T., Wcislik, S. (2014) Instantaneous heat transfer for large drops levitating over a hot surface. Int. J. Heat Mass Transfer, 73, 110-117.

Ozkan, O., Shahriari, A., Bahadur, V. (2017) Electrostatic suppression of the Leidenfrost state using AC electric fields. Appl. Phys. Lett., 111, 141608.

Padilla, J., Carey V. P. (2014) Water droplet vaporization on superhydrophilic nanostructured surfaces at high and low superheat. Proceedings of the ASME 2014 International Mechanical Engineering Congress and Exposition IMECE.

Pandey, V., Biswas, G., Dalal, A. (2016) Effect of superheat and electric field on saturated film boiling. Physics of Fluids, 28: p. 052102.

Paneru, M., Priest, C., Sedev, R., Ralston, J. (2010) Electrowetting of Aqueous Solutions of Ionic Liquid in Solid - Liquid - Liquid Systems. J. Phys. Chem. C 114, 8383–8388.

Panzarella, C.H., Davis, S.H., and Bankoff, S.G. (2000) Nonlinear dynamics in horizontal film boiling. Journal of Fluid Mechanics, 402: p. 163-194.

Pearson, M.R. and Seyed-Yagoobi, J. (2011) EHD Conduction-Driven Enhancement of Critical Heat Flux in Pool Boiling. Journal of Electrostatics, 69: p. 479-485.

Petrov, R., Hajyakbary, F., Sidor, J., Santofimia, M.J., Sietsma, J., Kestens, L.A.I. (2012) MTM Int. VirtualJ, 72.

Piorek, B.D., Lee, S.J., Santiago, J.G., Moskovits, M., Banerjee, S., Meinhart, C.D. (2007) Free-surface microfluidic control of surface-enhanced Raman spectroscopy for the optimized detection of airborne molecules. PNAS 104:18898-18901.

Pioro, I.L., Rohsenow, W. and Doerffer, S.S. (2004) Nucleate pool-boiling heat transfer. I: review of parametric effects of boiling surface. International Journal of Heat and Mass Transfer, 47: p. 5033–5044.

Pohl, H.A. (1978) Dielectrophoresis. Cambridge, UK: Cambridge University Press.

Post, S.L., Abraham, J. (2002) Modeling the outcome of drop–drop collisions in Diesel sprays. Int J Multiphase Flow 28:997–1019.

Priest, C., Herminghaus, S., Seemann, R. (2006) Generation of monodisperse gel emulsions in a microfluidic device. Appl. Phys. Lett. 88:024106.

Quan, X., Gao, M., Cheng, P., Li, J. (2015) An experimental investigation of pool boiling heat transfer on smooth/rib surfaces under an electric field. International Journal of Heat and Mass Transfer, 85: p. 595–608.

Quere, D. (2013) Leidenfrost dynamics, Annu. Rev. Fluid Mech. 45, 197.

Rahman, M., Olceroglu, E. and McCarthy, M. (2014) Role of Wickability on the Critical Heat Flux of Structured Superhydrophilic Surfaces. Langmuir, 30: p. 11225-11234.

Rahman, M., Pollack, J., McCarthy, M. (2015) Increasing boiling heat transfer using low conductivity materials. Scientific Reports, 5: 13145.

Raj, R., Kim, J. (2010) Heater size and gravity based pool boiling regime map: transition criteria between buoyancy and surface tension dominated boiling. J. Heat Transfer, 132(9), 091503-1 - 091503-10.

Ravikumar, S. V., Jha, J. M., Mohapatra, S. S., Sinha, A., Pal, S. K., Chakraborty, S. (2013) Experimental study of the effect of spray inclination on ultrafast cooling of a hot steel plate. Heat and Mass Transfer, 49(10), 1509-1522.

Ravnik, F., Grum, J. (2010) Relation between sound emission occurring during quenching and mechanical properties of the steel after quenching. BHM Berg-und Hüttenmännische Monatshefte, 155, 119-124.

Ravnik, F. Grum, J. (2012) Heat Transfer Stages Recognition by Boiling Acoustic During Quenching. Film and Nucleate Boiling Processes. ASTM International.

Roberts, C.C., Rao, R.R., Loewenberg, M., Brooks, C.F., Galambos, P., Grillet, A.M., Nemer, M.B. (2012) Comparison of monodisperse droplet generation in flow focusing devices with hydrophilic and hydrophobic surfaces. Lab Chip. 12:1540-1547.

Roh, H-S. (2014) Heat transfer mechanisms in pool boiling. Int. J. Heat Mass Transfer, 68, 332-342.

Sajadi, S. M., Irajizad, P., Kashyap, V., Farokhnia, N., Ghasemi, H. (2017) Surfaces for high heat dissipation with no Leidenfrost limit. Appl. Phys. Lett., 111, 021605.

Savino, R., Paterna, D., Lappa, M. (2003) Marangoni floatation of liquid droplets. J. Fluid Mech., 479, 307-326.

Schaffer, E., Thurn-Albrecht, T., Russel, R.P., Steiner, U. (2000) Electrically induced structure formation and pattern transfer, Nature 403, 874-877.

Schweizer, N., Di Marco, P., Stephan, P. (2013) Investigation of wall temperature and heat flux distribution during nucleate boiling in the presence of an electric field and in variable gravity. Exp. Therm. Fluid Sci., 44, 419-430.

Seemann, R., Brinkmann, M., Pfohl, T., Herminghaus, S. (2012) Droplet based microfluidics. Rep. Prog. Phys. 75:016601.

Shabani, R., Cho, H.J. (2013) Flow rate analysis of an EWOD-based device: how important are wetting-line pinning and velocity effects?, Microfluid. Nanofluid. 15:587-597.

Shabani, R., Kumar, R., Cho, H. J. (2013) Droplets on liquid surfaces: Dual Equilibrium states and their energy barrier. Appl. Phys. Lett., 102, 184101.

Shahriari, A., Ozkan, O., Bahadur, V. (2017) Electrostatic suppression of the Leidenfrost state on liquid substrates. Langmuir, 33, 13207–13213.

Shahriari, A., Wurz, J., Bahadur, V. (2014) Heat Transfer Enhancement Accompanying Leidenfrost State Suppression at Ultrahigh Temperatures, Langmuir 30, 12074-12081.

Shahriari, A., Hermes, M., Bahadur, V. (2016) Electrical control and enhancement of boiling heat transfer during quenching. Applied Physics Letters, 108: p. 091607.

Shahriari, A., Birbarah, P., Oh, J., Miljkovic, N., Bahadur, V. (2016) Electric-field-based control and enhancement of boiling and condensation. Nanoscale Microscale Thermophys. Eng.

Shahriari, A., Das, S., Bahadur, V., Bonnecaze, R. T. (2017) Analysis of the instability underlying electrostatic suppression of the Leidenfrost state. Phys. Rev. Fluids, 2034001.

Shapiro, B., Moon, H., Garrell, R. L., Kim, C. (2003) Equilibrium behavior of sessile drops under surface tension, applied external fields, and material variations. J. Appl. Phys., 93.

Sheikhbahai, M., Nasr Esfahany, M. and Etesami, N. (2012) Experimental investigation of pool boiling of Fe3O4/ethylene glycolewater nanofluid in electric field. International Journal of Thermal Sciences, 62: p. 149-153.

Sher, I., Harari, R., Reshef, R., Sher, E. (2012) Film boiling collapse in solid spheres immersed in a sub-cooled liquid. Applied Thermal Engineering, 36, 219-226.

Shichiri, T., Nagata, T. (1981) Effect of Electric currents on the nucleation of ice crystals in the melt. J. Cryst. Growth, 54, 207-210.

Shirota, M., van Limbeek, M.A.J., Sun, C., Prosperetti, A. (2016) Dynamic Leidenfrost effect: relevant time and length scales, D. Lohse, Phys. Rev. Lett. 116, 064501.

Siedel, S., Cioulachtjian, S., Robinson, A.J., Bonjour, J. (2011) Electric field effects during nucleate boiling from an artificial nucleation site. Experimental Thermal and Fluid Science, 35: p. 762–771.

Sloan, D., Koh, C. (2008) Clathrate Hydrates of Natural Gases, Third ed., CRC Press, Taylor & Francis Group: New York.

Smrke, A., Prezlej, J., Steblaj, P., Smrke, I. (2012) Sound of boiling as a disturbing noise and as a functional signal. MIPRO.

Snezhko, A., Jacob, E. B., Aranson, I. S. (2008) Pulsating–gliding transition in the dynamics of levitating liquid nitrogen droplets. New Journal of Physics, 10, 043034.

Sohel Murshed, S.M., Nieto de Castro, C.A., Lourenco, M.J.V., Lopes, M.L.M. and Santos, F.J.V. (2011) A review of boiling and convective heat transfer with nanofluids. Renewable and Sustainable Energy Reviews, 15: p. 2342–2354.

Son, G., Dhir, V.K. (2008) Numerical simulation of nucleate boiling on a horizontal surface at high heat fluxes. International Journal of Heat and Mass Transfer, 51: p. 2566–2582.

Song, H., Chen, D.L., Ismagilov, R.F. (2006) Reactions in Droplets in Microfluidic Channels. Angew. Chem., Int. Ed. 45:7336-7356.

Song, Y., Baudoin, M., Manneville, P., Baroud, C.N. (2011) The air–liquid flow in a microfluidic airway tree. Med. Eng. Phys. 33:849-856.

Suh, K.Y., Kim, P., Lee, H.H. (2004) Capillary Kinetics of thin polymer films in permeable microcavities. Appl. Phys. Lett. 85:4019-4021.

Sum, A. K., Koh, C. A., Sloan, E. D. (2009) Clathrate Hydrates: From Laboratory Science to Engineering Practice. Ind. Eng. Chem. Res., 48 (16), 7457–7465.

Sun, X., Tang, K., Smith, R.D., Kelly, R.T. (2013) Controlled dispensing and mixing of pico- to nanoliter volumes using on-demand droplet-based microfluidics. Microfluid. Nanofluid. 15:117-126.

Sur, A., Lu, Y., Pascente, C., Ruchhoeft, P., Liu, D. (2018) Pool boiling heat transfer enhancement with electrowetting. Int. J. Heat Mass Transfer, 120, 202-217.

Takano, K., Tanasawa, I. and Nishio, S. (1996) Enhancement of evaporation of a droplet using EHD effect. JSME International Journal. Series B, Fluids and Thermal Engineering, 37(3): p. 583-589.

Takata, Y., Shirakawa, H., Tanaka, K. and ITO, T. (2003) Numerical Study on Motion of a Single Bubble Exerted by Non-uniform Electric Field. International Journal of Transport Phenomena, 5: p. 247-258.

Tan, S.H., Murshed, S.M.S., Nguyen, N.T., Wong, T.N., Yobas, L. (2008) Thermally controlled droplet formation in flow focusing geometry: formation regimes and effect of nanoparticle suspension. J. Phys. D: Appl. Phys. 41:165501.

Tan, S.H., Nguyen, N.T., Chua, Y.C., Kang, T.G. (2010) Oxygen plasma treatment for reducing hydrophobicity of a sealed polydimethylsiloxane microchannel. Biomicrofluid 4:032204.

Tan, Y.C., Cristini, V., Lee, A.P. (2006) Monodispersed microfluidic droplet generation by shear focusing microfluidic device. Sensor Actuat. B-Chem. 114:350-356.

Tan, Y.C., Ho, Y.L., Lee, A.P. (2008) Microfluidic sorting of droplets by size. Microfluid. Nanofluid. 4:343-348.

Tanyeri, M., Ranka, M., Sittipolkul, N., Schroeder, C.M. (2011) A microfluidic-based hydrodynamic trap: Design and implementation, Lab Chip, 11:1786-1794.

Thiele, J., Windbergs, M., Abate, A.R., Trebbin, M., Shum, H.C., Forster, S., Weitz, D.A. (2011) Early development drug formulation on a chip: Fabrication of nanoparticles using a microfluidic spray dryer. Lab Chip, 11, 2362-2368.

Thomason W. H., Blumer D. J., Singh P., Cope D. P. (2005) Advanced electrostatic technologies for dehydration of heavy oils. SPE International Thermal Operations and Heavy Oil Symposium, Calgary, Canada, SPE/PS-CIM/CHOA 97786.

Thorsen, T., Roberts, R.W., Arnold, F.H., Quake, S.R. (2001) Dynamic pattern formation in a vesicle-generating microfluidic device. Phys. Rev. Lett. 86:4163–4166.

Tombari, E., Presto, S., Salvetti, G., Johari, G. P. (2006) Heat Capacity of Tetrahydrofuran Clathrate Hydrate and of Its Components, and the Clathrate Formation from Supercooled Melt. J. Chem. Phys., 124, 154507−154506.

Tong, L. S., Tang Y. S. (1997) Boiling Heat Transfer and Two-Phase Flow, 2nd ed. Washington, D.C.: Taylor and Francis.

Unal, C., Daw, V., Nelson, R. A. (1992) Unifying the controlling mechanisms for the critical heat flux and quenching: the ability of liquid to contact the hot surface. Journal of heat transfer, 114(4), 972-982.

Utada, A.S., Lorenceau, E., Link, D.R., Kaplan, P.D., Stone, H.A., Weitz, D.A. (2005) Monodisperse double emulsions generated from microcapillary device. Science 308:537–541.

Vakarelski, I.U., Patankar, N.A., Martson, J.O, Chan, D.Y.C, Thoroddsen, S.T. (2012) Stabilization of Leidenfrost vapour layer by textured superhydrophobic surfaces, Nature 489, 274.

van Dijke, K., Kobayashi, I., Uemura, K., Nakajima, M., Boom, R. (2010) Effect of viscosities of dispersed and continuous phases in microchannel oil-in-water emulsification. Microfluid. Nanofluid. 9:77-85.

Vassallo, P., Kumar, R. and D'Amico, S. (2004) Pool boiling heat transfer experiments in silica–water nano-fluids. International Journal of Heat and Mass Transfer, 47: p. 407–411.

Veluswamy, H. P., Kumar, R., Linga, P. (2014) Hydrogen Storage in Clathrate Hydrates: Current State of the Art and Future Directions. Appl. Energy, 122, 112−132.

Verplaetsen, F., Berghmans, J. A. (1997) The influence of an electric field on the heat transfer rate during film boiling of stagnant fluids, Rev. Gén. Therm., 37 (2), 83-88.

Verplaetsen, F.M., Berghmans, J.A. (1999) Film boiling of an electrically insulating fluid in the presence of an electric field. Heat and Mass Transfer, 35: p. 235-241.

Wada, Y., Schmidt, M.A., Jensen, K.F. (2006) Flow Distribution and Ozonolysis Reaction in Gas-Liquid Multichannel micro reactors. Ind. Eng. Chem. Res. 45:8036-8042.

Wan, J., Stone, H.A. (2012) Coated gas bubbles for the continuous synthesis of hollow inorganic particles. Langmuir 28:37-41.

Wang, H., Yu, W., Cai, Q. (2012) Experimental study of heat transfer coefficient on hot steel plate during water jet impingement cooling. Journal of Materials Processing Technology, 212(9), 1825-1831.

Wang, P., Lewin, P.L., Swaffield, D.J., Chen, G. (2009) Electric field effects on boiling heat transfer of liquid nitrogen. Cryogenics, 49: p. 379–389.

Wei S., Xiaobin X., Hong Z., Chuanxiang X. (2008) Effect of dipole polarization of water molecules on ice formation under an electrostatic field. Cryobiology, 56, 93-99.

Welch, S., Biswas, G. (2007) Direct simulation of film boiling including electrohydrodynamic forces. Phys. Fluids, 19, 012106.

Wheeler, A.R., Moon, H., Bird, C.A., Ogorzalek R.R., Kim, C.J., Loo, J.A., Garrell, R.L. (2004) Digital microfluidics with in-line sample purification for proteomics analyses with MALDI-MS. Anal. Chem. 77:534-540.

Wilson, P. W., Haymet, A. D. J. (2010) Hydrate Formation and Re-Formation in Nucleating THF/water Mixtures Show No Evidence to Support a “Memory” Effect. Chem. Eng. J., 161, 146−150.

Wilson, P. W., Lester, D., Haymet, a. D. J. (2005) Heterogeneous Nucleation of Clathrates from Supercooled Tetrahydrofuran (THF)/water Mixtures, and the Effect of an Added Catalyst. Chem. Eng. Sci., 60, 2937–2941.

Xu, J.H., Li, S.W., Tan, J., Luo, G.S. (2008) Correlations of droplet formation in T-junction microfluidic devices: from squeezing to dripping. Microfluid. Nanofluid. 5:711-717.

Xu, Q., Hashimoto, M., Dang, T.T., Hoare, T., Kohane, D.S., Whitesides, G.M., Langer, R., Anderson, D.G. (2009) Preparation of monodisperse biodegradable polymer microparticles using a microfluidic flow-focusing device for controlled drug delivery. Small 5:1575–1581.

Yang, L., Fan, S.S., Wang, Y.H., Lang, X.M, Xie, D.L. (2011) Accelerated formation of methane hydrate in aluminum foam. Ind. Eng. Chem., 50, 11563-11569.

Yang, S.M., Yao, H., Zhang, D., Li, W.J., Kung, H.F., Chen, S.C. (2015) Droplet-based dielectrophoresis device for on-chip nanomedicine fabrication and improved gene delivery efficiency. Microfluid. Nanofluid. 19:235-243.

Yang, Q., Li, B.Q., Ding, Y. (2013) Electrohydrodynamic Patterning of Micro/Nano-Structures on Thin Polymer Films, Proceedings of the ASME 2013 International Mechanical Engineering Congress and Exposition.

Yasuda, T., Imamura, K., Hirase, K. (2009) Droplet transportation using EWOD-induced wettability gradient. Solid-State Sensors, Actuators and Microsystems Conference (Transducers) 413-416.

Yobas, L., Martens, S., Ongand, W.L., Ranganathan, N. (2006) High-performance flow-focusing geometry for spontaneous generation of monodispersed droplets. Lab Chip. 6:1073–1079.

Zaghdoudi, M. C., Lallemand, M. (1999) Analysis of the polarity influence on nucleate pool boiling under a dc electric field. J. Heat Transfer, 121(4), 856-864.

Zaghdoudi, M. C., Lallemand, M. (2005) Pool boiling heat transfer enhancement by means of high dc electric field. Arab. J. Sci. Eng., 30, 189-212.

Zhang, K., Liang. Q., Ma, S., Mu, X., Hu, P., Wang, Y., Luo, G. (2009) On-chip manipulation of continuous picoliter-volume superparamagentic droplets using a magnetic force. Lab Chip 9:2992-2999.

Zhang, H.B., Yan, Y.Y., Zu, Y.Q. (2010) Numerical modelling of EHD effects on heat transfer and bubble shapes of nucleate boiling. Applied Mathematical Modelling, 34: 626–638.

Zhang, J. S., Lee, S., Lee, J. W. (2007) Kinetics of Methane Hydrate Formation from SDS Solution. Ind. Eng. Chem. Res., 46, 6353−6359.

Zhang, J. S., Lo, C., Somasundaran, P., Lu, S., Couzis, A., Lee, J. W. (2008) Adsorption of Sodium Dodecyl Sulfate at THF Hydrate / Liquid Interface. J. Phys. Chem., 112, 12381–12385.

Zhong, Y., Rogers, R. E. (2000) Surfactant Effects on Gas Hydrate Formation. Chem. Eng. Sci., 55, 4175–4187.

Zhou, C.F., Yue, P.T., Feng, J.J. (2006) Predicting sizes of droplets made by microfluidic flow-induced dripping. Phys. Fluids. 18:092105.

Zou, A., Maroo, S. C. (2013) Critical height of micro/nano structures for pool boiling heat transfer enhancement. Appl. Phys. Lett., 103, 221602.